UNIVERSITY OF COPENHAGEN
NIELS BOHR INSTITUTE

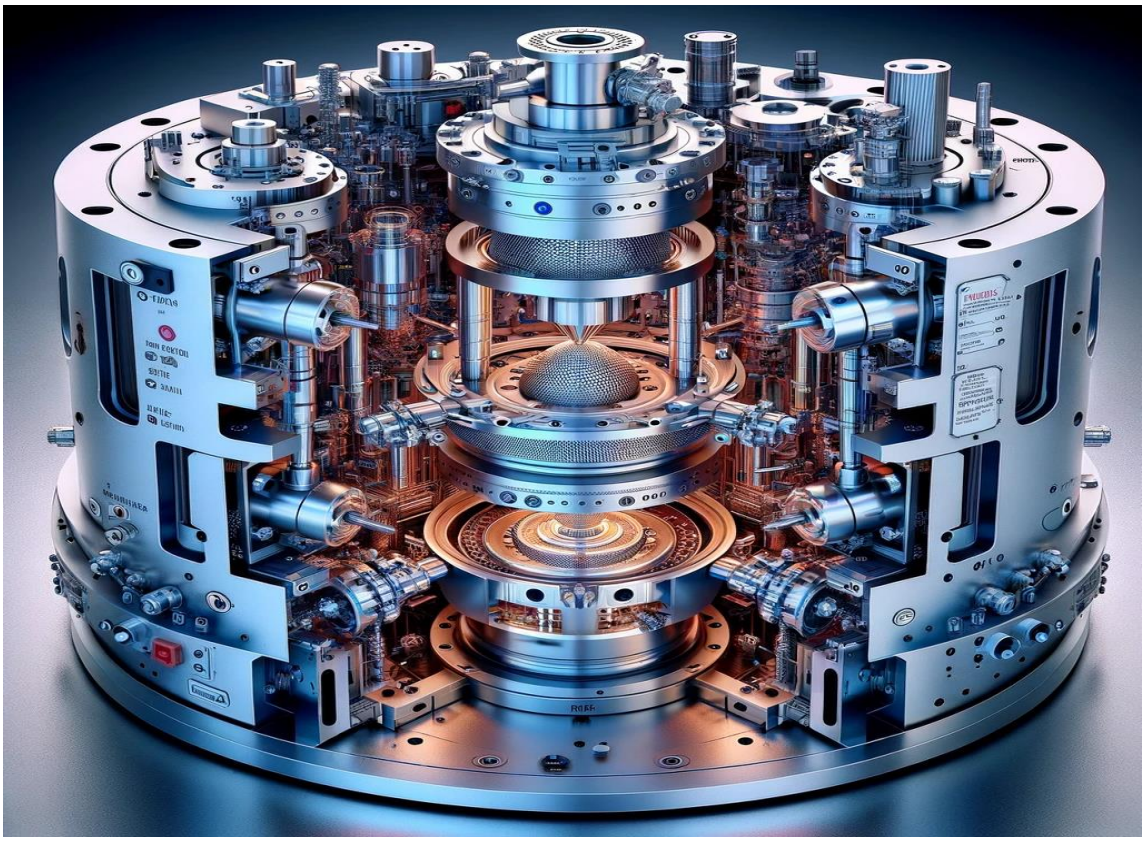

PhD thesis

Tobias Særkjær

Bottom-up nanoscale synthesis of quantum circuits

Supervisor: Peter Krogstrup

Submitted: 1. januar 2024

This thesis has been submitted to the PhD School of The Faculty of Science,
University of Copenhagen

Bottom-up nanoscale synthesis of quantum circuits

UNIVERSITY OF COPENHAGEN
FACULTY OF SCIENCE

Bottom-up nanoscale synthesis of quantum circuits

Tobias Særkjær

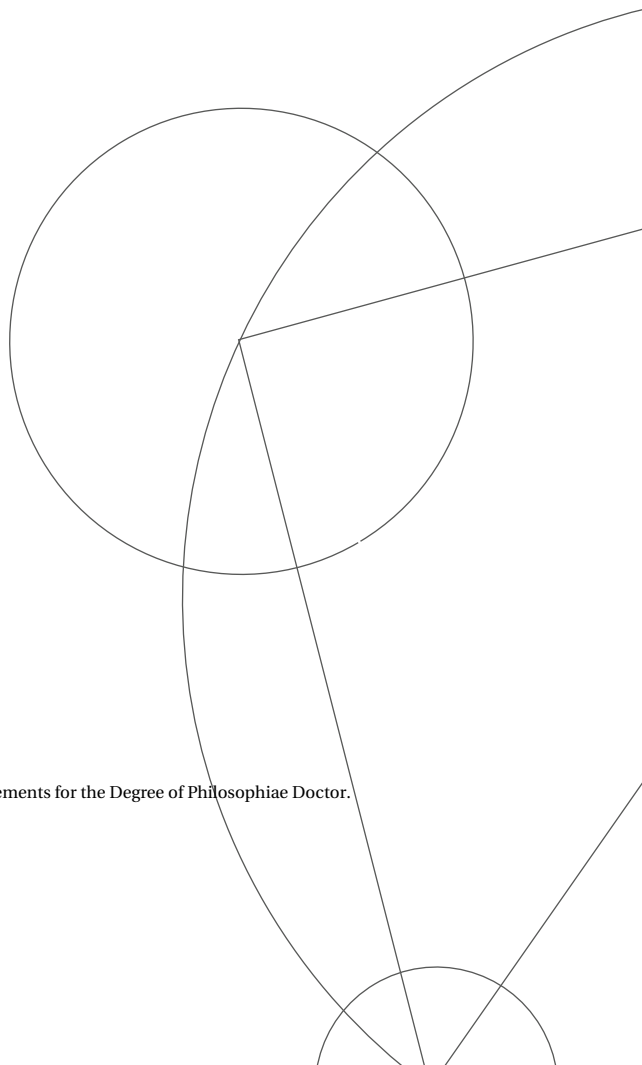

Advisor:
Prof. Peter Krogstrup

Co-advisor:
Prof. Thomas Kanne

Assessment committee:
Prof. Jesper Nygård
Prof. Frank Glas
Prof. Detlev Grützmacher

Thesis submitted in partial fulfillment of the requirements for the Degree of Philosophiae Doctor.

Bottom-up nanoscale synthesis of quantum circuits
Tobias Særkjær
Copenhagen, January 2024.

Citation:
Særkjær, T. *Bottom-up nanoscale synthesis of quantum circuits.* (2024) Niels Bohr Institute, University of Copenhagen.

Abstract

This thesis is a summary of my work spanning almost 3½ years, spent with the Novo Nordisk Foundation Quantum Computing Programme and with the Center for Quantum Devices at the Niels Bohr Institute, University of Copenhagen.

It recounts my efforts in the intersection between physics, materials science and engineering towards the realization of nano- and microscale circuits with relevance for quantum computing applications. The efforts are part of a larger scale research effort into quantum devices and quantum computing technology, but very little quantum physics appears in this thesis. Rather, the focus is on the enabling technology, going through considerations for the high-cleanliness quantum circuit synthesis.

The novel stencil techniques proposed towards the end of this thesis allow for multiple qubit fabrication steps within one in-situ UHV step, offering improvements in qubit performance and reproducibility. The pristine conditions are kept for devices fabricated with these techniques, as little to no ex-situ fabrication is necessary. While challenges remain on the engineering side, I am hopeful and confident that these techniques will prevail and prove valuable for quantum device fabrication in the long run.

Resumé

Denne afhandling er en sammenfatning af mit arbejde fordelt over næsten 3½ år ved Novo Nordisk Foundation Quantum Computing Programme og ved Center for Quantum Devices ved Niels Bohr Institutet, Københavns Universitet.

Afhandlingen afspejler mit bidrag i krydsfeltet mellem fysik, materialevidenskab og ingeniørarbejde hen mod realiseringen af nano- og mikro-kredsløb med relevans for kvantecomputer-applikationer. Mit arbejde er del af en større forskningsprojekt omkring kvantekredsløb og kvantecomputer-teknologi, men meget lidt kvantefysik optræder i selve afhandlingen. Fokus er i stedet på den muliggørende teknologi, hvor jeg gennemgår forskellige overvejelser for ultra-ren kredsløbs-syntese.

De nyskabende stencil-teknikker som præsenteres hen mod de afsluttende kapitler i denne afhandling gør det muligt at udføre flere fabrikationstrin for kvantebits i ét in-situ forløb, hvilket giver forbedringer i ydeevne og reproducibilitet for kvantebits. De ultrarene og uberørte forhold kan bevares for enheder fremstillet med disse teknikker, da behovet for ex-situ fabrikation skæres fra. Der er stadig ingeniør-mæssige udfordringer tilbage, men jeg er håbefuld og sikker på, at disse teknikker vil vinde indpas og vise sig som værdifulde til fabrikation af kvanteenheder i det lange løb.

Acknowledgments

First and foremost, I extend my heartfelt gratitude to my supervisor, **Peter**, for his invaluable guidance. His role in facilitating my participation in esteemed academic endeavors, such as the Microsoft Quantum Materials Lab Lyngby and the pioneering Novo Nordisk Foundation Quantum Computing Programme, has been instrumental in my PhD journey. The caliber of academic research and the wealth of opportunities for collaborative engagement and intellectual exchange provided by these research programmes have been indispensable in my studies.

Additionally, the contribution of my co-supervisor, **Thomas**, has been nothing short of extraordinary. His involvement has been crucial not only in the inventive aspects central to my thesis work but also in the way he has helped nudge and steer my projects in the right directions. Thomas's keen insight into continuous improvement and his knack for identifying new objectives have been pivotal in shaping my thesis. Having shared an office with Thomas for a year and a half, I have been privileged to experience his support and friendship first-hand. This thesis, undoubtedly, would have been significantly less comprehensive without his support and camaraderie.

I wish to express my profound appreciation to the members of my assessment committee, chaired by **Jesper Nygård**, with esteemed members **Frank Glas** and **Detlev Grützmacher**. Their willingness to dedicate time and effort to meticulously read and evaluate my thesis is deeply valued. I am hopeful that the ideas and concepts presented in this work will resonate with and perhaps even intrigue these distinguished experts in the field.

I would also like to acknowledge the significant impact of my primary co-inventors, **Michaela** and **Morten**. Their invitation to join the stencil project marked a turning point in my academic journey. The fusion of exceptional experimental work with theoretical advancements under their and Thomas' guidance has been a source of inspiration and has substantially increased my productivity. The experience of transforming theoretical concepts into tangible reality through our work on stencil inventions has been nothing short of enlightening. The results and memories of this collaboration will be treasured for many years.

I am also indebted to numerous collaborators who have contributed to my journey in various capacities. My good friend and co-author **Thue**, along with other students and colleagues from QDev, Microsoft, and NQCP, have provided invaluable inspiration, guidance, and friendships. On the academic front, I extend my thanks to **Martin**, **Laurits**, **Anna**, **Daria**, **Gunjan**, **Sangeeth**, and **Oskar**. My apologies for inadvertently forgetting someone in this acknowledgment. In addition, the administrative support, often the unsung heroes of any academic endeavor, has been crucial. I am immensely thankful for the assistance provided by **Gitte**, **Michelle**, **Helle**,

Natascha, **Jeanette**, **Maria**, **Lena**, and **Katrin**. Their contributions have been essential in facilitating various aspects of my research and studies. My heartfelt gratitude towards **Jonas Johansson** from Lunds Universitet for his boundless hospitality and unmatched expertise in mass transport modeling for nanoscale systems. Jonas's skill in formulating equations and rendering complex concepts accessible is truly commendable. I am also immensely grateful to **Alexandra Lindholm** for her diligent organization related to my campus visits and for her assistance in navigating the university.

Finally, my deepest and most profound love is reserved for my family. To my wife, **Maria**, for her endless patience and resilience, and for consistently making arrangements, especially during the times I felt the need to work late hours, weekends, or holidays. Especially after the times in December '23, with the entire family sick for the better part of two weeks right up to the deadline for this thesis, I am convinced that we can actually overcome anything. To our children, **Vita** and **Henry**, you have brought an entirely new dimension to my life, altering my perspective on virtually everything. Returning home to you after work each day has become the highlight of my daily routine. It is astounding to think that just three years ago, you were not yet a part of our lives, and now, I can hardly imagine the time before you were here. Balancing parental responsibilities with academic endeavors has been an immense challenge, yet it has been even more fulfilling than challenging. My life is immeasurably enriched by your presence, and I cherish every moment with you.

Contents

List of figures

Preface

The pursuit of technological and scientific breakthroughs often stems from a blend of focused theoretical inquiry and relentless experimental endeavors. It's the synergy of these efforts that propels the boundaries of knowledge and innovation forward. In large-scale fundamental research projects, this collaborative journey involves the contributions of thousands of scientists, specialists, and engineers. Each participant plays a crucial role, though they may not always have the opportunity to fully perceive the broader impact of their individual contributions.

However, in research areas that are particularly novel, specialized, and narrowly focused, researchers may find themselves in a unique position. They can be involved in the entire early life cycle of an idea – from its initial conceptualization, through theoretical development, to the practical challenges of experimental realization. In these cases, even though the immediate impact might seem modest, such early-stage explorations are vital for the advancement of ideas and technologies.

This thesis is a narrative of my own modest contributions within such a context. Fortuitously, I became involved in an intriguing stencil project partway through my PhD journey. This project not only shaped the direction of the latter part of my thesis but also brought new perspectives to the work I had already conducted. It continues to encourage our research group to explore the potential of this innovative approach further. My hope is that the concepts and ideas presented in this thesis will resonate with the readers and spark interest among experimentalists who possess the curiosity and expertise to ground these ideas further in the realm of practical implementation.

Thesis outline

This thesis ultimately leads towards novel stencil methods, exploring properties of stencil inventions for synthesis of quantum circuits. The initial chapters serve as context and help to exemplify considerations necessary for the design and realization of nanoscale circuity. The latter chapters delve into this novel stencil approach by way of theory and simulation.

- Chapter 1: An introduction to chip-based quantum technology, setting the stage with classical circuit fabrication concepts. This chapter establishes the broader motivation and thematic groundwork for the thesis.
- Chapter 2: Discusses the basics of crystal growth, focusing on the physical processes and phenomena involved in bottom-up synthesis. It lays the foundation for understanding adatom kinetics and thermodynamics and their role in crystal growth.
- Chapter 3: Introduces mask-on-substrate based techniques, particularly lift-off and Selective Area Growth (SAG), providing a baseline for compairson with subsequent stencil based methods. This chapter helps set the context for studies of phenomena related to SAG systems presented in the following three chapters.
- Chapter 4: Delves into Selective Area Growth rates and their design dependencies, bridging the gap between design intricacies and growth outcomes. The theory and type of analysis conducted here would be equally relevant in a stencil based parallel study. This contents of this chapter are based on my contributions to the paper, ref. [P1].
- Chapter 5: Explores the effects of mismatch strain in heteroepitaxial growth, examining both theoretical and experimental perspectives on strain-induced growth transitions. We conduct a literature review for context before the paper in the following chapter.
- Chapter 6: A study on strain relaxation in Selective Area Grown heterostructures, focusing on misfit dislocation configurations at the critical height. This chapter primarily recites my contributions to the paper, ref. [P2], extending the discussion on strain and dislocations.
- Chapter 7: Introduces basic stencil based techniques as an alternative to mask-on-substrate methods, analyzing the impact of this paradigm shift on circuit production and geometric design. We derive characteristic flux dependence relationships in a framework which encompasses both mask-on-substrate and stencil based techniques. The flux dependencies found here also carry relevance for the more advances stencil methods presented in the following chapters.

- Chapter 8: Presents the innovative concept of flux filtering stencils, based on alignment of series of aperture arrays, exploring new control parameters through analytical and simulation-based approaches. We provide comparison with experiments, empirically verifying the geometry based functionality of the technique.
- Chapter 9: Offers practical insights into adapting stencil design for flux filtering applications, including script automation for design adaptations and efficient flux simulations. We also speculate on additional applications, briefly touching on atomistic simulations for dual species depositions, and providing derivations of additional geometry with relevance for binary or ternary depositions, highly relevant for e.g. III/V semiconductors.
- Chapter 10: Provides a short introduction to multi-gap stencils, a novelty building upon the flux filtering stencil technique by incorporating local control of the gap parameter, g, enhancing design flexibility and flux precision. This chapter is short and conceptual, addressing some issues identified previously, and more or less marking the state of our technical progress at the point of writing.
- Chapter 11: Concludes the thesis, summarizing key findings and contributions, and providing a brief research outlook.

Publications

Parts of this thesis are based on work leading to the papers listed below.

P1 *Selective area growth rates of III-V nanowires*
Martin Espiñeira Cachaza, Anna Wulff Christensen, Daria Beznasyuk, **Tobias Særkjær**, Morten Hannibal Madsen, Rawa Tanta, Gunjan Nagda, Sergej Schuwalow, and Peter Krogstrup
Phys. Rev. Materials 5, 094601, ref. [P1].
I contributed substantially to the theory, analysing and simulating results from experiments.

P2 *Collective formation of misfit dislocations at the critical thickness for equilibrium nanowire heterostructures*
Tobias Særkjær*, Thue Christian Thann*, Sergej Schuwalow, and Peter Krogstrup
Journal of Crystal Growth, Volume 622, 127400, ref. [P2].
I did the primary work on the scientific investigation, model building, parameter sweeping, analysis, generating images and writing the paper.

Drafts not included in this thesis

These papers are in a preparatory state, and are not included here.

P3 *Geometrical approach to finite source shadow selectivity*
Tobias Særkjær*, Michaela Eichinger*, Thomas Kanne Nordqvist, Morten Kjaergaard and Peter Krogstrup
In preparation, ref. [P3]
I did the primary work with derivation of theory, parameter examinations, writing scripts for adaptation and simulation, generating images and writing the paper.

P4 *The Shadow Mask Polarizer - A stencil lithography technique for the in-situ fabrication of quantum devices*
Michaela Eichinger*, **Tobias Særkjær***, Thomas Kanne Nordqvist, Morten Kjaergaard and Peter Krogstrup
In preparation, ref. [P4].
I contributed significantly to the experimental design, developed the theory being tested, made pattern inputs and adaptations, conducted simulations and some analysis of experimental results.

Asterisk* denotes equal author contribution.

Patent applications

The work in this thesis has contributed significantly to the following patent applications filed by the University of Copenhagen.

PA1 *Polarizer stencil mask*
Michaela Eichinger, Thomas Kanne, **Tobias Særkjær**, Morten Kjaergaard, and Peter Krogstrup Jeppesen
Patent application PCT/EP2023/066474 – filed June 19th 2023

PA2 *Stencil mask with barriers*
Thomas Kanne Nordqvist, **Tobias Særkjær**, Asbjørn Cennet Cliff Drachmann, Oskar Leiva Perstølen, Michaela Eichinger, and Peter Krogstrup Jeppesen
Patent application – filed December 21st 2023

Part I

Introduction

1

Quantum technology and circuit fabrication

1.1 Integrated circuits (ICs)

The recent decades have been characterized by an exponential surge in both academic and industrial engagement with quantum technologies. This burgeoning interest is fueled by a confluence of factors: deepening theoretical insights, breakthroughs in fabrication methodologies, and experimental endeavors culminating in the tangible realization of quantum technologies. This thesis delves into the intricacies of nanoscale circuit synthesis for quantum applications, eventually presenting an innovative stencil based technique for such nanofabrication. To provide a foundational understanding and establish essential terminology, an overview of classical electronic circuits is presented, offering some historical perspective.

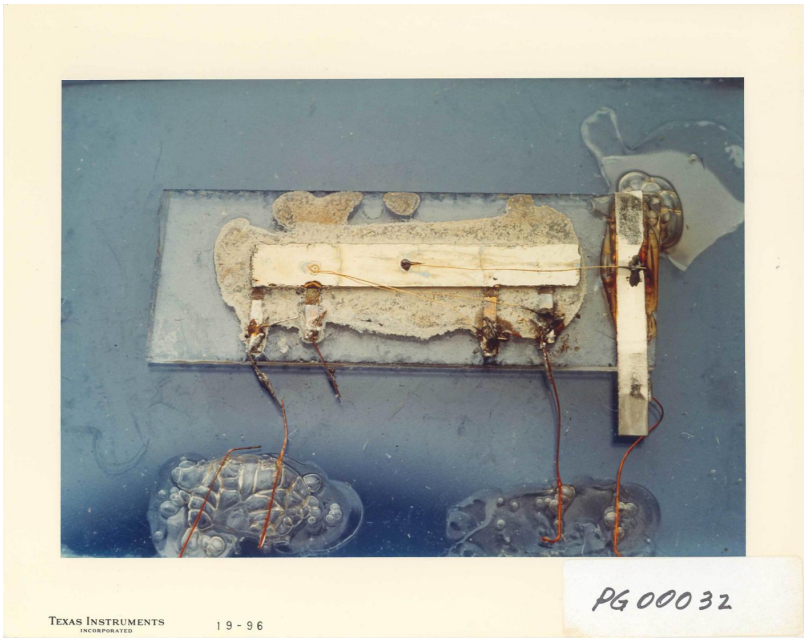

Figure 1.1: **The first integrated circuit:** Jack Kilby's phase shift oscillator which is widely considered to be the first integrated circuit. The rectangular part is a germanium substrate with a single bipolar transistor under the bar of aluminium in the center. The smaller aluminium bars at the bottom are input/output connections, and the large aluminium bar on the right is ground. Connections are soldered gold wires. The circuit measures 5 cm x 2.5 cm.

Integrated circuits (ICs) are at the epicenter of contemporary electronics, pivotal in shaping the modern world, particularly in the realms of telecommunications and information processing. An IC is essentially a compact electronic circuit, composed of various elements like transistors,

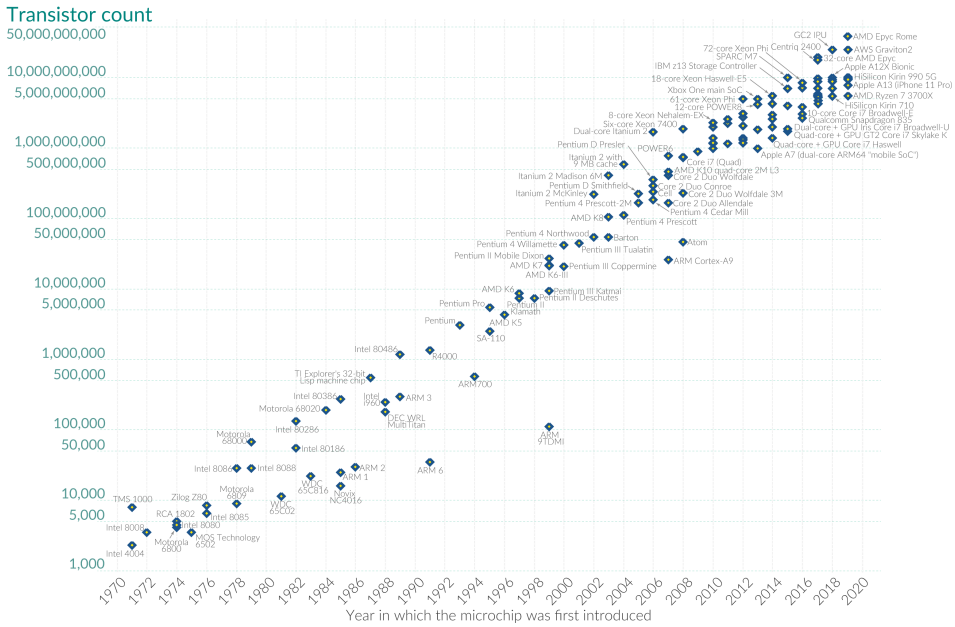

Figure 1.2: **Moore's law visualized:** Number of transistors on integrated circuits plotted on a logarithmic scale vs. year. The trend shows approximate doubling every two years.
By Max Roser, Hannah Ritchie – https://ourworldindata.org/uploads/2020/11/Transistor-Count-over-time.png
CC BY 4.0, https://commons.wikimedia.org/w/index.php?curid=98219918

diodes, and resistors, integrated onto a single semiconductor substrate, typically silicon. The genesis of ICs in the mid-20th century, attributed to several pioneers including the notable Jack S. Kilby (Nobel Laureate, 2000), marked a revolutionary step in electronics[5].

Since their inception, ICs have undergone a remarkable evolution, witnessing substantial enhancements in complexity and functionality, while their physical size and production costs have concurrently diminished. The integrated circuit paradigm has become so pervasive that the terms ICs and circuits are often used interchangeably. The period from the mid-1900s onwards saw the semiconductor industry flourish into a sophisticated and incredibly successful sector, underpinning contemporary technological advances. This industry achieved unprecedented scaling in computing power and transistor density through continuous innovation across various domains (see figure 1.2).

In the quest for a scalable quantum computing architecture, valuable insights can be gleaned from the success story of the semiconductor industry. Essential to quantum applications is the integration of components

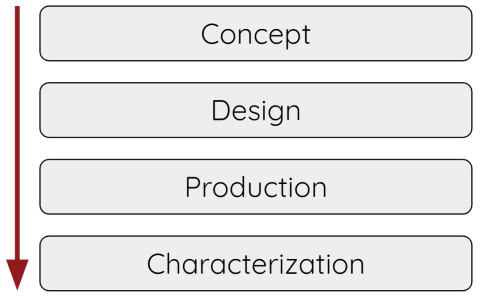

Figure 1.3: **Basic circuit synthesis workflow:** In the simplest form, the workflow involves four stages from concept towards realization. The stages are described further in the main text.

and connections onto a substrate with nanometer precision, targeting lateral resolutions in the order of tens of nanometers. Therefore, in the realm of chip-based quantum computing hardware, a bottom-up approach, emerges as the primary methodology.

Circuit synthesis workflow

The synthesis of circuits encompasses work in multiple stages, and the research presented in this thesis spans several of these. To add context to the research in distinct chapters, this thesis will identify the main stage(s) corresponding to each chapter within the framework of a simplified workflow, as illustrated in figure 1.3. Most of the contents are centered around the production stage, with some overlap towards the design and characterization stages. Modifications to this workflow will be introduced in chapters 3 and 7, but this simplified version will suffice for initial discussions.

Concept entails the circuit in a rudimentary and theoretical format, akin to a basic circuit diagram in conventional electronics. This stage outlines the essential components and their interconnections, highlighting fundamental characteristics. For quantum circuits, these "basic" features might encompass complex material parameters or the application of external magnetic fields.

Design involves a more concrete visualization of the circuit as it is envisaged on the wafer or substrate. Analogous to a detailed blueprint in traditional electronics, this stage includes precise dimensions and material compositions. Like its conventional counterpart, the blueprint is typically multi-dimensional, encompassing various layers of functionality and connectivity. In essence, the design phase outlines the envisaged final circuit structure.

Production stage, encompassing synthesis and fabrication, is concerned with actualizing the design. In bottom-up synthesis, this involves transferring patterns from the design (for instance, through lithographic techniques) and the subsequent deposition and growth of materials on the substrate. The objective is to materialize a physical circuit that adheres as closely as possible to the intended design.

Characterization stage involves a quantitative assessment of the extent to which the fabricated product conforms to the design. This includes the specification of physical dimensions and the verification of material properties as planned, such as structural, optical, or electrical characteristics. It focuses on evaluating the morphology, material composition, and uniformity of the final product.

The ideal workflow in circuit synthesis inherently incorporates feedback mechanisms, particularly between the characterization and production stages. These feedback loops are crucial, as systematic measurements of Metrics of Interest (MOIs) contribute significantly to the establishment of robust protocols. They facilitate the identification of critical Process Control Parameters (PCPs) and their impact on the final product. The four stages above correspond approximately to the transition from the **Technical Feasibility** phase to the **Design & Verification** phase, as conceptualized in the Six Sigma framework for product development[6, 7]. This alignment underscores the emphasis on achieving high reproducibility and precise control in synthesis processes akin to high-level industrial production.

1.2 Quality in quantum technology

In the realm of quantum computing technology, *quality* emerges as a paramount concern. Relating back to the stages outlined in section 1.1, quality is primarily the product of meticulous control during the production phase, and its extent is revealed through subsequent characterization. In the context of quantum technology, the term "quality" often equates to *material quality*, more or inversely related to the density of material defects. Structural imperfections such as phase variations, grain boundaries, vacancies, impurities, and dislocations invariably compromise the integrity of quantum devices.

Ref. [8] presents a pivotal study demonstrating statistical variations in the performance of superconducting qubits based on different deposition techniques. Notably, niobium qubits fabricated via sputtering exhibited superior performance compared to other methods. This indicates that the microstructure and chemical composition of the Nb films, determined by the deposition technique, are critical factors influencing qubit relaxation times. Variations even within different sputtering techniques were noted, pointing to discrepancies in suboxides and oxygen vacancies. These

defects can absorb energy from qubits, reducing coherence and impairing performance. A comprehensive review from 2021, ref. [9], highlights primary loss channels in superconducting qubits, including surface and interfacial defects, as well as microscopic charge and spin defects. These insights underscore the importance of understanding and controlling material defects to bolster qubit coherence and overall device performance.

The key message here is that material quality stands as a critical bottleneck for cutting edge quantum devices, affecting their lifetime, fidelity, and overall functionality. Hence, achieving high purity and precise control over all process parameters is essential for the successful synthesis of quantum circuits.

Qubit platforms

Numerous platforms for quantum computing have been proposed, each leveraging distinct physical principles to construct and operate two-level systems, thereby imparting unique attributes in terms of design, physical parameters, tolerances, and respective strengths and weaknesses.

This thesis concentrates on the synthesis of components for **superconducting** and **topological** qubits. The relevance for the latter platform is mostly due to its reliance on III/V semiconductor materials and specific morphological features. III/V semiconductors are also highly pertinent to the photonic qubit platform, suggesting that the synthesis considerations discussed here should also apply to the development of photonic qubit components. Given its extensive study and advanced state, the superconducting platform will serve as our main example. Consequently, a brief overview of a fundamental superconducting qubit is appropriate, serving both an explanatory and illustrative purpose.

The superconducting qubit

In its simplest form, a superconducting qubit comprises three key elements in a circuit configuration, as depicted in a conceptual manner in figure 1.4. These components are characterized by three fundamental energy types: the charging energy E_C, the Josephson energy E_J, and the inductive energy E_L. This archetypal configuration gives rise to a Hamiltonian that can be formulated utilizing these energy quantities:

$$\hat{H} = E_c\left(\hat{n} - n_g\right)^2 - E_J\cos\left(\phi\right) + E_L\frac{\left(\hat{\phi} - \phi_e\right)^2}{2} \tag{1.1}$$

$$E_C = \frac{(2e)^2}{2\left(C + C_J\right)} \qquad E_J = \frac{\hbar I_0}{2e} \qquad E_L = \frac{\hbar^2}{4e^2 L} \tag{1.2}$$

In the Hamiltonian above, $\hat{n}$ represents the island charge, while $\hat{\phi}$ denotes the phase difference across the Josephson Junction (JJ). Resolving

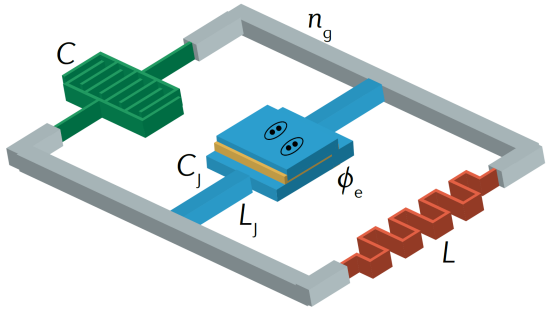

Figure 1.4: **A basic superconducting qubit:** A Josephson junction (JJ) circuit qubit with basic elements: capacitance (green), Josephson junction (blue) and inductance (red). The circled pairs on the JJ illustrate Cooper pairs tunnelling through the dielectric barrier. Figure adapted from ref. [9].

this Hamiltonian for its eigenvalues yields an energy landscape, contingent upon the energy parameters, where the quantization of charge and flux manifests as discrete energy states. The interplay among the three characteristic energies specified in equation 1.2 is adjustable, and their relative magnitudes – often expressed in ratios like E_J/E_C and E_L/E_J – define the energy landscape, thereby determining the type of superconducting qubit[9–11].

In summary, the discrete states of a qubit is dictated by the energies in equation 1.2, which in turn are determined by the characteristics of the components they represent, such as material constants, dimensions, and distances. Direct manipulation of the materials and dimensions of these components translates, albeit in a complex manner, into control over qubit parameters. Consequently, each component is meticulously designed, with precise dimensions outlined, often as a result of extensive modelling in finite element method (FEM) software.

1.3 Patterning techniques

With a detailed design at hand, the next phase involves transforming this design into a tangible circuit on a chip. Different qubit platforms necessitate distinct designs, with the realization of qubits in various physical systems. These designs may incorporate elements like nanowires, quantum dots delineated by electric potential gating, extended nanowire networks, capacitor pads, and superconducting circuits including Josephson junctions, just to mention a few.

To faithfully realize these sophisticated nanoscale designs, precision in lateral patterning is paramount. The success of self-assembly in aligning different materials into specific patterns relies on the ability to accurately demarcate regions for material deposition and growth. This patterning

process constitutes the core focus of this thesis, and we will primarily distinguish between two main branches of patterning methods.

Mask-on-substrate based techniques utilize a mask deposited directly onto the substrate. The pattern is defined through the selective removal of parts of this mask. Subsequent growth or deposition of the desired material occurs with the mask in place, adhering to the substrate. After deposition, the mask material can be removed in a post-processing phase. This technique is explored in greater detail in part II of the thesis.

Stencil based techniques involve the use of a stand-alone stencil with predefined patterns. Similar to the mask, openings or apertures in the stencil determine the deposition pattern. The stencil is then positioned above the substrate, and deposition or growth is conducted with the stencil in a fixed position. After completion, the stencil is removed. Stencil based methodologies are examined in part III of this thesis.

We acknowledge that some studies adopt hybrid methodologies, incorporating both a substrate-attached mask and a stencil to selectively inhibit deposition in specific areas[12]. Hybrid strategies facilitates enhanced pattern control over multiple deposition processes within a single device. Although this thesis does not delve further into hybrid techniques, the principles governing these approaches essentially combine the characteristics of the mask-on-substrate and stencil based methods described earlier. In our later argument in favor of the stencil based technique, our primary rationale centers on the complete circumvention of resist materials on the substrate, which is an inherent limitation in the traditional mask-on-substrate approach for synthesis of quantum devices – a limitation which would also apply in the case of a hybrid approach.

2

Crystal growth basics

The theory of crystal growth and morphology also played a central role in my Master's thesis, ref. [13], and the essence of the explanations with central equations therefore appear in said reference as well. In both cases, the basic theoretical framework of transition state kinetics largely follows that of Krogstrup et al. (2013), ref. [14].

2.1 Why crystal growth?

In the realm of classical macroscopic engineering, top-down methodologies are effective when materials and components can be either mechanically arranged or sculpted from larger structures. However, the inherent size sensitivity of quantum systems necessitates a different approach. Qubit designs typically range in size from approximately 100nm to a few millimeters in one dimension. Despite the seemingly larger dimensions of some systems, precision in patterning remains crucial, as small variations translate to deviations in qubit characteristics, resulting in reduced coherence and impaired performance. Thus, "quality" in the realization of design is not only about fidelity to the intended pattern but also about controlling morphology as it ultimately impacts device performance.

Given that direct mechanical manipulation is incompatible with the required precision level, quantum circuit fabrication adopts a bottom-up approach. In this approach, conditions are meticulously arranged to promote self-assembly into the desired configurations; quantum circuits are essentially crafted through controlled crystal growth. While the latter sections of this thesis predominantly focus on controlling flux distributions, it is crucial not to oversimplify circuit synthesis as merely depositing materials into pre-defined mask apertures. Indeed, high-resolution control of flux distribution is a significant aspect, as will be demonstrated. However, it is essential to remember that our influence is exerted on the input side, with the final output being the culmination of atomic self-assembly governed by the principles of thermodynamics and kinetics.

Beginning with a broad overview of these fundamental principles, we can develop an initial understanding of crystal growth, conceptualizing it as atoms undergoing various transitions on the substrate. From this starting point, we can move towards a phenomenological account of different growth modes, essentially representing the collective behavior of atomic ensembles operating under these physical rules.

2.2 Introduction to crystal growth

A multitude of systems exist for material deposition, each tailored to specific requirements in terms of conditions, materials, and control precision. Among these, ultra-high vacuum (UHV) Molecular Beam Epitaxy (MBE) systems stand out for their exceptional purity and control capabilities, making them the preferred choice for the growth of high-quality semiconducting and superconducting quantum devices. This thesis will provide a cursory description of an MBE system, highlighting its most critical features and the implications of this type of production process and growth environment for the bottom-up synthesis of quantum circuits. A comprehensive exposition of MBE systems is beyond the scope of this work but can be found elsewhere[15].

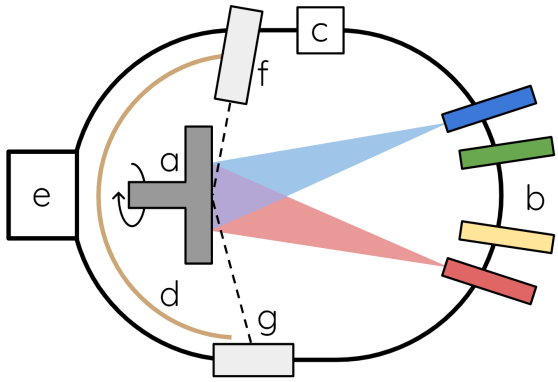

Figure 2.1: **MBE chamber schematic:** a) Rotating substrate holder and heater. b) Effusion cells. c) Vacuum pumps. d) Cryo shrouds. e) Shutter. f) RHEED gun. g) RHEED flourescent screen. Further explanations in main text. Figure adapted from ref. [13].

Subsequently, the thesis will offer an introductory overview of crystal growth within the MBE-type environment. While a thorough examination of crystal growth modes and phenomena could constitute a substantial review or even a dedicated PhD thesis (examples include refs. [16, 17]), the focus here will be on outlining key phenomena and trends that shed light on the challenges inherent in crystal growth and may suggest avenues for controlling such growth in the context of circuit synthesis.

Crystal growth setup

As previously noted, the MBE system functions under ultra-high vacuum conditions. Figure 2.1 provides a schematic representation of an MBE growth chamber, illustrating its essential components. The growth substrate is affixed to a rotating holder and heater, with rotation promoting uniform material distribution. Temperature control plays a pivotal role in MBE growth, serving as a primary process control parameter. The independently operable effusion cells emit beams of single-element particles for deposition onto the substrate, each positioned at a fixed location relative to the substrate holder. Ultra-high vacuum pumps are instrumental in eliminating undesirable atoms from the system, achieving base pressures in the range of 10^{-10} to 10^{-12}Torr, depending on specific system configurations, wafer types, and cleaning protocols[15]. Cryo shrouds further enhance the pristine condition of the environment by capturing residual atoms within the chamber. The shutter represents the entrance to the growth chamber, while the reflection high-energy electron diffraction (RHEED) components enable in-situ monitoring of the growth process.

The ultra-high vacuum environment is a critical prerequisite for achieving high levels of cleanliness in the MBE process. The near-absence of

unwanted atoms in this environment inherently helps minimize the introduction of impurities. In the MBE system, effusion cells are used for the deposition of ultra-clean elemental precursors. Under optimally selected conditions, these precursors self-assemble into a solid-phase crystal on the chosen substrate. The system provides the user with precise control over temperature and molecular beam pressures in an ultra-pure setting. Additionally, the ultra-high vacuum conditions simplify the system in theory, reducing it to a substrate exposed to controlled atomic beams from effusion cells.

2.3 Crystal growth adatom kinetics

III/V semiconductors are of particular interest due to their significance in semiconductor technology and their unique properties relevant to topological and photonic quantum systems. They provide an insightful case study for this research. Our exploration of crystal growth from adatom kinetics will primarily focus on these semiconductors. Simplified simulations of adatom diffusion in III-V semiconductor growth often only track the group III species[1], assuming an ample group V overpressure to ensure the availability of group V species whenever required[20–22].

Drawing on existing literature[23, 24], we assume an atomically flat substrate as the initial condition, unless stated otherwise. In certain scenarios, we may need to account for a density of atomic steps due to wafer miscut or the impact of roughness from an existing step on growth conditions, but these are neglected in the first approach. The activity of adatoms is considered to be confined to one "adsorption layer" (bilayer) at the surface of the growing crystal, at the interface between the crystal and vacuum. While some activation in layers beneath this is possible, the rates of these secondary layer activations are deemed significantly lower, rendering their effects negligible. The group III species is represented with a normalized density $\rho \in [0,1]$, corresponding to the proportion of occupied lattice sites in the adsorption layer. At an atomic level, a lattice site is either occupied or unoccupied, but considerations of average density become more relevant at larger scales, thus the continuous variable ρ.

The primary processes under consideration, representing the lifecycle of adatoms, include **adsorption**, **diffusion**, **decomposition**, **incorporation**, and **desorption**. The kinetics are based on transition rates, specifically the transitions associated with the aforementioned processes. Figure 2.2 illustrates the transition from a generalized state p to state q, governed by the free energy barrier between the two states.

The transition rate in these processes is contingent on the availability of the initial state, the attempt frequency, and the thermal energy requisite

[1] This simplification is not always employed, and some works do explicitly set up frameworks for tracking multiple species[14, 18, 19]. We will briefly come back to dual species tracking towards the end of this thesis.

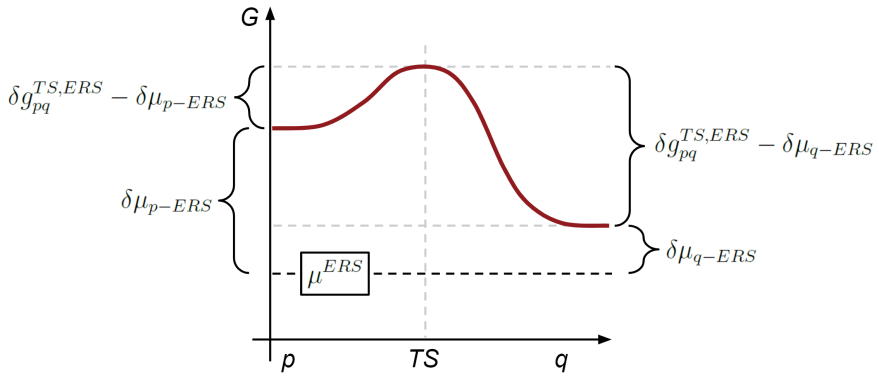

Figure 2.2: **Transition states:** The horizontal axis displays generalized states p and q, with a transition state TS between. The vertical axis displays the free energies of the states with respect to an equilibrium reference state ERS. This asymmetry of the transition is apparent, and transition from p to q requires overcoming a much lower effective barrier than vice versa. Figure adapted from refs. [13, 14].

for overcoming the barrier, which in turn dictates the probability of the transition. For clarity, we can define the effective height of the energy barrier "as seen from" state p:

$$\delta g_{pq}^{TS} \equiv \delta g_{pq}^{TS,ERS} - \delta g_{p-ERS} \tag{2.1}$$

which will determine the transition rate as an Arrhenius function[14, 25]:

$$\Gamma_{pq} = \rho_p \Xi_{pq} \exp\left(-\frac{\delta g_{pq}^{TS}}{k_B T}\right) \tag{2.2}$$

where Ξ_{pq} is the attempt frequency, and k_B is the Boltzmann constant. The net transition rate is then the difference between transitions back and forth:

$$\begin{aligned}\Delta\Gamma_{pq} &= \Gamma_{pq} - \Gamma_{qp} \\ &= \rho_p \Xi_{pq} \exp\left(-\frac{\delta g_{pq}^{TS}}{k_B T}\right) - \rho_q \Xi_{qp} \exp\left(-\frac{\delta g_{qp}^{TS}}{k_B T}\right)\end{aligned} \tag{2.3}$$

We now turn our attention to the atomistic processes and describe their effect on the time derivative of the adatom density.

Adsorption

Adsorption is the process where incoming atoms transition from a molecular beam state to adatoms on a surface, specifically becoming loosely

bound to the substrate. These atoms originate from the beam of the effusion cells, denoted as F. A widely employed approximation in this field is that of a constant and uniform beam flux across the substrate. Indeed, the rotation of the substrate holder during MBE growth is a strategy meant to help promote even flux distribution.

The adsorption process is typically described with the inclusion of a sticking coefficient, Λ, which represents the fraction of incoming atoms that adhere to the surface, with the remainder reflecting back into the vacuum[23]. In the case of the group III species adsorbing as single atoms, it is logical to expect the sticking coefficient to scale linearly with the availability of vacant lattice sites. However, empirical findings suggest that the sticking coefficient for group III species can be approximated as close to unity[26, 27]. This is attributed to the fact that the hopping rate (discussed in section 2.3) significantly exceeds the deposition rate, thereby enabling group III species to rearrange for adsorption regardless of the initial state of the surface.

Putting these assumptions together results in the simple rate equation:

$$\left.\frac{\partial \rho}{\partial t}\right|_{\text{beam}} = F \quad \text{(uniform constant)} \tag{2.4}$$

Diffusion

Diffusion refers to the spatial distribution over time, in our context, the movement of adatoms across the surface prior to their eventual incorporation or desorption. The concept of diffusion was initially explored through the study of salt concentration diffusion in a water solution, where Fick[28] observed that the flux of salt exhibited a linear relationship with the concentration gradient, analogous to the diffusion of heat in a solid body.

Diffusion is typically described using Fick's second law:

$$\left.\frac{\partial \rho(x,t)}{\partial t}\right|_{\text{diffusion}} = \nabla \cdot \Big(D(x,t) \nabla \rho(x,t) \Big) \tag{2.5}$$

where $\rho(x,t)$ is the concentration of the group III species, and ∇ is the differential operator. In the case of a uniform diffusion coefficient, D, this simplifies to:

$$\left.\frac{\partial \rho(x,t)}{\partial t}\right|_{\text{diffusion}} = D \nabla^2 \rho(x,t) \tag{2.6}$$

which is of a form similar to the heat equation. The scenario with a uniform diffusion coefficient is frequently examined due to the robustness of this model[21, 29]: while the diffusion *length* of the group III species may be influenced by variables such as the density of group V species, this dependency arises from changes in the lifetime due to termination via incorporation (as discussed in section 2.3), rather than alterations to

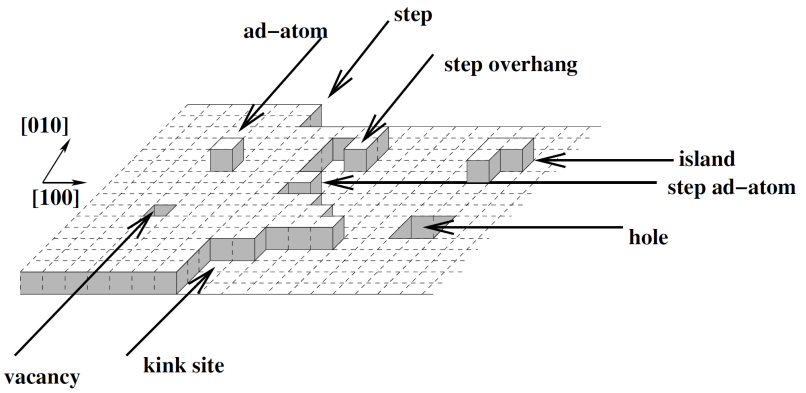

Figure 2.3: **Kossel crystal:** The simple Kossel crystal surface is shown with a few of the different features which may arise in crystal growth. Note the cubic appearance of each atom, which leaves a crystal layer represented as a flat surface. Figure adapted from ref. [17].

the diffusion characteristics. The constancy of the diffusion coefficient reflects the independence of the diffusive hopping rate and probability of transitioning to each neighboring site from other transition events, such as desorption into a gaseous state or incorporation into the solid crystal. Thus, even in analyses where the diffusion characteristics of group III atoms are evaluated in relation to the availability of group V species[30, 31], a uniform diffusion coefficient D can be implicitly assumed.

In reality, crystals manifest in a vast array of structures, and a comprehensive representation of these is beyond the scope of this thesis. The Kossel crystal model, albeit a simplification, provides an insightful conceptual framework for understanding the growth and structure of crystalline materials. Figure 2.3 illustrates a Kossel crystal, depicting a crystal surface during growth, complete with steps, kinks, adatoms in motion, and the formation of islands. In this model, each atom is represented as a cube, with the perfect crystal being a closely packed arrangement of these cubes in orderly rows and layers. Essentially, crystal growth occurs as atoms integrate into the existing cubic structure.

Focusing on diffusion, the specific form of equation 2.3 for a given site on a Kossel crystal surface results in a net rate of change at site p:

$$\begin{aligned}\left.\frac{\partial \rho_p(t)}{\partial t}\right|_{\text{diff}} &= \sum_q \Delta\Gamma_{qp} \\ &= \sum_q \left[\rho_q \exp\left(-\frac{\delta g_{qp}^{TS}}{k_B T}\right) - \rho_p \exp\left(-\frac{\delta g_{pq}^{TS}}{k_B T}\right)\right]\end{aligned} \tag{2.7}$$

Here, the index q runs the neighboring lattice sites. As indicated by the presence of densities ρ_p and ρ_q in equation 2.3, random hopping

between two identical lattice sites leads to a net movement from sites that are, on average, more densely populated to those that are less so. This random walk of adatoms effectively distributes the concentration from higher-density regions towards lower-density regions.

Incorporation and decomposition

Incorporation is the process by which an adatom transitions to becoming an integral part of the solid crystal structure. Conversely, decomposition refers to the reverse process, where an atom dissociates from the solid state to revert to an adatom. Analogous to the discussion in section 2.3, the net decomposition rate is the difference between the rates of decomposition and incorporation:

$$\left.\frac{\partial \rho(x,t)}{\partial t}\right|_{\text{inc}} = \Delta\Gamma_{sa} \tag{2.8}$$

$$= \kappa_{sa} - \kappa_{as}\rho(x,t) \tag{2.9}$$

In this equation, the positive term on the right side (κ_{sa}) represents the decomposition rate of the existing crystal. This coefficient is dependent on temperature and the local atomic configuration, i.e., how the local atoms are bound to the crystal, which varies with the arrangement of neighboring sites. A factor of $(1-\rho(x,t))$ is omitted for the same reasons outlined in section 2.3. Often, for the sake of simplicity, the decomposition rate is assumed to be negligible ($\kappa_{sa} = 0$). The negative term on the right corresponds to incorporation, where adatoms transition into the solid state. This rate is expected to be proportional to the availability of the group III species, characterized by the Arrhenius-type coefficient κ_{as}.

Desorption

Desorption refers to the phase transition from the adatom state to a gaseous state, effectively leaving the surface and dispersing into the vacuum, where atoms are captured by the MBE system's cryo shrouds or expelled by the ultra-high vacuum pumps. Drawing from literature[24], it is noted that group III atoms predominantly desorb as individual atoms[32, 33]. The desorption rate of group III species is thus expected to be linearly proportional to the normalized adatom density:

$$\left.\frac{\partial \rho(x,t)}{\partial t}\right|_{deso} = -\gamma_{av}\rho(x,t) \tag{2.10}$$

where γ_{av} represents the temperature-dependent desorption rate constant, which is also anticipated to adhere to an Arrhenius relationship.

Adatom density equations

Integrating the insights from section 2.3 and its subsections, we can formulate a differential equation representing the behavior of group III species (with implicit dependencies on spatial position x and time t):

$$\frac{\partial \rho}{\partial t} = F + D\nabla^2\rho + \kappa_{sa} - \kappa_{as}\rho - \gamma_{av}\rho \tag{2.11}$$

$$= D\nabla^2\rho - \rho\left(\gamma_{av} + \kappa_{as}\right) + \left(F + \kappa_{sa}\right) \tag{2.12}$$

where the terms in the first line encapsulate contributions from adsorption, diffusion, decomposition, incorporation, and desorption processes. The second line gathers these terms into a diffusion term, followed by a term linear in ρ and a constant term.

It is crucial to note that the coefficients governing the different transitions (D, κ_{sa}, κ_{as}, γ_{av}) are also functions of the local environment. For instance, an adatom on an atomically flat bare substrate surface will exhibit different behavior compared to an adatom adjacent to an atomic step. These environment-dependent variations become increasingly significant as we explore growth conditions in the subsequent sections. Moreover, many characteristics of crystal growth in various regimes (as introduced in section 2.2) stem from these local environmental differences. This is evident in phenomena such as nucleation with characteristic island sizes and step-flow growth, both of which are heavily influenced by local kinetic effects – more on nucleation below.

2.4 Crystal growth thermodynamics

While the previous section describes the kinetic processes that influence the density of group III adatoms on the substrate, it is also essential to consider the constant thermodynamic pressure towards equilibrium. In the context of crystal growth from adatom kinetics, this drive towards equilibrium, specifically towards a morphology that minimizes the excess chemical potential, is implicitly embedded in the locally dependent coefficients (D, κ_{sa}, κ_{as}, and γ_{av}). This thermodynamic force shapes the equilibrium structure of the crystal. Therefore, a basic understanding of the thermodynamics involved will enhance our comprehension of the morphologies and phenomena observed in crystal growth.

Starting from a basic free-floating crystal, we can consider the Wulff shape, which is the thermodynamically favored form for a given volume of a free-floating crystal. This shape minimizes the surface excess chemical potential[34]:

$$\delta\mu = \sum_{\mathrm{s}} \gamma_{\mathrm{s}} A_{\mathrm{s}} \tag{2.13}$$

Here, $\delta\mu$ represents the total surface excess chemical potential, expressed as a sum of products of surface energy density and the corresponding area for each surface. This thermodynamic optimization leads to a proportionality between the normal distance from the crystal center to a crystal face and the surface energy density of that face[35, 36]:

$$d_s = \lambda \gamma_s \tag{2.14}$$

where d_s denotes the aforementioned distance, and λ is a constant of proportionality[2]. Over time, a lower growth rate and higher temperature should allow the crystal to overcome kinetic barriers, evolving towards the thermodynamic shape through reconfiguration.

The direct link between surface energy density and morphology allows for the construction of the equilibrium shape if the surface energy density function $\gamma_{\mathrm{SED}}(\theta,\phi)$ is known. However, determining this function is a complex task, with values typically calculated for specific orientations or crystal termination facets via density functional theory (DFT)[37–40]. Consequently, the surface energy densities are functions of thermodynamic parameters like temperature and partial pressures. When the surface energy density for low-Miller index orientations is known, the method to derive the equilibrium morphology is referred to as the Wulff construction[34, 41]. From these known orientations, a two-dimensional approximation to the surface energy density function can be expressed as[14]:

$$\gamma(\theta) = \gamma_{\max} - \sum_{hkl} c_{hkl} \frac{I_{hkl}}{1 + \left((\theta - \theta_{hkl})/w_{hkl}\right)^2} \tag{2.15}$$

where $\gamma_{\max}$ is the maximum surface energy density, serving as a reference. The subtraction of the sum indicates the removal of a "dip" of depth I_{hkl} and width w_{hkl} in the function around each high-symmetry facet, with the hkl indices covering these facets. The coefficient c_{hkl} is retained separately, accounting for overlap adjustments between closely spaced neighboring facets. Plotting the value of the γ-function as the radial distance r as a function of angle θ, the Wulff construction entails drawing radial-normal lines at each point in the plot, with the resulting convex hull defining the equilibrium or Wulff shape. For a fully faceted morphology (shown in two dimensions), the resultant shape adheres to equation 2.14, as the radial distance is determined from the surface energy density. This procedure is illustrated in figure 2.4.

Returning to the discussion of crystal morphology and the thermodynamic equilibrium shape, a special case arises when a crystal grows on

[2] There is also a kinetic version of equation 2.14 with a proportionality between the distance mentioned for a given crystal face, and the growth rate on that crystal face: $d_s = \eta v_s$. In this description, that might be confused for the description of adatom kinetics in the previous chapter, and it has been omitted here.

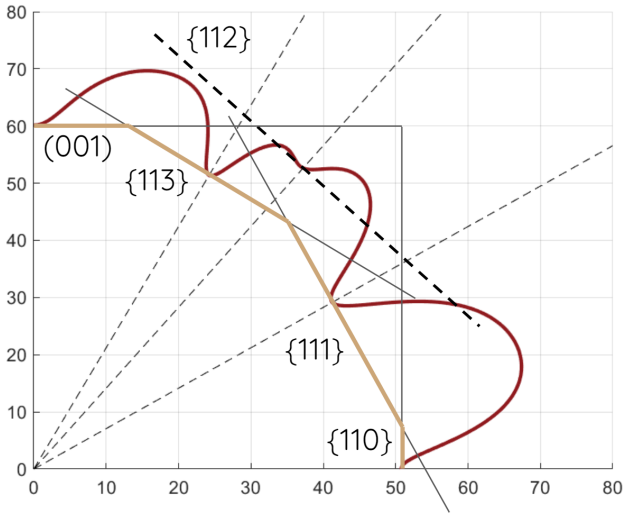

Figure 2.4: **Wulff construction:** An example of the γ-function from equation 2.15 is plotted in red for the <110> zone axis with. Radius-normal lines are drawn in principle at each point in the plot. The convex hull (sand color) is the Wulff shape. Note the {112} facet top right, which due to a high surface energy density does not appear in the final equilibrium morphology. Figure reproduced from ref. [13].

a substrate. The thermodynamic shape for a crystal attached to a surface is termed the Winterbottom shape[42]. This shape results from a minimization process akin to that in equation 2.13, but with an additional term accounting for the interface between the substrate and the growing species. It is noteworthy that the shapes discussed here exhibit self-similarity, meaning they remain consistent under scaling in a continuum framework. However, this scaling invariance does not hold when crystal growth is spatially constrained, such as being limited to specific areas of a substrate. In such cases, the resulting shapes may not conform to the typical categories described earlier. Nevertheless, the fundamental principle is that the thermodynamic shape represents a minimization of excess chemical potentials. For a more comprehensive understanding of crystal growth morphology modeling, interested readers are directed elsewhere[43].

This principle of thermodynamic minimization remains applicable even when additional terms are incorporated into the excess energy equation. In the context of heteroepitaxial growth – where one material is grown on a substrate of another, and the lattice structure of the substrate influences the growing species – the growing species experiences strain due to a lattice parameter mismatch. This strain adds to the overall excess chemical

potential:

$$\delta\mu = \delta\mu_{\text{surfaces}} + \delta\mu_{\text{interface}} + \delta\mu_{\text{strain}} = \sum_s \gamma_s A_s + \gamma_i A_i + \delta\varepsilon \tag{2.16}$$

Note that all terms in equation 2.16 depend on the crystal morphology. Therefore, any reconfiguration alters all terms simultaneously. Additionally, other, less significant energy terms have been omitted for simplicity, such as those associated with edges and vertices, which generally have a minor impact due to their lower dimensional nature. The interplay between these various energy components leads to intriguing phenomena, particularly in scenarios involving high-mismatch crystal growth. This topic, including the complexities of high-mismatch crystal growth and the role of misfit dislocations, will be delved into in greater detail in chapters 5 and 6.

Nucleation

Crystal growth is fundamentally about the systematic arrangement of atoms on a substrate, where chemical or elementary precursors are deposited and, under favorable conditions, additional layers are formed. These "favorable conditions" refer to a reduction in the chemical potential through the configuration of atoms into a crystalline structure. From an atomically flat substrate surface, the initiation of a new layer of growth requires nucleation. During this process, the randomly moving supplied adatoms occasionally meet up by chance, with two or more adatoms ending up in adjacent lattice sites to form a small cluster. The stability of this initial cluster hinges on the excess energy, which can be primarily decomposed into bulk and surface energy contributions. If we consider a single-layered cluster as having a circular shape, the Gibbs free energy of this cluster can be formulated as[17, 44]:

$$\Delta G = -\frac{\pi r^2}{a^2}\Delta\mu_{\text{bulk}} + 2\pi r\gamma_{\text{step}} \tag{2.17}$$

Here, the negative term represents the reduction in energy per atom ($\Delta\mu_{\text{bulk}}$) due to their incorporation into a bulk cluster, with a being the lattice constant. The positive term accounts for the energy cost associated with the formation of a step at the cluster circumference, where γ_{step} is the step energy density. Taking the derivative of equation 2.17 with respect to the cluster radius r yields a critical radius:

$$r_c = \frac{a^2\gamma_{\text{step}}}{\Delta\mu_{\text{bulk}}} \tag{2.18}$$

At this critical radius, the derivative of ΔG with respect to r changes from positive to negative, implying that any cluster reaching or exceeding

this size will find it energetically favorable to continue growing. Thus, nucleation is said to have occurred.

$$\Delta G_c = \Delta G(r = r_c) = \frac{\pi a^2 \gamma_{\text{step}}^2}{\Delta \mu_{\text{bulk}}} \tag{2.19}$$

The maximum of the Gibbs free energy at $r = r_c$ represents the barrier that limits the rate of nucleation. A schematic illustrating the free energy as a function of the cluster radius is depicted in figure 2.5 with the critical radius marked.

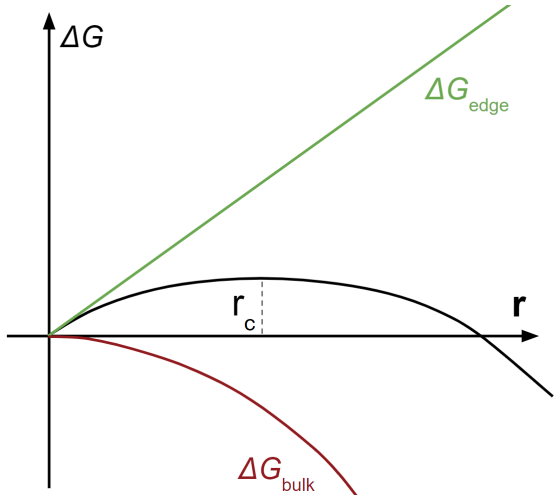

Figure 2.5: **Critical nucleation cluster radius:** The two terms of the free energy are shown in colors, with the negative bulk contribution in red, and the positive step energy in green. Increasing the cluster size is moving against the free energy derivative up to the critical radius r_c. Once the cluster grows to this critical size, additional growth is energetically favorable. The critical quantities are given in equations 2.18 and 2.19.

Growth modes

The assembly of atoms into the lattice structure is typically characterized by one of three distinct growth modes. These modes reflect the interplay between nucleation and the subsequent incorporation of atoms onto a cluster or at a step edge.

Frank-van der Merwe (FM) growth is colloquially known as **layer-by-layer** growth. This mode is prevalent when nucleation is relatively slow, characterized by a high nucleation barrier and thus low nucleation probability. In this regime, each layer completes its growth before another layer begins to nucleate on top. This indicates a propensity for adatoms

to preferentially incorporate at step edges or kinks. Key prerequisites for FM growth include sufficient temperature to allow adatoms to migrate to these preferred lattice sites and overcome potential barriers such as the Ehrlich-Schwoebel barrier when traversing a step edge[45, 46].

Volmer-Weber (VW) growth is typified by the formation of **clusters** or **islands**. In this scenario, clusters form at a significantly higher rate than the incorporation of atoms at step edges and kinks. Consequently, the growing surface becomes rough, with clusters randomly forming at characteristic sizes and densities determined by the growth conditions. It is noteworthy that island formation is not merely a consequence of random atomic assembly into layered structures; it also arises from factors like strain and surface energy excess chemical potentials.

Stranski-Krastanov (SK) growth represents a hybrid of the FM and VW modes. Initially, growth proceeds in the FM manner, but after a few layers, islands begin to form on top. The SK mode emerges from a competition between different contributions to the surface excess chemical potential and is commonly observed in systems such as InAs grown on GaAs[44, 47].

Step-flow is a phenomenon observed when the surface possesses a certain density of steps, often due to wafer miscut. Here, growth predominantly occurs at step edges without nucleation on the terraces. Each step edge advances uniformly, leading to a synchronized "flow" of all step edges. Though not a growth mode per se, step-flow growth is a significant phenomenon that manifests under certain growth conditions. **Spiral** growth is a related phenomenon where a step edge is consistently available due to the presence of a screw dislocation, and growth proceeds primarily by advancing this step edge in a circular fashion around the dislocation line.

The key insights to be drawn here revolve around the intricate relationship between growth rate and the resulting growth modes. This relationship is nuanced and subject to various influencing factors. However, in the context of homoepitaxial growth, where misfit strain does not affect the morphology of the growing film, certain general trends can be observed: 2-dimensional growth is more likely at higher temperatures and slower growth rates, while 3-dimensional growth is favored by higher growth rates and lower temperatures[3]. These trends can be better understood by considering specific cases:

Low temperature limit: Here, the deposited species lacks sufficient energy to overcome barriers for transitioning between lattice sites. The atoms

[3] One noteworthy caveat to this trend is the temperature for roughening transition T_R, where an otherwise smooth surface becomes rough due to thermal fluctuations.

effectively adhere to the substrate in a "hit-and-stick" manner, landing and remaining more or less stationary where they first make contact with the substrate. While the distribution of atoms should be statistically uniform, stochastic fluctuations often result in a rough surface.

High temperature limit: In this scenario, the deposited species has enough energy to migrate on the substrate until a favorable site for incorporation is encountered, such as a kink or step edge. This mobility facilitates a smoother surface formation as vacancies are readily filled through incorporation. However, it is crucial to note that this "high temperature" scenario is more about finding the optimal temperature for Frank-van der Merwe (FM) growth than merely increasing the temperature indefinitely. At excessively high temperatures, decomposition becomes a significant factor, and smooth growth is not straightforwardly assured.

The understanding of the physical principles underlying these growth phenomena is vital, especially when reviewing experimental observations in chapter 5. Additionally, this conceptual framework is instrumental in discussing the interplay between flux distribution input and crystal growth output in chapter 9, where these dynamics are explored in greater detail.

Part II

Mask-on-substrate based techniques

3

Mask-on-substrate based techniques

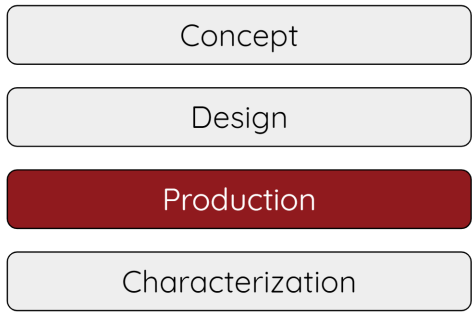

Figure 3.1: **Synthesis production stage:** This stage relates to the actual realization of the design, the physical production or synthesis of the circuit.

Having introduced the basics of circuits and crystal growth, it is time to turn our attention towards how designs are realized in fabrication. We briefly touched on this back in section 1.3, and our first in-depth look is dedicated to the mask-on-substrate techniques. As a technique for realizing designs, it pertains mostly to the production stage, although the choice in patterning technique also influences the design stage.

3.1 Introduction to mask-on-substrate

The "lift-off" technique, a widely used mask-on-substrate approach, represents an efficient method for pattern creation in the fabrication of components and circuits. This process is distinguished by its straightforward approach to depositing material uniformly and then selectively removing unwanted regions[47], as illustrated in figure 3.2.

The key steps of the lift-off technique (simplified) are as follows:

1. **Mask application:** A resist mask, typically a polymer, is applied to the substrate. This mask is spun onto the substrate and then soft baked to help set it in place.

2. **Exposure:** The mask is exposed to ultraviolet or electron beam lithography, targeting specific regions. This exposure makes the targeted areas of the mask more susceptible to etching. The mask is then hard baked, stabilizing the resist.

3. **Developing/etching:** In the development step, the exposed parts of the mask are removed by etching, leaving behind an inverse representation of the desired pattern.

4. **Material deposition:** A uniform layer of material, often a metal, is then deposited over the entire surface, covering both the substrate and the remaining mask.

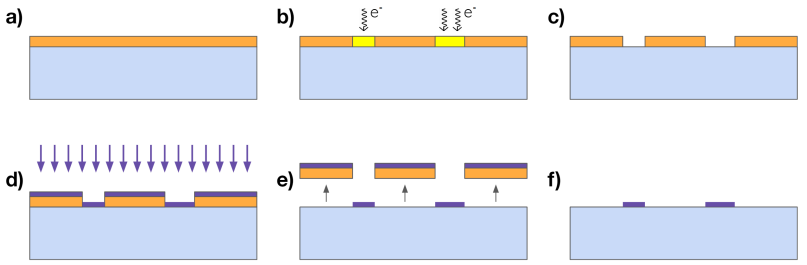

Figure 3.2: **Lift-off with resist mask: a)-c)** A resist layer (orange), typically a polymer, is "spin coated" onto the substrate (light blue). The lateral pattern is then traced out e.g. with electron beam lithography, and chemical development removes the parts of the mask previously exposed. **d)** The material (e.g. metal) is deposited. **e)-f)** The "lift off" of the remaining mask leaves only the intended structure behind.

5. **Lift-off:** The final step involves removing the remaining mask. This "lift-off" process leaves the deposited material only in the areas where the mask was initially etched away, thus creating the intended pattern on the substrate.

This process can be repeated with various patterns and materials to fabricate complex components and circuits. The technique described here employs "positive resist," meaning that the parts of the mask exposed and subsequently developed are those that are removed. In contrast, a "negative resist" process would involve the removal of non-exposed parts during development, leaving the exposed sections intact. While there are several variations of mask methods, the basic concept outlined above provides a fundamental understanding of the lift-off technique.

Selective Area Growth (SAG), also known as Selective Area Epitaxy, is a prominent technique in semiconductor nanofabrication, recognized for its precision and effectiveness in patterned growth[48]. This method utilizes an amorphous mask, often made of an oxide like SiO_2, with a thickness typically in the range of tens of nanometers. The mask is deposited onto the substrate, and as with the lift-off technique, openings are defined through lithographic exposure and etching. This leaves the mask as a negative of the desired growth pattern.

The core principle of SAG is the meticulous adjustment of thermodynamic conditions during epitaxial growth[49]. These conditions are optimized so that the deposited material preferentially nucleates and grows in the exposed regions of the substrate, while primarily desorption occurs on the mask surface. Although the growth species impinges across the entire surface, selective thin film layer growth is facilitated only in the designated regions, with minimal or no undesired growth on the mask.

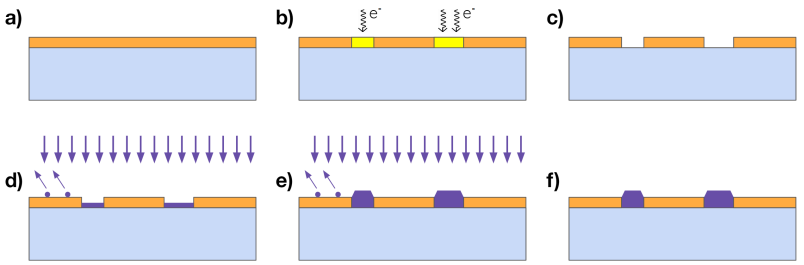

Figure 3.3: **Lateral patterning with SAG mask: a)-c)** An amorphous oxide layer (orange), typically e.g. SiO_2, is deposited onto the substrate (light blue). The lateral pattern is then traced out with electron beam lithography, and a removal procedure strips the parts of the mask previously exposed to the electron beam. **d)-f)** The material (e.g. III/V semiconductor) is deposited under specific thermodynamic conditions prohibiting growth on the mask, leading to selective growth in the trenches. Schematic shows faceted crystal shapes which commonly occur for e.g. III/V semiconductors due to a highly anisotropic surface energy density function.

This is depicted in figure 3.3.

The fundamental distinction between lift-off and SAG lies in their approaches to selectivity:

- **Lift-off:** This technique focuses on the end result in the exposed areas, with less concern for the mask which will be removed afterward. Commonly used for deposition rather than growth, lift-off often operates at lower temperatures where kinetic and thermodynamic influences are minimal. The mask functions similarly to masking tape used in painting: paint is applied broadly and then removed with the tape to reveal the desired pattern.

- **SAG:** In contrast, SAG involves tuning the conditions for crystal growth versus mask behavior. This is done by adjusting parameters such as D, κ_{sa}, κ_{as}, and γ_{av} from equation 2.12, to promote growth on the exposed substrate while inhibiting it on the amorphous mask[P1, 49]. Extending the painting analogy, this is akin to priming the surface, such that the paint adheres only to specific surfaces.

$$\frac{\partial \rho}{\partial t} = D\nabla^2\rho - \rho\left(\gamma_{av} + \kappa_{as}\right) + \left(F + \kappa_{sa}\right) \tag{3.1}$$

Equation 3.1 is equivalent to equation 2.12, but it emphasizes the control parameters integral to SAG patterning. While control remains indirect

and adjustments in temperature and pressures affect all parameters concurrently, the stark contrast in conditions between the exposed substrate and the masked areas underpins the selectivity in the technique.

3.2 Basic mask-on-substrate simulations

In order to analyze the effects of varying parameters in equation 2.12, simulation approaches, particularly mean-field models, are quite useful. These models focus on large-scale mass transport and general material distribution, rather than intricate atomic-level details. Simplifying the problem to a one-dimensional perspective can provide insights into diffusion characteristics and help interpret outcomes seen in simulations. From equation 2.12, we can derive a simplified one-dimensional version for analysis:

$$\frac{\partial \rho}{\partial t} = F + D\frac{\partial^2 \rho}{\partial x^2} + \kappa_{sa} - \rho\kappa_{as} - \rho\gamma_{av} \tag{3.2}$$

Assuming negligible decomposition and probing the steady state, we can simplify this to:

$$D\frac{\partial^2 \rho}{\partial x^2} = \rho\left(\kappa_{as} + \gamma_{av}\right) - F \tag{3.3}$$

It's important to note that seeking steady-state solutions is an approximation. Actual crystal growth, characterized by phenomena like cluster nucleation, disrupts equilibrium by inducing rapid changes in conditions. Nonetheless, steady-state solutions can reveal trends, with the understanding that quantities like the rates in equation 3.3 are now "suitably averaged." For instance, κ_{as} becomes an average incorporation rate of adatoms, inclusive of nucleation events necessary for growth initiation. This averaging process results in a κ_{as} that differs subtly from the rate an adatom might encounter at a step edge in an atomistic simulation where all local conditions are precisely accounted for.

Considering a setup with an exposed trench surrounded by masked areas, as shown in figure 3.3, we can draw some preliminary conclusions. Figure 3.4 presents a simplified version of this setup. Symmetry dictates that there should be no net flux at the outer boundaries ($J(x_0) = J(x_3) = 0$). Additionally, from the principle of mass conservation, the flux approaching any boundary from one side should match the flux leaving the opposite side of the same boundary:

$$\lim_{x \to x_n^-} J(x_n) = \lim_{x \to x_n^+} J(x_n) \tag{3.4}$$

This requirement ensures that a boundary does not act as a sink or source. For boundaries x_1 and x_2, this balance involves parameters influ-

enced by both the crystal and the mask, reflecting the interplay between different growth conditions:

$$\lim_{x_m \to x_{1,2}} D_m \frac{\partial \rho}{\partial x} = \lim_{x_c \to x_{1,2}} D_c \frac{\partial \rho}{\partial x} \tag{3.5}$$

where Equation 3.5 stems from Fick's first law, $J = -D\,\partial\rho/\partial x$, signifying a Neumann boundary condition on the first-order derivative at each boundary. In this context, m and c subscripts denote mask and crystal, respectively, aligning with the designations in figure 3.4.

For the outer boundary, which is far from the "active region," we implement a Dirichlet type boundary condition. Under the assumption of steady state and no net diffusion (as per equations 2.12 and 3.2), we can establish:

$$\rho_{\text{far away}} = F \big/ \left(\kappa_{as} + \gamma_{av}\right) \tag{3.6}$$

This implies a fixed value for the adatom density at the outer boundary. The assumption of "far away" also justifies a zero derivative Neumann condition at this boundary, which aligns with zero flux according to Fick's first law.

Although diffusion coefficients may vary between regions, the boundary condition in equation 3.5 necessitates that the first-order derivative maintains the same sign on both sides of a boundary. Focusing on the central crystal region, we can infer that adatom density should be symmetric. Whether this region represents a maximum or minimum in density depends on the sign of the second-order derivative in equation 3.3, with a negative sign indicating a maximum and a positive sign a minimum[1].

Figure 3.4 illustrates the valid solution types for this setup. The constraints of vanishing derivatives at the outer boundaries and the maintenance of the first-order derivative sign across boundaries lead to three viable solution types. The flat distribution is a trivial solution that satisfies all boundary conditions. The dotted line solutions in figure 3.4 fail to preserve the sign of the first-order derivative at the boundaries, resulting in a boundary acting as a sink (dotted red) or source (dotted green). These general trends persist when extending the analysis to two dimensions and including additional regions.

The diffusion equation 3.3 can be numerically solved using a `FiPy` environment, which allows for the definition of regions with varying conditions. This is particularly useful for more complex layouts than the simple ones shown in figure 3.4. Figure 3.5 presents a sample solution, analogous to the solid red line in figure 3.4. In the upcoming chapter 4, we will explore another solution of this type, applied to a more intricate design, based on studies of growth rates for arrays of nanowires in ref. [P1].

[1] The value of the second order derivative is allowed to vary across the region as prescribed by equation 3.3, but the sign is constant.

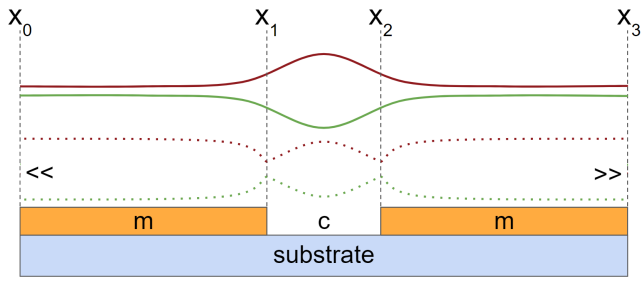

Figure 3.4: **Simple diffusion solution types:** Our simplified setup for initial observations. Orange is amorphous mask covering the entire substrate except for our small exposed region between x_1 and x_2. The points x_0 and x_3 are very far away, position not shown to scale. Solid graphs on top sketch valid solution types for negative (red) and positive (green) second order derivates on the crystal region. The first order derivates vanish at the outer boundaries, and the first order derivates carry their sign across internal boundaries. Dotted graphs on the bottom show invalid "solutions", where the sign of the first order derivative is not carried correctly.

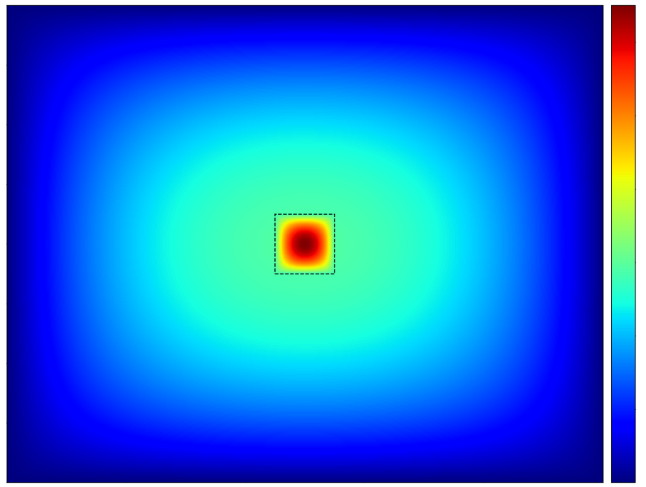

Figure 3.5: `FiPy` **sample solution:** A sample solution for a region of exposed substrate surrounded by mask on all sides. Colorbar denotes adatom density in arbitrary units. The lack of notation reflects the fact that this is a solution type, corresponding to the red line in figure 3.4. The way in which the adatom density tapers off depends on input parameters D, κ_{sa}, κ_{as}, and γ_{av} for both mask and crystal.

4

Selective Area Growth rates

The following chapter is based on my contributions to the paper *"Selective area growth rates of III-V nanowires"*, ref. [P1], which among other things is a study of how the design parameters influence the Selective Area Growth rates of nanowire arrays. Some figures and sections of text here therefore appear in adapted form or directly in the work referenced above.

The growth rates in Selective Area Growth is – to no surprise – very much in the production stage. Understanding and controlling the growth rates is intricately tied to successful realization of designs.

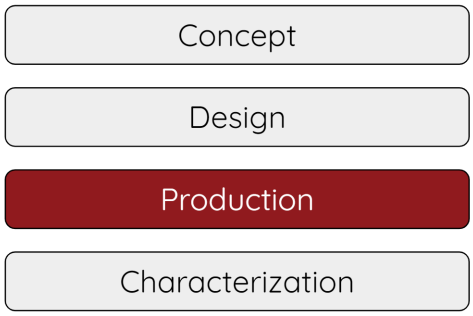

Figure 4.1: **Synthesis production stage:** This stage relates to the actual realization of the design, the physical production or synthesis of the circuit.

4.1 Design dependence

The initial portrayal of Selective Area Growth (SAG) in chapter 3 might lead to a simplistic understanding of the process as mostly filling trenches defined in an amorphous mask through electron beam lithography. However, as discussed in chapter 2, the essence of SAG lies in the meticulous control of conditions conducive to crystal growth.

The paper titled "*Selective area growth rates of III-V nanowires*", ref. [P1], delves into the complexities of growth rates for nanowires fabricated using the SAG method. As introduced in earlier chapters, the selectivity in SAG is attained by manipulating the differential parameters between regions of the crystal and the mask. This study challenges a simplistic interpretation of SAG as just filling trenches and underscores the necessity of a profound understanding and control over the crystal growth process.

Key findings of the paper are derived from examining arrays of four nanowires, where two are classified as "inner" nanowires, each flanked by two immediate neighbors, and two as "outer" nanowires, each having only one immediate neighbor. The growth rates of these nanowires, which vary based on design parameters like nanowire width and pitch, were determined by calculating the volume of crystal incorporated. This was characterized post-growth using atomic force microscopy (AFM) and transmission electron microscopy (TEM). Growth rates are expressed in "nominal units," where a unit value corresponds to the volume for a large planar section under identical growth conditions. Thus, growth rates are presented "relative to a corresponding planar growth rate". One of the principal conclusions is that growth rates are intrinsically linked to the specific design employed, with different parts of the design exhibiting

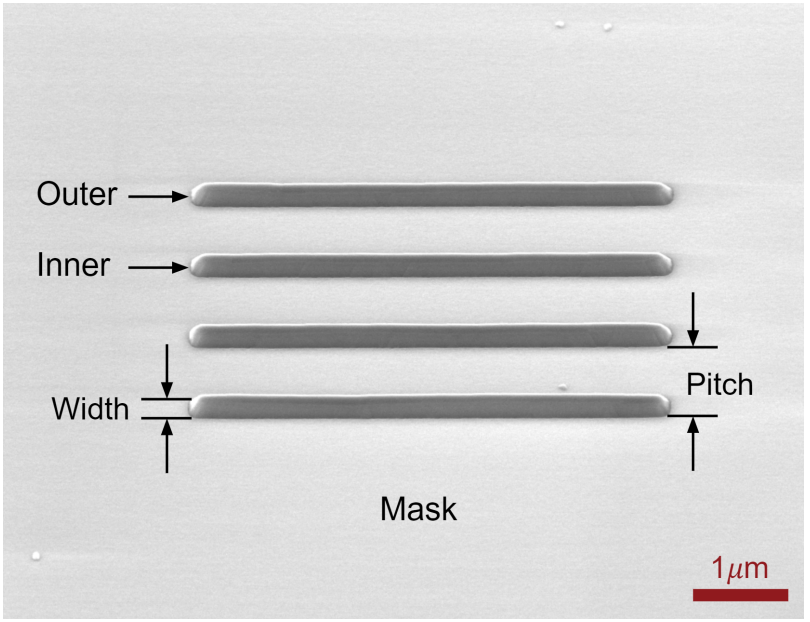

Figure 4.2: **Nanowire 4-array SEM with labels:** Array of four nanowires (oriented horizontally) with labels of width and pitch, as well as inner an outer nanowires. The part shown is surrounded by a much larger mask area with no defined features. Image is included for explanatory purposes and the growth shown is not directly related to the paper, ref. [P1]. *Growth by Daria Beznasyuk, SEM image by Martin Espiñeira Cachaza.*

varying growth rates. This finding highlights the importance of design considerations in SAG and the necessity of precise control over the growth process to achieve the desired outcomes in nanowire fabrication.

The most relevant significant findings from the study, ref. [P1] are captured in figure 4.3. This figure shows the variations in growth rates of nanowires under different conditions, providing valuable insights into the dynamics of Selective Area Growth (SAG). The left panel of the figure shows the growth rate as a function of pitch, with a fixed nanowire width. A notable divergence in growth rates between inner and outer nanowires is observed, with inner nanowires consistently exhibiting higher rates for pitches up to approximately 4μm. This suggests a characteristic diffusion length $L_D = \sqrt{D\tau} \approx 4\mu$m, indicating that beyond this distance, nanowires become effectively isolated. The diffusion length probed here pertains to the amorphous mask. As pitches decrease, the growth rate of inner nanowires nears unity, reflecting the diminishing influence of mask regions and suggesting that very closely spaced nanowire arrays behave similarly to a single large trench.

The right panel presents growth rates as a function of nanowire width, maintaining a fixed pitch. The disparity in growth rates between inner

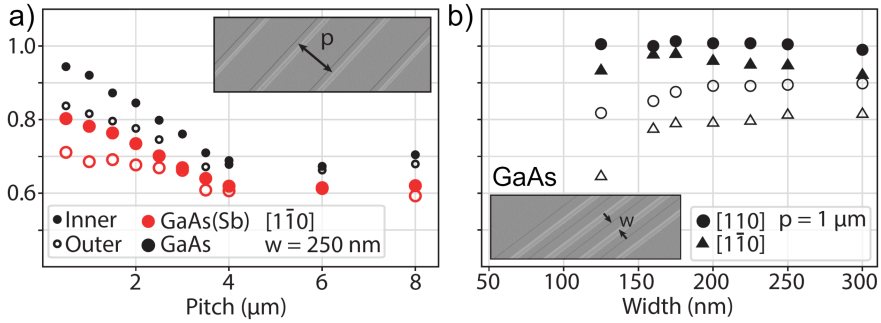

Figure 4.3: **Main SAG growth rate results: a)** Growth rates as a function of pitch at fixed width $w = 250$nm. Notice the clear difference in growth rates between inner (filled markers) and outer (open markers) nanowires. The values converge as the nanowires are distanced sufficiently far apart at $p \approx 4\mu$m. **b)** Growth rates as a function of width at fixed pitch $p = 1\mu$m. Notice the steeply declining growth rate towards lower nanowire widts.
Figure adapted from from ref. [P1], reprinted with permission.

(filled markers) and outer (open markers) nanowires is pronounced, particularly at lower nanowire widths. A noteworthy point is the observation that growth ceases for sufficiently narrow trenches, as indicated by a trench width of 45nm showing no growth compared to substantial growth in a 150nm trench (shown in the original paper, ref. [P1], not shown here).

The study also reveals a lower overall growth rate for GaAs nanowires oriented along the [1$\bar{1}$0] direction compared to the [110] orientation, an outcome that appears counterintuitive given the longer diffusion length in the [1$\bar{1}$0] direction[50, 51]. However, the anisotropic diffusion length on the crystal should play little to no role, as it is much longer than the nanowire widths examined[52, 53]. The discrepancy is instead attributed to the morphology during growth, with [1$\bar{1}$0] oriented nanowires forming dominant 113 facets known for lower incorporation rates. In contrast, [110] oriented nanowires retain their initial (001) top facet. The zincblende crystal structure of GaAs, particularly on a (001) substrate, plays a crucial role in this orientation-specific behavior, leading to different sets of crystallographic orientations for the nanowire side facets, which can be directly read out from a stereographic projection[13]. These results underscore the intricate interplay of various factors in crystal growth, including design, crystal orientation relative to the substrate, and growth morphology. This complexity significantly influences the growth rates, highlighting the importance of considering all these aspects in the design and execution of growth processes for nanowire fabrication.

The study of growth rate phenomena in Selective Area Growth (SAG), particularly around a single exposed trench or mask aperture, is crucial

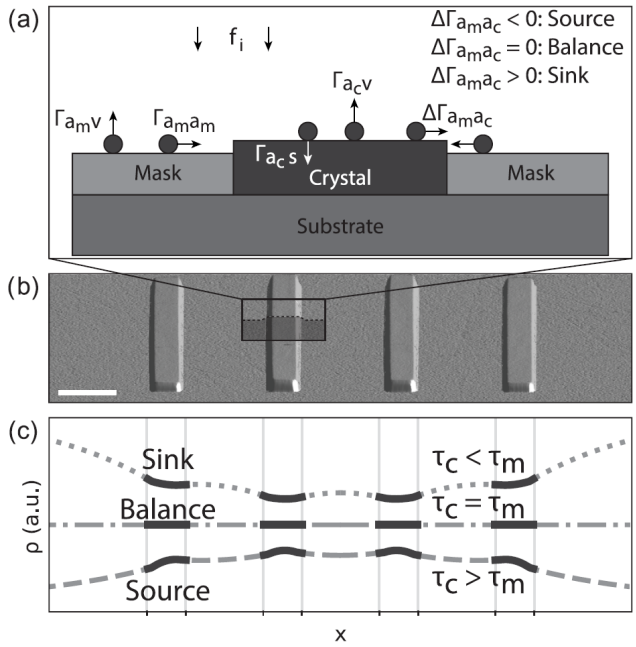

Figure 4.4: **Nanowire array kinetics and regimes: a)** Schematic of substrate with partially covering mask, and aperture exposing substrate and crystal during growth. The Γ-rates correspond to those described in chapter 2, with additional sub-subscripts "m" and "c" denoting mask and crystal regions, respectively. **b)** AFM scan of four parallel GaAs SAG nanowires oriented along the $[1\bar{1}0]$ in-plane direction. Lateral scale bar is 500nm. **c)** Types of solutions to the adatom density equations of the form in equation 4.1 with three different regimes determined by the sign of the net adatom transition rate from mask to crystal $\Gamma_{a_m a_c}$.
Figure adapted from from ref. [P1], reprinted with permission.

for understanding the dynamics of nanowire fabrication. Figure 4.4a illustrates the critical transitions involving adatoms, with subscripts a_m and a_c representing adatoms on the mask and crystal, respectively. This schematic is instrumental in visualizing the key processes that govern material deposition in the exposed regions. Figure 4.4c further elaborates on this by depicting three distinct types of solutions to the steady-state adatom density diffusion equation (Equation 4.1). These solutions mirror the types identified in section 3.2, providing a deeper insight into the diffusion dynamics under steady-state conditions.

$$D\frac{\partial^2 \rho(x)}{\partial x^2} + f - \Gamma_{av}(x) - \Gamma_{as}(x) = 0 \tag{4.1}$$

It is important to recognize that Equation 4.1 is essentially a one-dimensional, steady-state rendition of Equation 2.12, which was discussed

in detail in chapter 2. This equation assumes that decomposition is negligible ($\kappa_{sa} = 0$) and that the transition rates are linearly dependent on the adatom density. Such assumptions simplify the model, allowing for a clearer understanding of the fundamental processes at play in SAG, particularly in terms of how adatoms behave on different surfaces (mask vs. crystal) and how this behavior influences the overall growth rates and patterns.

4.2 Diffusion transition characteristics

The concept of "growth modes"[1] as presented in ref. [P1] refers to the steady-state diffusion characteristics at the boundary between the mask and crystal regions, indicated by the sign of the transition rate $\Delta\Gamma_{a_m a_c}$. The correspondence of these modes with simulation solution types highlights that discrepancies in growth rates are primarily a result of adatom diffusion – a mass transport phenomenon. We underscore that, just as in section 3.2, the steady-state solution is considered an "average" solution, not representative of an actual steady state during growth.

A positive net rate $\Delta\Gamma_{a_m a_c} > 0$ is labeled "sink" behaviour, characterized by each exposed crystal region acting as a sink, attracting material flow. This results in a gradient with decreasing adatom density from the mask region towards the crystal boundary, and then again towards the interior of the crystal region. In this scenario, each trench has an associated collection area from which adatoms are drawn towards the crystal for incorporation. This behavior is reminiscent of early-stage growth rates in Vapor-Liquid-Solid (VLS) nanowire synthesis[14, 21, 54–58], where growth rates show positive scaling with increased distance between catalyst sites due to reduced competition for material. The effect from competition tapers off in VLS as the growth proceeds and the nanowire length increases, since the adatoms become unable to traverse the distance from the substrate along the nanowire axis to the catalyst at the end. Thus, longer VLS nanowires show slower growth rates, as the main contribution of material is either directly impinging on the catalyst droplet or diffusing from the sides of the nanowire. This also renders the collection area on the substrate obsolete[14, 21, 57], and scaling with inter-nanowire distance vanishes.

A negative net rate $\Delta\Gamma_{a_m a_c} < 0$ is labeled "source" behaviour, and involves adatoms flowing from the crystal to the mask regions. Despite this outward flow, steady-state crystal growth is maintained as long as the influx of adatoms onto the crystal surpasses the combined outflow due to diffusion and desorption. This phenomenon explains why the observed growth rates are consistently lower than unity[P1]. This growth mode is the

[1] These modes – sink, source, and balanced – are fundamentally different from the morphological growth modes (Frank-van der Merwe, Volmer-Weber, and Stranski-Krastanov) discussed earlier.

result of the relationship between the two lifetime limiting mechanisms[2] on the crystal and on the mask. When $\tau^c > \tau^m$ the system accumulates adatoms in the crystal regions compared to the mask regions. The gradient and diffusion (see chapter 2.3) caused by this relative accumulation leads to an effective two-step lifetime limiting mechanism for adatoms on the crystal: diffusion onto the mask and subsequent desorption (figure 4.4a).

The "balanced" growth mode $\Delta\Gamma_{a_m a_c} = 0$ is speculated to exist, which implies a uniform flux distribution and adatom lifetime across both crystal and mask regions. For true selectivity, this would necessitate equal lifetimes on crystal and mask surfaces: $1/\tau^c = 1/\tau^m$. The balanced mode would manifest as a growth rate on the crystal equal to the planar growth rate, independent of design parameters.

The solution types presented in figure 4.4c, derived from the 1-dimensional reduction of the SAG problem, offer a valuable understanding of the adatom density distribution. These solutions were obtained using the `bvp5c` boundary value problem solver from MATLAB[59]. Additionally, figure 4.5b showcases a sample solution for the steady-state 2-dimensional adatom density distribution, computed using the Python package `FiPy`. This analysis extends the principles discussed in section 3.2 to a more complex, 2-dimensional scenario. In this setup, regions are categorized as either crystal or mask, exploiting the symmetry in an array of four nanowires. This reduces the computational domain to a quarter of the full pattern, with crystal regions represented by the two exposed areas in the lower left and the mask covering the remaining area. The steady-sstate version of equation 2.12 applies throughout, with distinct parameter sets for crystal and mask regions. Boundary conditions are applied as follows:

- Zero derivative boundary condition: Implemented around all outer edges for symmetry, as per equation 3.4.
- Flux conservation: Enforced across internal boundaries between regions, in line with equation 3.5.
- Outer boundary values: Set according to equation 3.6, reflecting the conditions far from the active region.

The emergence of "sink" or "source" mode solutions hinges on the comparative lifetime-limiting rates on the mask versus the crystal regions. A longer lifetime on the crystal ($\tau^c > \tau^m$) results in "source" behavior, as illustrated in figure 4.5b. Conversely, a longer lifetime on the mask ($\tau^m > \tau^c$) indicates "sink" behavior. The extent of the difference in adatom density between inner and outer nanowires is heavily influenced by the rate values, with significant differences likely due to the exponential factors in the

[2] The lifetime on the crystal: $1/\tau^c = 1/\tau^c_{as} + 1/\tau^c_{av}$ comes as a result of straight forwardly summing transition rates for adatom life terminating mechanisms.

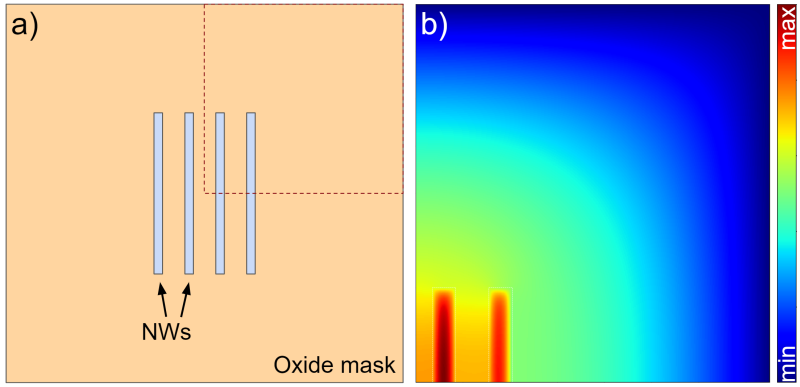

Figure 4.5: **Nanowire 4-array, overview and simulation: a)** Schematic of substrate with amorphous mask (orange) and exposed nanowire trenches (blue). Red dashed frame indicates area for simulation with proper symmetry boundary conditions imposed. The full square shown may be thought of as being the "tile" repeated in a much larger array of tiles, all comprising similar arrays of 4 nanowires. **b)** Sample result from mean-field simulation in `FiPy` showing "source" type behaviour. The lack of values on the color scale is indicative of this being a type of solution, with exact values highly dependent on input parameters. Further explanation in main text.

rates, consistent with the Arrhenius form discussed in section 2.2.

This study underscores the dependency of growth rates on both the design pattern and thermodynamic growth parameters. It highlights the necessity for further theoretical and experimental work to deepen our understanding of SAG kinetics, particularly regarding the control of crystal growth rates and accounting for proximity effects between design elements. Additionally, ref. [P1] provides insights into the complexity of binary and ternary growth in systems like $In_xGa_{1-x}As$ nanowires, demonstrating significant shifts in growth regimes and the interplay between composition and morphology. This complexity adds another layer to the challenges of achieving precise control in SAG, especially when dealing with multiple species that may exhibit different behaviors within a selected growth window. Similar studies would be highly relevant for designs synthesized with a stencil based technique.

5

Thin film critical height review

Parts of this chapter and subsections were initially drafted to be included as a short review section of the paper *"Collective formation of misfit dislocations at the critical thickness for equilibrium nanowire heterostructures"*, ref. [P2], co-authored with T. C. Thann et al. The bulk of this review ended up not making the final cut of the paper, but parts of it were included in my co-authors Master's thesis, ref. [60].

Some parts of the following chapter therefore appear in one form or another in the two sources mentioned.

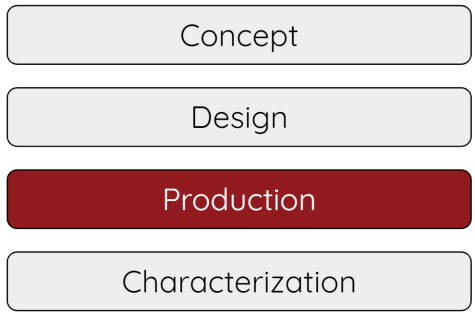

Figure 5.1: **Synthesis production stage:** This stage relates to the actual realization of the design, the physical production or synthesis of the circuit.

The critical height refers to the introduction of misfit dislocations, that is, a phenomenon occurring during growth. As such, it pertains to the production stage. However, concluding the presence of misfit dislocations can occur in-situ during crystal growth – or with other characterization techniques ex-situ, in a subsequent characterization step.

5.1 Case study: InAs on GaAs

Crystal growth, particularly in the context of heteroepitaxial processes where one material grows on top of another, involves a multitude of complex phenomena. A notable example is the self-assembly of InAs quantum dots on a GaAs substrate under specific conditions[47, 61–64], a phenomenon utilized e.g. in the optical qubit platform. The upcoming chapter reviews experimental observations of growth effects in such heterostructures, leading to a discussion on the critical height for InAs grown on GaAs. This sets the stage for a subsequent chapter that examines strain relaxation phenomena in specific InGaAs heterostructures. These strain-related effects amount to an additional layer of complications which need to be accounted for, in the case of crystal growth where we are concerned with strain and perturbations related to crystal defects.

When InAs is grown on GaAs(001), there are three significant transition phenomena often reported in literature, with some works reporting on all three while others report on just one or two:

- The *transition height*, h_t, at which islands are introduced, and the initial Frank-Van der Merwe (FM) layer-by-layer growth mode transitions to either Volmer-Weber (VW) displaying pure island growth or Stranski-Krastanov (SK) with both a wetting layer and islands.
- The *critical height*, h_c, at which the first misfit dislocations are introduced.

- A *reversion height*, h_r, beyond which the growth mode appears to revert back to Frank-Van der Merwe.

In an equilibrium framework, the preferred growth mode is determined by the configuration with the lowest free energy. To model this, equation 5.1 represents the free energy in a format similar to those employed in other studies focused on phenomenological models for growth modes[65–67]. This approach allows for the assessment of how various factors, such as strain, surface energies, and misfit dislocations, influence the overall growth dynamics. Understanding these transitions and their underlying mechanisms is crucial for optimizing the growth of heteroepitaxial structures. This knowledge not only aids in the controlled fabrication of devices like quantum dots but also helps in addressing challenges related to strain and defect formation, which are critical for ensuring the quality and performance of the resulting semiconductor materials and devices.

$$E_{\text{free}} = \gamma(1+\beta) + \frac{1}{2}M(1-\alpha)\epsilon^2 h \tag{5.1}$$

Equation 5.1 captures the interplay between various energy contributions that influence the formation of islands on the growing crystal layer. This equation considers:

- γ: The total surface energy in the absence of islands, comprising the surface energies of the substrate-crystal interface γ_{sc} and the crystal-vacuum boundary γ_{cv}.
- M: The effective stiffness of the growing layer.
- ϵ: The mismatch strain between the substrate and the growing crystal layer.
- h: The height of the growing crystal layer.
- $-\alpha$: The decrease in strain energy due to island formation.
- β: The increase in surface energy resulting from island formation.

In the absence of islands ($\alpha = \beta = 0$), the equation simplifies to account for only the surface and strain energies of a uniform 2-dimensional layer. The preference for island growth occurs when the reduction in strain energy $-\alpha$ outweighs the increase in surface energy β.

Drawing an analogy with Young's equation for the contact angle of a liquid droplet on a surface[68], we can conceptualize the substrate as the rigid surface and the growing crystal as the "droplet." However, unlike a liquid droplet, the atomic structure of the growing crystal interacts with the substrate, leading to strain and anisotropic surface energy density: the crystal morphology will be faceted. Here, wetting (small contact angle) points towards layer growth (Frank-van der Merwe mode), and de-wetting

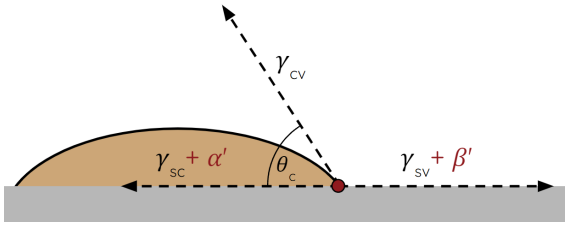

Figure 5.2: **Young's equation for crystal "droplet":** Subscripts s, c and v denote substrate, crystal and vacuum, respectively. The forces in Young's derivation are proportional to the local surface energy densities, and in our case these are supplemented by the additional terms α' and β'. α' and β' denote the works associated with a change in the unitless quantities α and β from equation 5.1, respectively. A higher value for α' promotes island formation, as island formation helps lower the strain energy. Conversely, a higher value for β' hinders island growth due to an increased surface energy cost. Further explanation is found in the main text.

towards island growth (Volmer-Weber mode). The balance of forces is modified by strain due to lattice mismatch: a high α value favors island formation, while a high β value favors wetting.

Stranski-Krastanov (SK) growth, which involves an initial layer growth followed by island formation, challenges the equilibrium crystal shape (ECS) concept and cannot be fully explained by surface energy considerations alone, as it violates the convex nature of such. This growth mode arises from a complex interaction between surface and strain energies. Studies comparing growth modes in different semiconductor systems reveal that the appearance of SK growth cannot be attributed solely to strain either, as systems with both lower and higher mismatches exhibit varied growth behaviors[67].

We shall expand upon equation 5.1 later in section 5.2, when we review the phenomenological models for misfit dislocations. In summary, island formation in heteroepitaxial growth serves as a form of strain relaxation, and SK growth emerges as a hybrid phenomenon driven by both surface and strain energy conditions. Further exploration of these concepts, including a review of phenomenological models, will be undertaken in later sections, shedding light on the complexities of heteroepitaxial crystal growth and the factors that govern the different growth modes.

5.2 Phenomenological models for planar films

The equilibrium models developed by Okajima et al. (2000)[65], Shiraishi et al. (2002)[66], and Tinjod et al. (2004)[67] provide significant insights into the interplay between morphology and strain in determining growth modes. These models utilize phenomenological expressions to represent

the free energy of various system configurations, considering scenarios with and without the presence of islands and misfit dislocations (MDs). The general form of these expressions, as seen in equation 5.2, is:

$$E_{\text{free}} = \gamma(1+\beta) + \frac{1}{2}M(1-\alpha)\left(1-\frac{l_0}{l}\right)^2 \epsilon_0^2 h + \frac{E_d}{l} \tag{5.2}$$

In equation 5.2 (compare to equation 5.1 above), ϵ_0 the average strain in the absence of islands and misfit dislocations. The parenthesis $(1-l_0/l)$ accounts for the density of misfit dislocations with l_0 being the characteristic distance between dislocations for full plastic relaxation and l being the actual distance. Finally, E_d/l is the energy cost associated with the misfit dislocations itself, with one misfit dislocation per length l.

Figure 5.3 shows two scenarios for the evolution of these energies for two different values of E_d, the misfit dislocation energy density.

The critiques of the phenomenological models by Okajima et al. (2000)[65], Shiraishi et al. (2002)[66], and Tinjod et al. (2004)[67] highlight some limitations in their approach to explaining growth modes in heteroepitaxial systems. While these models provide valuable insights, certain aspects warrant closer examination. We note that equation 5.2 includes a strain energy linear in layer height in the presence of misfit dislocations. This is effectively a mean field strain which might be a good approximation far from the interface, but it proves problematic in the case of misfit dislocations in a thin film. Taking as an example the case of $l = l_0$, the strain energy of the growing layer fully vanishes in equation 5.2, which obviously neglects the highly-strained field near each misfit dislocation. For highly mismatched and very thin films, most of the growing layer is indeed close to the interface upon formation of misfit dislocations. The expressions are also somewhat one-dimensional, as no interplay is considered between misfit dislocations along different directions. One could argue that each of these concerns can be absorbed by an adjustment to the phenomenological parameters, however this would in turn also make the phenomenological nature of the expression more problematic. Nevertheless, the papers[65–67] demonstrate that systems with free energies described by such expressions can have equilibrium configurations which initially favor 2-dimensional coherent growth, followed by S-K growth with coherent islands, then followed by S-K growth including misfit dislocations and finally 2-dimensional growth with misfit dislocations. This phenomenologically matches the observations presented in section 2.2. Depending on the closer details of the phenomenological parameters, one or more of these modes may be suppressed in the growth. The authors even supply estimates for the free parameters in the phenomenological model, but since some of these are complicated in nature (e.g. α, the fractional decrease in strain energy in the growth layer caused by formation of islands in S-K growth), they are not easy to relate directly to growth parameters. As such these works serve a more explanatory purpose.

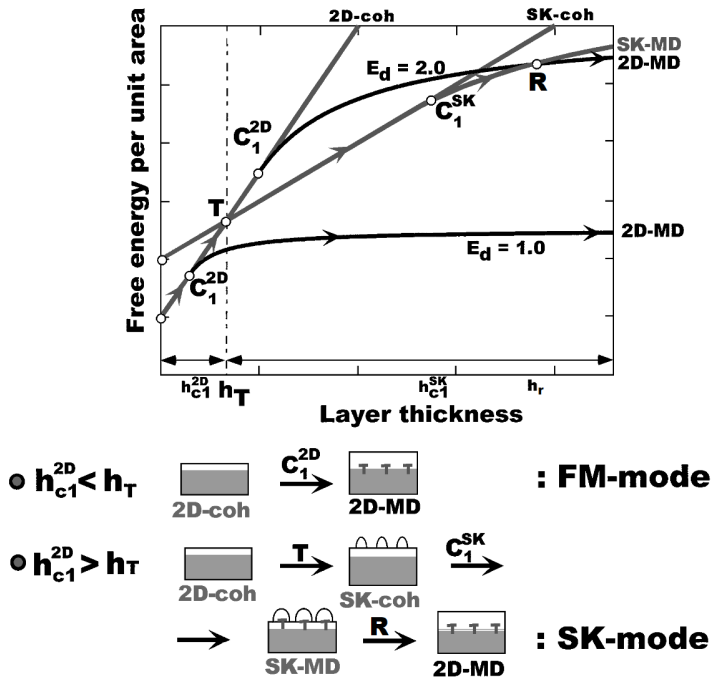

Figure 5.3: **Evolution of growth modes:** The main panel shows the normalized free energy for different growth modes as a function of film thickness h. Paths traced with arrows show the lowest energy configurations in the case of two different values for the misfit dislocation energy E_d. Points marked with "C" are critical, i.e. when the configuration with misfits becomes favorable compared to the corresponding coherent case. Lower panel shows the two main paths with the observation, that the growth stays 2-dimensional in the case where misfits are introduced before islands. R is reversion with h_r corresponding to the reversion height.
Figure from ref. [65], reprinted here with minor changes with permission in accordance with license 1422968-1.

Another approach, the "generalised Wulff-Kaichew theorem" by Müller and Kern (2000)[69], directly addresses the change in free energy during crystal growth on a mismatched substrate. This approach also approximates the strain in the presence of dislocations as mean-field but includes substrate strain in the consideration. The "relaxation factor", R in this model serves a similar function to α in the earlier models, explaining trends but not providing predictions for transitions like the onset of 3D islands or misfit dislocations, as predictions of transitions will depend on other unknown factors, e.g. the crystal surface energy density, $\gamma(\mathbf{n})$, as a function of surface normal direction (section 2.4). Müller and Kern's work does suggest that the introduction of each dislocation should abruptly

change the equilibrium shape of a 3D island, a phenomenon potentially observable through in-situ imaging. This insight could explain observed rapid changes in island diameter after the onset of island growth, possibly linked to equilibrium shape alterations due to misfit dislocations.

5.3 Theoretical predictions for planar films

A general concern for the theoretical models in the field must be addressed here, even if no direct resolution is readily available; most theoretical predictions employ scenarios for misfit dislocations in a planar film of a certain thickness, h. But the experimental observations summarized above show that the introduction of misfit dislocations, at least in our case, is closely tied to island formation. The differences could be highly significant, and we would expect theoretical predictions to overestimate the critical height, since the actual physical system has island formation with misfit dislocations as an additional degree of freedom for minimization of the free energy. From an equilibrium point of view, this configuration must be favorable over the planar growth with misfit dislocations, since it shows up in experiments. This is intertwined with another concern, that most of the models which we are about to review either implicitly or explicitly assume for the strains to be very small, which is not true for the cases relevant to us here. As a result, we see phenomena such as island formation which is not accounted for in the models below. This is not as much a flaw of the theories as it is just an assumption, nevertheless it turns out to be important in our case.

Wu and Jin (2015)[70] express a reasonable concern from the variety of observations and theoretical models: most authors of predictions seem to be able to find experimental observations that fit their model and vice versa for the experimentalists attempting to explain their findings from theory. The reader should be mindful, that each model may in fact only show dependencies approximately reasonable in a narrow part of the wider range of available growth variables. Here we present models in two broad categories, and the reader interested in settling the score between different models is encouraged to consult the excellent reviews by other authors[70, 71].

The early theoretical work on predicting the critical height for misfit dislocations in heteroepitaxial growth, notably by Frank and van der Merwe in 1949[72], provided a foundational approach to understanding these phenomena. Their model conceptualized the epilayer as a one-dimensional spring chain of atoms, influenced by the periodic potential from the atomic configuration of the substrate. This representation allowed for the construction of a potential energy equation for the epilayer, leading to the estimation of a characteristic distance, l_0 between misfit dislocations. This distance is a function of several factors including the spring constant between atoms, the amplitude of the periodic potential, and the

substrate lattice spacing. The critical condition for the introduction of misfit dislocations in their model is expressed through the ratio between l_0 and P_0, with the latter being the inverse of the mismatch between the atomic distances in the chain and the substrate's periodic potential. In terms of crystal heterostructures, this translates to the necessary period of regular misfit dislocations for achieving full plastic relaxation. A notable conclusion from their work is the prediction of a critical mismatch limit of approximately 7%. This implies that only configurations with a mismatch below this threshold are likely to develop a coherent epilayer exceeding one monolayer in height before the onset of misfit dislocations. However, the reliance on inter-atomic forces in this model makes the direct calculation of critical height complex. Later studies have aimed to address this by offering more straightforward approaches, but the initial insights provided by Frank and van der Merwe have been significant.

Van der Merwe's work in 1963[73, 74] significantly contributed to the theoretical understanding of misfit dislocation formation in heteroepitaxial layers. His approach involved comparing the interfacial strain energy density for configurations both with and without misfit dislocations, employing two distinct models for calculating interfacial forces: the parabolic and Peierls-Nabarro models. For a critical mismatch of approximately 7%, he deduced that the critical height for misfit dislocations falls between one and two lattice parameters, or about 2-4 monolayers (ML). The parabolic model leaned towards the higher end of this range, while the Peierls-Nabarro model suggested a slightly lower critical height. His calculations also showed that differences in the relative hardness of the epilayer and substrate have minimal impact on the critical height, particularly relevant to systems like InAs grown on GaAs.

Matthews' equilibrium model, introduced in 1966[75] and further developed in the following years[76], marked a shift in focus from energies to forces. The model starts with pre-existing threading dislocations, which under sufficient misfit stress can produce misfit dislocations along the interface. Matthews and Blakeslee observed a much lower density of misfit dislocations than predicted, suggesting potential barriers to dislocation formation that keep the system out of equilibrium. When applied to InAs grown on GaAs, the model predicts a critical height of between $h_c = 5$ and 5.4 ML[77, 78], with variations stemming from different interpretations and expansions of the model[71]. The Matthews model has been subject to a wide range of interpretations, leading to significant variability in critical height predictions for the same system. As Fitzgerald noted in 1991[79], these predictions can differ by an order of magnitude. This variability, coupled with the discrepancy between theoretical predictions and experimental observations, highlights the complexities involved in understanding heteroepitaxial growth processes. Consequently, when experimental results are said to align with the Matthews model, such statements should be interpreted with an understanding of the model's broad scope and inherent limitations.

People and Bean introduced a model in 1985[80] that shared similarities with van der Merwe's approach, focusing on comparing strain energy densities of different system configurations. They examined both a coherent system and one where a screw dislocation forms at the interface at a specific film thickness. In their analysis, People and Bean also compared their model to other existing models, including those by van der Merwe[73, 74], Matthews[75] and Blakeslee[76], as well as experimental data from the growth of Ge_xSi_{1-x} on Si. They found that their revised model aligned more closely with the experimental evidence, offering a more compatible explanation for the observed phenomena.

Dodson and Tsao in 1987[81] proposed a novel approach that considered time-dependent relaxation based on dislocation velocities. This model aimed to predict the evolution of strain relaxation over time, differing from previous models that focused on the static relationship of strain relaxation to the height of the growth layer h. However, the work of Whaley and Cohen[82, 83] challenged the validity of Dodson and Tsao's approach. Their results indicated that the evolution of strain relaxation was dependent on the layer height h rather than time t, demonstrated by halting growth and continuously monitoring strain relaxation.

For a comprehensive understanding of the various theoretical models addressing strain relaxation in semiconductors, Dunstan's in-depth review in 1997[71] is highly recommended. This review not only covers the original works but also includes derived works that show equivalences between models under different conditions and assumptions. While the introduction provided here highlights the key aspects, Dunstan's review offers a more detailed and nuanced examination of the topic, beneficial for readers seeking a deeper understanding of these complex theoretical models.

Marée et al. in 1987[84] conducted a study comparing various theoretical models for misfit dislocations with experimental data from the growth of $In_{0.07}Ga_{0.93}As$ on GaAs, which has a mismatch of $\delta \approx 0.5\%$. A key observation in their work was the low density of pre-existing dislocations, which is significant for the Matthews model that posits the transformation of pre-existing threading dislocations into misfit dislocations under stress. This low density implies that new misfit dislocations would need to nucleate through half-loop generation, a process with a higher barrier for nucleation. Consequently, a Matthews-based model would likely underestimate the critical height for misfit dislocation formation. This aligns with Matthews and Blakeslee's own findings, where the observed density of misfit dislocations was much lower than their model predicted[76]. Marée et al. also noted that most theoretical models are limited in their applicability. For very low mismatches ($0.2\% < \delta < 2\%$), limited dislocation mobility constrains the models, while for higher mismatches ($\delta > 2\%$), the interaction of dislocations and other strain relaxation mechanisms, such as island formation, become significant factors. The $In_{0.07}Ga_{0.93}As$ system falls conveniently within these limits. In this context, their model

based on the generation of dislocation half-loops was found to best fit the experimental data, providing a more accurate prediction of the critical height for misfit dislocation formation in such heteroepitaxial systems.

5.4 Experimental observations for planar films

In the upcoming section, we provide an introductory overview of experimental observations concerning strain relaxation and growth modes for planar films of InAs on GaAs(001), as documented in the literature. It is important to recognize that there are various, sometimes conflicting, experimental findings in this area, a point also noted by other researchers[70, 85]. The discrepancies and varying interpretations of these results can be attributed, at least in part, to differences in key experimental factors:

- **Growth conditions:** The growth of III-V semiconductors such as InAs and GaAs involves a diverse range of time-dependent conditions. These include thermodynamic variables like temperature and partial pressures, as well as procedural aspects like shutter operation, temperature variation rates, and sample rotation during growth. Additionally, substrate preparation, encompassing various cleaning procedures and differences in substrate miscut, significantly influences the initial growth conditions. This wide array of parameters complicates direct comparisons between different studies. For detailed insights into specific results, consulting the original works is recommended.

- **Characterization techniques:** The methodologies used for characterizing grown films also contribute to the diversity in findings. As characterization technologies have evolved, they have brought forth different aspects of the samples being studied. Consequently, different characterization techniques may lead to varying conclusions about critical heights or interpretations of changes in growth modes, as seen e.g. in reflection high-energy electron diffraction (RHEED) patterns.
  A notable issue in this context is what we can term *strain-composition ambiguity*. This arises in studies lacking direct elemental analysis such as electron energy loss spectroscopy (EELS), where changes in lattice parameters observed through techniques such as RHEED could be attributed to either elastic strain or material composition changes. This ambiguity is particularly pertinent since studies have shown discrepancies between the material composition in the grown crystal and the input ratio from effusion cells[86–89]. Furthermore, the phenomenon of *intermixing*, which tends to increase with temperature[89], adds another layer of complexity, especially in the growth of ternary compounds like $In_xGa_{1-x}As$, where composition is a variable parameter.

The factors highlighted here underscore the challenges and complexities in reviewing and drawing consistent conclusions from the wide range of studies in this field. It is often challenging to isolate the effects of single variables, as multiple parameters tend to change from one experiment to another. In the following review, we aim to present the experimental observations on an equal footing, but readers should be aware of the potential variations and nuances inherent in different experimental setups.

As flux dependence

Schaffer et al. (1983)[90] conducted a study on the nucleation and early growth stages of InAs on GaAs(001) under In-stabilized conditions at temperatures ranging from 510-520°C. Their key morphological observations shed light on the growth behavior of this heteroepitaxial system. The study revealed that the InAs film initially grows two-dimensionally up to a thickness of about 7Å (approximately 2.3 monolayers, ML). However, at the next measured point of 9Å (around 3 ML), the reflection high-energy electron diffraction (RHEED) patterns indicated a significant change, displaying two distinct patterns superimposed on each other. The authors interpreted this as a transition from two-dimensional growth to island growth, with InAs forming islands interspersed with areas of exposed indium-stabilized GaAs substrate. The exact growth mode (Volmer-Weber or Stranski-Krastanov) at this stage was not definitively determined, but the presence of islands was evident. The lattice constant of these islands was measured at 5.95Å. This island growth pattern persisted for film thicknesses ranging from 9Å to 44Å (up to about 15 ML). Beyond this point, the RHEED pattern corresponding to the lower lattice parameter vanished, presumably due to the coalescence of the islands covering the entire GaAs substrate. As the growth continued, the lattice parameter of the film gradually increased, eventually reaching a saturation value of 6.07Å at a thickness of 1900Å, indicative of pure, unstrained InAs. The authors asserted that the heterointerface should be atomically abrupt without any alloying at the interface, implying that the film would be composed of pure InAs from the interface upward. According to this interpretation, any changes in the lattice parameter observed through RHEED would reflect strain relaxation rather than compositional variations. However, other studies, such as those by Joyce et al.[86], challenge this view, suggesting significant alloying at higher temperatures, particularly above 500°C. This contrast in findings exemplifies the strain-composition ambiguity mentioned above, highlighting the challenges in distinguishing between effects due to strain relaxation and compositional changes in such heteroepitaxial systems.

Tournié, Trampert, and Ploog (1994, 1995)[91, 92], explored the growth of InAs on GaAs(001) under different arsenic flux conditions, providing insights that align with previous observations. The studies focused on samples grown under high and low As flux regimes, both at a growth rate

of 0.4 ML/s at 430°C, and without capping. In the high As flux sample (As_4/In flux ratio 10), a transition to 3D island formation was observed at a height of 1.5 ML, as indicated by changes in the RHEED pattern. Misfit dislocations were detected at a layer height greater than 8 ML through high-resolution TEM. These dislocations were found in a band approximately 1nm wide around the interface, consisting of both 60 ° and pure edge types, spaced about 4nm apart. RHEED measurements suggested rapid strain relaxation, with the film lattice parameter approaching the bulk value of InAs after only 7 ML, though it was not possible to differentiate whether this relaxation was due to island formation or dislocation generation. In contrast, the low As flux sample (As_4/In flux ratio 0.7) exhibited a markedly different growth behavior. The growth remained planar up to a layer height of 4.8 ML, with the formation of misfit dislocations occurring without prior island formation. TEM characterized these dislocations as pure edge types located at the interface, with an average spacing of 8nm. RHEED analysis indicated a residual strain of about 2% at 35 ML, assuming a composition of pure InAs. Despite the lower As pressure, the amount of material deposited closely matched the nominal flux, indicating that growth was not significantly impeded. The authors suggested that these differences might indicate a kinetic limitation in the formation of misfit dislocations. However, without direct compositional analysis, such as EELS, the strain-composition ambiguity comes into play. For instance, if the lower As pressure led to significant alloying in the growing film, the lower lattice parameter observed by RHEED could indicate a composition of $In_{0.68}Ga_{0.32}As$, assuming Vegard's law. This composition would correspond to a mismatch of about 4.9%, compared to 7.2% for pure InAs on GaAs, and would imply a spacing between misfit dislocations close to the observed 8 nm. This example highlights the challenges in conclusively interpreting experimental data due to the interplay of strain and composition in heteroepitaxial growth with characterization techniques based on lattice parameter.

In the realm of heteroepitaxial growth, the role of surfactants presents an intriguing dimension, as evidenced by studies on InAs growth on GaAs(001). Though this thesis does not delve deeply into surfactants, a few notable observations are relevant. For instance, Grandjean et al. (1992)[77], observed that introducing a tellurium surfactant during InAs growth at 400°C could shift the transition height from 1.5 ML to 6 ML. They attributed this change to the surfactant affecting the surface energies.

Conversely, Snyder and Orr (1993)[93], proposed a different perspective. They argued that the surfactant influence on the growth mode stemmed from kinetic effects rather than energetic considerations. While the results from Te-surfactant assisted growths bear resemblance to those under lower As pressure, it is crucial to recognize that different mechanisms might be driving these apparently similar outcomes. This notion aligns with the suggestion from other authors[70], that the complexities of

Stranski-Krastanov (S-K) growth cannot be fully encapsulated in a simplistic equilibrium framework.

Additional research supports the idea of rapid mass transport during the transition from two-dimensional to three-dimensional growth, with studies indicating significant mass transfer from the wetting layer and underlying substrate[94–96]. Joyce et al. (1998)[86], found that the volume of islands increased more rapidly than the rate of material supplied for growth, implying a significant contribution from the wetting layer. These findings emphasize the need for careful interpretation of experimental results and caution against over-reliance on initial conclusions. While the specific mechanisms driving the transition to S-K growth are fascinating, a thorough exploration of these processes is beyond the scope of this current discussion. For those interested in a more in-depth examination, other works provide comprehensive studies on the topic[70, 85].

InAs/GaAs transitions

Returning to the direct observations of transitions, Houzay et al. (1987)[97] and Glas et al. (1987)[98] conducted detailed studies on the growth of InAs films on GaAs(001), offering significant insights into the transition dynamics of heteroepitaxial growth. The research involved growing InAs films at various thicknesses (1, 2, 7, 15, and 100 monolayers or ML) under As-stabilized conditions at a rate of 0.05 ML/s and a temperature of 420°C. At a film thickness of 1 ML, the RHEED patterns indicated a two-dimensional film structure. However, as the film thickness increased to 2 ML, there was clear evidence of island formation. These islands were remarkably uniform in size, exhibited no measurable strain, and did not show any signs of misfit dislocations. This observation suggests that the transition height from two-dimensional to island growth occurs between 1 ML and 2 ML. When the film thickness reached 7 ML, the islands no longer maintained uniformity in size. Moiré patterns in this stage revealed the presence of misfit dislocations in larger islands (exceeding 200Å in width), while smaller islands remained coherent. This finding implies that the critical height for the formation of misfit dislocations lies between 2 ML and 7 ML. Scanning transmission electron microscopy (STEM) annular dark field images further showed that misfit dislocations tended to nucleate more at the edges of the islands than at the centers. The dislocation density was generally found to increase with the size of the island. For the 15 ML thick film, the observations were similar to those of the 7 ML film, with an increased density of islands. At the 100 ML thickness, the substrate was almost entirely covered by the InAs film, although with a very non-uniform thickness. Moiré patterns from this stage indicated a locally distorted and discontinuous network of misfit dislocations.

Mazuelas et al. (1993)[99] conducted a study to determine the critical thickness for InAs films grown on GaAs(001), using a combination of RHEED and X-ray diffraction (XRD). Their samples were grown under

identical conditions at 350°C for varying durations, with RHEED monitoring during growth and XRD characterization performed post-growth on samples capped with 200nm of GaAs. They found the critical height deduced from XRD to be more reliable, due to a higher density of data points, concluding a critical height of 2.3 ML. It's important to note that this observation via XRD is indirect, capturing overall lattice relaxation rather than specific onset of misfit dislocations, which would be difficult to detect through this method. The study assumes that the subsequent GaAs capping does not significantly alter the configuration of the InAs film.

In another study, Leonard et al. (1994)[100] reported a transition height of approximately 1.5 ML based on atomic force microscopy (AFM) studies of InAs growth at 530°C. They concluded that the initial islands formed were dislocation-free, aligning with earlier studies by Guha et al.[101–103] and Snyder et al.[104]. This conclusion about initially coherent islands was also echoed in the works of Tournié, Trampert, and Ploog[91, 92] and Houzay et al.[97] mentioned above. Leonard et al. noted that dislocated islands tend to form when growth is continued beyond 2 ML, although a more precise value for this transition was not specified. Interestingly, they observed that the average diameter of the islands decreased with increasing InAs deposition within a certain range, going from about 30Å at 1.6 ML to around 20Å at 1.9 ML, suggesting a reconfiguration of the morphology or possibly a transient, kinetically limited phenomenon.

Sasaki (1996)[78] conducted a study on the growth of InAs on GaAs(001) at high V/III-ratios of 40 and 28 at a temperature of 480°C, with a subsequent capping layer of GaAs measuring 100Å. Sasaki observed changes in the reflection high-energy electron diffraction (RHEED) patterns during growth, indicating morphological shifts in the film. The study reports a transition height $h_t \leq 2$ ML and reversion height $h_r = 10$ ML. The critical thickness $h_c = 3$ ML was calculated using a Valence Force Field model and supported by the emergence of Moiré patterns in transmission electron microscopy (TEM) images of islands between 2 and 4 MLs. It is important to note that the actual observation suggested a critical height $h_c \leq 4$ ML, with the value of 3 ML being more a calculation than a direct observation.

InGaAs/GaAs observations

The complexity increases further when considering ternary compounds like $In_xGa_{1-x}As$, where the composition x is a variable parameter. The strain and critical height in the growing layer are heavily influenced by the composition of the crystal, making the strain-composition ambiguity even more pertinent. Studies have shown a discrepancy between the In/Ga ratio supplied from the effusion cells and the ratio actually incorporated into the crystal, as measured by techniques such as EELS. The incorporated $In_xGa_{1-x}As$ composition has been found to be temperature-dependent[89], with higher growth temperatures leading to a lower indium

content x for a constant supply ratio. Often, the composition is assumed to be uniform, but significant intermixing near heterointerfaces is expected[86–89], and the composition may vary with the distance from the interface and locally due to island formation. The reader is advised to keep these intricacies in mind in the following.

Lewis et al. (1984)[105] were among the first to study RHEED oscillations in the growth of InGaAs on GaAs(001), covering both metal and As stabilized conditions at temperatures ranging from 470°C to 530°C. Their study also included different initiation methods for InGaAs growth, such as simultaneous or sequential opening of indium and gallium shutters. While the primary focus was on the RHEED oscillatory behavior, they observed key trends. Notably, the transition height, h_t, decreased with increasing indium content and arsenic pressure. Additionally, initiating growth on a rougher surface (indium shutter opened during rough-phase GaAs growth) led to a lower transition height, suggesting that layer-by-layer growth is more readily achieved from a smooth surface.

Whaley and Cohen (1988, 1990)[82, 83], examined the relaxation of $In_xGa_{1-x}As$ films on GaAs(001) with a focus on how composition and temperature influence the process. Conducted under arsenic-rich conditions, these studies spanned temperatures between 450°C and 510°C, with notable differences in growth rates: approximately 3 ML/s in the earlier study and 0.1-0.5 ML/s in the latter. The main method of characterization in both studies was RHEED. The most significant finding from these studies was the clear trend of earlier and more rapid onset of lattice relaxation at higher temperatures or higher indium fractions, x. Conversely, lower temperatures or lower indium fractions resulted in a delayed onset of relaxation. In all cases, the films initially conformed to the lattice parameter of the underlying GaAs substrate, with relaxation observed through changes in the RHEED pattern during growth. Interestingly, Whaley and Cohen did not directly investigate differences between the transition height h_t, and the critical height h_c. They observed that films grown at lower temperatures were metastable, meaning that three-dimensional features could be induced by merely increasing the temperature. This suggests that island growth can result from the redistribution of already-deposited material, not just as a part of ongoing growth. Moreover, the studies found that the lattice parameter of a two-dimensional film becomes constant once growth is interrupted, as indicated by RHEED measurements. This implies that the lattice parameter of a grown layer is somewhat "locked-in" at a constant temperature, and that additional relaxation occurs only in subsequently grown layers or when the metastable condition is disrupted by a temperature increase.

Nakao and Yao (1989)[106] investigated the growth of $In_xGa_{1-x}As$ on GaAs(001) under As-rich conditions, achieving a growth rate of approximately 0.3 monolayers per second (ML/s). Utilizing reflection high-energy electron diffraction (RHEED) for their analysis, they estimated critical heights for various indium contents: $h_c = [1.5, 2.0, 2.3, 12]$ ML for $x =$

[1, 0.78, 0.66, 0.23] (corresponding to mismatches of [7.16%, 5.58%, 4.73%, 1.65%], respectively). Both the critical heights and compositions were deduced from RHEED oscillations, subject to the common strain-composition ambiguity. The study concluded that pseudomorphic growth starts just before the critical height, and that the reversion to two-dimensional growth occurs due to the coalescence of islands.

Elman et al. (1989)[107] focused on both planar films and quantum wells to examine the critical thickness of $In_xGa_{1-x}As$ on GaAs(001) for $x \leq 0.5$. Conducted at temperatures between 550°C and 615°C and a V/III ratio of 25, the growth rate was roughly 0.5 ML/s. A combination of RHEED and photoluminescence was used for characterization. RHEED oscillations indicated when growth transitioned to a three-dimensional mode. Elman et al. measured the transition height, h_t, from RHEED and speculated that it coincides with the critical height, h_c, where misfit dislocations are introduced, as inferred from broadening in the photoluminescence spectrum. The study revealed that temperatures above 550°C produced similar results, with transition heights of $h_t = [4, 5, 7, 9, 12, 40]$ ML for indium fractions $x = [0.5, 0.42, 0.39, 0.32, 0.29, 0.24]$. Notably, significant differences were observed when comparing thin films to quantum wells, as has also been noted elsewhere[71]. In a subsequent study in 1991, Elman et al.[108] examined quantum wells of $In_xGa_{1-x}As$ for lower indium fractions (x in the range of 0.3 to 0.5) at 410°C and 460°C. The wells were separated by approximately 50nm GaAs barriers, with the possibility of interaction between wells. Using photoluminescence and TEM for characterization, they found that the critical thickness could increase up to sevenfold at lower temperatures for specific indium fractions $x \in [0.3, 0.4]$, suggesting a thermal barrier to the onset of misfit dislocations. This observation points to a potential strategy for manipulating the critical thickness by adjusting the growth temperature.

Guha et al. (1990)[101, 102] explored the growth of thin films of $In_xGa_{1-x}As$ on GaAs(001) with thicknesses ranging from 4 to 11 ML, grown at rates of 0.25 to 0.28 ML/s under varying V/III ratios. Their TEM analysis revealed substrate deformation beneath the islands and strain fields extending up to approximately 150Å into the substrate. Islands were coherent up to around 80Å in height and 250Å in width, with lattice spacing measurements indicating initial in-plane constraint to the GaAs substrate lattice parameter, gradually relaxing with distance from the interface. Incoherent islands displayed misfit dislocations forming at island edges, attributed to high interfacial stress. Defect formation was also noted at island coalescence. Two samples of $In_{0.5}Ga_{0.5}As$ grown for 11 ML at different temperatures (420°C and 470°C) showed temperature-dependent island formation, with the higher temperature sample exhibiting both islands and defects, while the lower temperature sample maintained a smooth surface. The impact on defect structure is inconclusive.

Yao et al. (1990)[109] grew $In_xGa_{1-x}As$ quantum wells on GaAs in sequence, with 20nm GaAs barriers between each well. Conducted at

530°C to 550°C and a rate of ≈ 0.3 ML/s, they found the transition height, h_t, strongly dependent on the indium content x, for values $x < 0.3$, with a weaker dependence for higher indium content; additional indium is most detrimental at first, and the influence on transition height diminishes in a non-linear fashion as the indium content increases. They observed vertical alignment of islands between successive quantum wells, suggesting that successively grown quantum wells are indeed not completely separate entities, and that each new quantum well is not to be considered as a separate planar film growth. Planar growth was achievable on substrates with strain variation, but growth tended to be faster in areas with less mismatch strain due to misfit dislocations aligned in layers of quantum wells beneath. The authors also find island growth to be strongly correlated with defects as examined by TEM.

Zou et al. (1993)[110] investigated both thin films and quantum wells of $In_xGa_{1-x}As$ for $x = 0.1$ and $x = 0.2$ using epitaxial lift-off and TEM, with a critical height of 240Å for $x = 0.1$ and 160Å for $x = 0.2$. They concluded that these values might be overestimated due to dislocation pinning, with all samples exhibiting initial threading dislocations regardless of layer height, but with a decreasing density with increasing film height, supporting the Matthews model mechanism. No transition height is reported, as all measurements are conducted ex-situ. We remark that the critical height is understood as the point of elongation of initial threading dislocations, and that initial threading dislocations are reported in all samples regardless of layer height.

Westwood et al. (1993)[111] grew thick films of $In_xGa_{1-x}As$ across a wide composition range ($0.039 < x < 1$), revealing an unexpected relationship between composition and material quality. Conducted at a low V/III ratio of As_4/(Ga+In)~ 0.7 and around 350°C, they observed expected trends with increasing indium content in the range of $0 < x < 0.5$, including increased threading dislocation density and wider diffraction peak full width half maximum (FWHM). Surprisingly, for higher indium content, $0.5 < x < 1$, these trends reversed, suggesting a more regular periodicity of misfit dislocations. The study found the highest degree of non-uniformity around $x \approx 0.5$ and not near $x = 1$ as might be expected from the increased lattice mismatch. Despite the mismatch variations, they consistently observed a transition from three-dimensional to two-dimensional growth as layers thickened.

Summary of observations for planar films

The growth of planar InAs on GaAs(001) under high arsenic pressures (V/III ratio around 10) and temperatures in the range of 450°C to 500°C typically follows a sequence of developmental stages, albeit with variations depending on specific conditions.

Initially, the first monolayer adheres to the GaAs substrate in a planar manner. The formation of three-dimensional islands at the transition

height (1 ML < h_t < 2 ML) marks the first significant development. This island formation involves considerable mass transport from the wetting layer and substrate, a process that is temperature-dependent and may lead to intermixing, thereby raising concerns about interfacial sharpness and material composition of the islands. This particular aspect of growth is not well captured in the standard Stranski-Krastanov (SK) growth model.

The evolution of these islands is complex. Their growth does not solely rely on the addition of adatoms but also involves a decrease in island diameter and an increase in island density with continued material deposition, a behavior contrary to Ostwald ripening expectations. Misfit dislocations, forming at the temperature dependent critical height (h_c ≈2-3 ML), are believed to nucleate primarily at island edges due to high stress levels. Subsequently, a phase of island coalescence occurs, eventually leading to a return to planar growth. This transition appears to happen relatively early in the growth process, around h_r ≈7 ML, and is also influenced by growth conditions.

Lower temperatures or arsenic pressures tend to delay these transitions. Specifically, lower temperatures may delay or even suppress island growth, reduce intermixing, and potentially delay the onset of misfit dislocations and island coalescence. Lower arsenic pressure might have similar effects on island growth and coalescence but could increase intermixing, which is undesirable from a design perspective.

In the growth of ternary $In_xGa_{1-x}As$, a lower indium fraction typically delays transitions within the range of $0 < x < 0.5$. The crystal homogeneity appears to be most compromised around $x \approx 0.5$, with either very high or very low indium fractions resulting in more uniform structures. The lower end is more homogeneous due to a lower density of misfit dislocations, while the higher end achieves a more regular periodicity for a network of misfit dislocations.

Finally, surface preparation and the use of surfactants add another dimension of tunable parameters for experimentalists. Surfactants have been shown to delay island growth, although the mechanisms behind this effect remain debated. Due to its additional complexity, additional discussion of surfactant-mediated growth is considered beyond the scope of this thesis.

Recap

The extensive research on InGaAs/GaAs crystal growth, encompassing models for growth phenomena, theoretical insights into misfit dislocations, and a variety of experimental observations, highlights the complexity and intricacies of this area of study. The significant discrepancies between different sets of observations, as discussed in the previous chapter, underscore the challenges faced in this field. These variations can be partly attributed to the factors mentioned in section 5.4 on planar experimental observations, including differences in growth conditions, characterization

techniques, and the inherent complexities of the materials and processes involved.

Building upon this somewhat fragmented understanding of the critical height in InGaAs/GaAs crystal growth, the next chapter delves into finite element-based simulations of misfit dislocations within a growing thin film heterostructure. By leveraging finite element modeling, the chapter seeks to shed light on the phenomenon of dislocation formation and configuration, contributing to a better theoretical and practical grasp of thin film heteroepitaxy in semiconductor materials.

6

Collective formation of misfit dislocations

The following chapter is based on my contributions to the paper *"Collective formation of misfit dislocations at the critical thickness for equilibrium nanowire heterostructures"*, ref. [P2], which studies strain relaxation mechanisms in Selective Area Growth heterostructures. The contents of this entire chapter therefore appear in said reference.

6.1 Strain and misfits

The presence of misfit dislocations (MDs) in epitaxial heterostructures alters the structural, mechanical, optical and electronic properties. The stress induced from elastic strain, originating from the mismatch between the lattice parameters of a growing thin film and the substrate, acts as a driving force for the formation of structural defects when the critical thickness is exceeded. Understanding the mechanisms that lead to formation of MDs at the critical thickness is therefore important in finding the limits of coherence for engineered epitaxial devices. The transition from elastic strain to plastic relaxation at the critical thickness in thin films has for these reasons been studied intensively in the past decades, and a number of general models for the formation of MDs have been proposed and tested[71–74, 76, 79–81, 84, 112–114]. Most of these models examine the limit for nucleation of a singular MD in an otherwise elastically strained and pseudo-infinite planar thin film, implicitly assuming a singular MD nucleation event.

A challenge in simulating the general case of MD formation for a simple interface (pseudo-infinite system) is finding boundary conditions which reduce the model to a finite size, while not affecting the physics. Using for instance symmetric or periodic boundary conditions will hinder modeling MDs as "additional" or "missing" crystal planes in a pseudo-infinite film, since the outer boundaries need the ability to move freely. For this reason we choose Selective Area Growth (SAG) as a model system, given that a full SAG nanowire geometry can be modelled to avoid challenges associated with boundary conditions for pseudo-infinite systems. Additionally, SAG offers the opportunity to design complex networks in the plane of the substrate, which makes it a promising platform for production of scaleable devices. For this reason, SAG methods for synthesis of nanowire heterostructure networks have received increasing interest in the field[49, 115–121].

Meanwhile, the initial growth stages of SAG nanowires closely resemble the trends observed from planar films, and studies of SAG allow us to probe the mechanisms for MD formation in general. We note the important difference of a bulk section of a planar structure, which do not have have freedom to expand over the boundary and hang over e.g. a buffer structure, like SAG does. We further note rotation of crystal planes at such overhangs, as discussed further in section 6.2.

The non-trivial morphologies found in SAG nanowires may be difficult to handle in a purely analytical framework, but they are fairly easy to define with the finite element method (FEM) software employed in our model. The morphologies add an interesting study of interplay between strain relaxation along different interfacial directions, and compared to large planar films, the SAG morphology may allow the growing film an additional spatial degree of freedom, altering the critical thickness.

From studies of the free-standing Vapor-Liquid-Solid (VLS) radial type

nanowires, we know that critical thickness can change dramatically [122–124] due to additional degrees of freedom from the change in morphology, with a limited nanowire radius in the VLS case. Theoretical models explain this phenomenon from comparison of a fully elastic model and a model exhibiting a single pair of perpendicular, interfacial MDs[125, 126]. The models predict how the critical thickness should scale with parameters such as nanowire radius and mismatch, and these are nicely summarized in a review by Kavanagh (2010)[127]. Unfortunately the VLS method lacks reliable ways of forming more complex nanowire networks in an experimental setting, and so our choice of SAG lets us work with a promising method somewhere between the planar thin film and the VLS nanowires.

Starting with the simplest case in section 6.2, we study purely elastic strain relaxation in SAG nanowires, to characterize the strain energy evolution for different growth stages. The shapes studied are those observed in experiments[115–117], appearing to be approximately equilibrium shapes given lowest surface energy configuration for the nanowire cross section. Building on these examinations, in section 6.3 we subsequently study elastic and plastic relaxation in SAG nanowires with dislocations as "additional" crystal planes. The FEM simulations are carried out for a wide range of mismatches and MD densities, finding the equilibrium configurations at the critical thicknesses from comparison between the elastic and plastic configurations. We study in particular plastic strain relaxation of a ⟨110⟩ orientated nanowire on a (001) substrate and buffer, and find a first order-like transition as a function of the extensive parameter film thickness, from a fully elastic configuration to one with a network of MDs formed collectively – a conclusion expected to carry over to other heterostructures subject to in-plane strain caused by a lattice mismatch. In later sections it will be discussed how dislocation formation observed experimentally in literature, for instance in islands, does not represent a SAG system of these conditions, and we propose an experiment to investigate our simulated predictions empirically. Lastly we analyze the stationary MD densities and show critical thicknesses and MD densities as functions of mismatch, finding a weaker dependence on mismatch than on e.g. morphology. This further allows for study of different fractions of plastic relaxation as opposed to elastic.

6.2 Purely elastic strain relaxation

Figure 6.1a presents a stereographic projection of the typical nanowire types available on (001) substrates. The purely elastic simulation features a translationally invariant segment, using three symmetry planes as illustrated in figure 6.1b along with an example of a preliminary mesh. We assume for simplicity that the buffer (region separating the conducting nanowire channel from the substrate) is relaxed to the underlying substrate. More details on strain implementation and calculation of strain

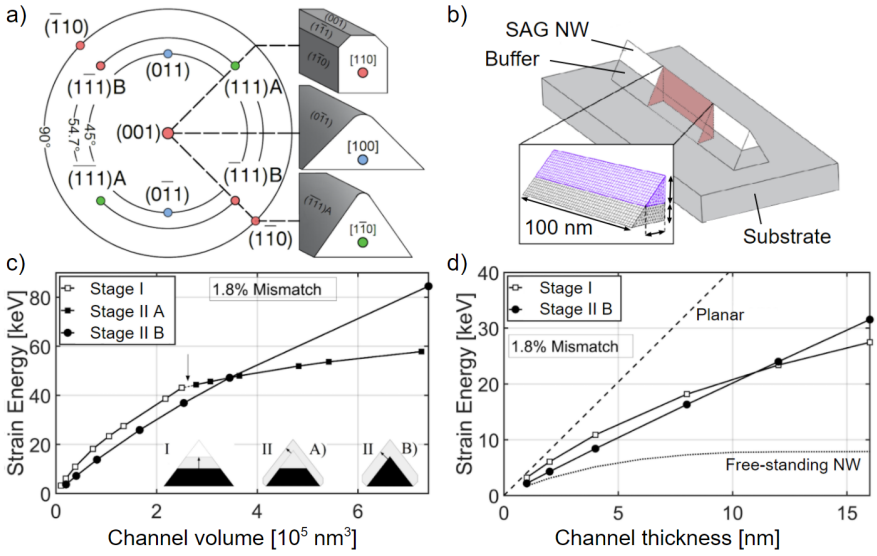

Figure 6.1: **Elastic growth of translationally invariant nanowires. a)** Linear stereographic projection of SAG nanowires grown on (001) substrate. **b)** Sketch of a SAG nanowire on a substrate with indicated symmetry planes, and a mesh example in zoom-in. **c)** Total elastic strain energy per 100nm section length of a ⟨100⟩ nanowire as a function of InAs transport channel volume V_{InAs} on a $In_{0.75}Ga_{0.25}As$ buffer (approx. 1.8% mismatch). Insets (InAs: grey, InGaAs: black) illustrate three types of cross sectional shapes. Growth stages are described further in the main text. **d)** As c) except investigated as a function of the thickness of the growing layer, where the dotted line represents a free-standing nanowire model at same mismatch and interfacial area. The free-standing nanowire is simulated as hexagonal in cross-section, protruding normal to a {111} substrate. We consider only half a stage II B) nanowire, as the two sides have little to no strain field interplay.

energy density (SED) in the FEM software COMSOL[128] in the supplementary section later.

Varying geometric parameters allows for analysis of the dependence on dimensions, shape and size of the structure. In an actual growth environment these parameters can be controlled by lithographic patterning and adjusting growth time, flux compositions and temperature. These simulations are run for an InAs nanowire on an $In_{0.75}Ga_{0.25}As$ buffer grown in the ⟨100⟩ direction with {110} side facets (see figure 6.1a). In figure 6.1c we show three different variations of this morphology, where stage I represents a transport channel grown from a thin layer on the buffer to a full pyramid shape with fully formed facets. We regard this shape to be an approximation of the lowest-energy shape as dictated by the surface energy densities associated with different crystallographic orientations.

The other morphologies represent overgrowth, where stage II A) specifically represents a layer beginning to form on a fully grown stage I nanowire, and the transition is marked with an arrow in figure 6.1c. We conclude that for our model, overgrowth contributes to total strain at a lower rate than stage I growth. We also see that stage II B) can accommodate higher mismatch for lower transport channel volumes, but also that this becomes unfavorable at larger channel volumes. All three stages exhibit sublinear increase in total strain energy for very large transport channel volumes. We note that the simulated interface area is kept constant between these morphologies for comparison. In figure 6.1d we investigate stage I and stage II B) and the strain energy dependence on the thickness of the InAs layer. For stage II B) we consider only half of the wire (cut along the axial direction), re-dimensionalized so that the interface area is equal for both morphologies, considered a normalization to interface area. We further compare to a free-standing nanowire with identical interface area, which is not constrained by symmetry planes. We find this free-standing type nanowire to be favorable in comparison to SAG at all thicknesses, which is expected since the free-standing nanowire is less constrained. We note that the graphs for stage I and stage II B) cross each other at approximately 11nm in panel 6.1d. This is due to stage I gaining less volume per unit layer thickness, as the triangular cross section becomes thinner towards the top. Hence, this crossing is absent in the panel 6.1c displaying the energy as a function of transport channel volume.

All cases compare favorably to the planar growth of thin film on a planar substrate, which is shown as the dashed line in panel 6.1d. The thin film is a rectangular structure with symmetry planes on all four sides to emulate a pseudo-infinite plane. For the thin film case, a mismatch of 1.8% ($InAs/In_{0.75}Ga_{0.25}As$) corresponds to a critical thickness of $h_c \approx 4.8$nm according to Matthews model[112], depending on the exact Burger's vector in the strained top layer. This highlights the morphological advantages of a SAG buffer, where the nanowire can relax strain by a rotational degree of freedom which has also been shown by other authors[115].

6.3 Plastic strain relaxation

As the crystal volume of a lattice mismatched heterostructure increases during growth, the excess energy increases until a critical thickness is reached, at which point MDs are formed to lower the total energy, most often edge dislocations along the interfaces [115]. We are interested in understanding the limits of fully elastically strained heterostructures as a function of shape, volume and composition (which defines the lattice mismatch).

In a simple 1-dimensional case, the spacing between dislocations is generally given by: $d = |\vec{b}|/(\delta - \varepsilon)$, with $|\vec{b}|$ being the length of the Burger's vector, δ being the mismatch and ε being the average remaining elastic

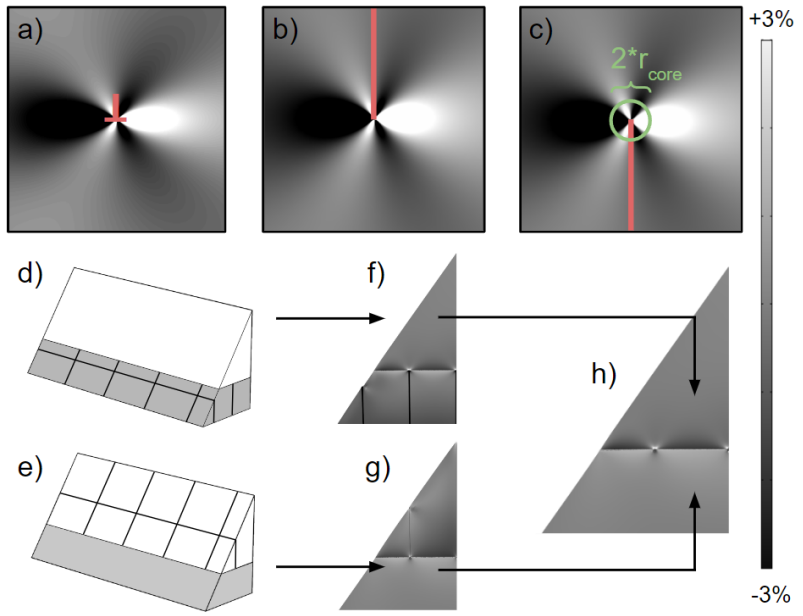

Figure 6.2: **FEM simulations of dislocations.** Top row: XY-components of stress fields caused by an edge dislocation at the markers. **a)** Analytical solution by Head [129]. **b)** and **c)** Results from 2D FEM simulations with dislocations modeled as a planes indicated by markers, with strain (+1) and (-1) respectively. Panel **c)** additionally shows the region near the core excluded from energy calculations, size greatly exaggerated for clarity. **d)** and **e)** 3D FEM models of ⟨110⟩ type nanowire (substrate not shown) with $\frac{a}{2}\langle 110\rangle$ dislocations modeled as vertical planes with strain (+1) and (-1), respectively. **f)** and **g)** Horizontal components of strain resulting from models d) and e) with 3% mismatch (InAs/$In_{0.58}Ga_{0.42}As$ buffer). **h)** Composite image of results from the two models in panels f) and g). Colorbar applies to a-c) and f-h).

strain. Therefore "full plastic relaxation" corresponds to $\varepsilon = 0$ with a corresponding density of dislocations. However, there will be a certain fraction of elastic vs. plastic relaxation that will display the minimum strain energy, and we can not in general expect full plastic relaxation. As such, we need to examine configurations with different MD densities in order to determine the critical thickness and the associated equilibrium configuration. As a first approach the dislocations are assumed to be equidistant, but distribution of strain may not be spatially uniform. Should material concentrations of e.g. In and Ga also be spatially non-uniform, it may be expected that dislocations form an irregular network.

Figure 6.2d shows a model of a ⟨110⟩ type nanowire with edge MDs of in-plane Burger's vectors of type $\frac{a}{2}\langle 110\rangle$, where a is the lattice parameter. The dislocations are here modeled as planes in the buffer with thickness

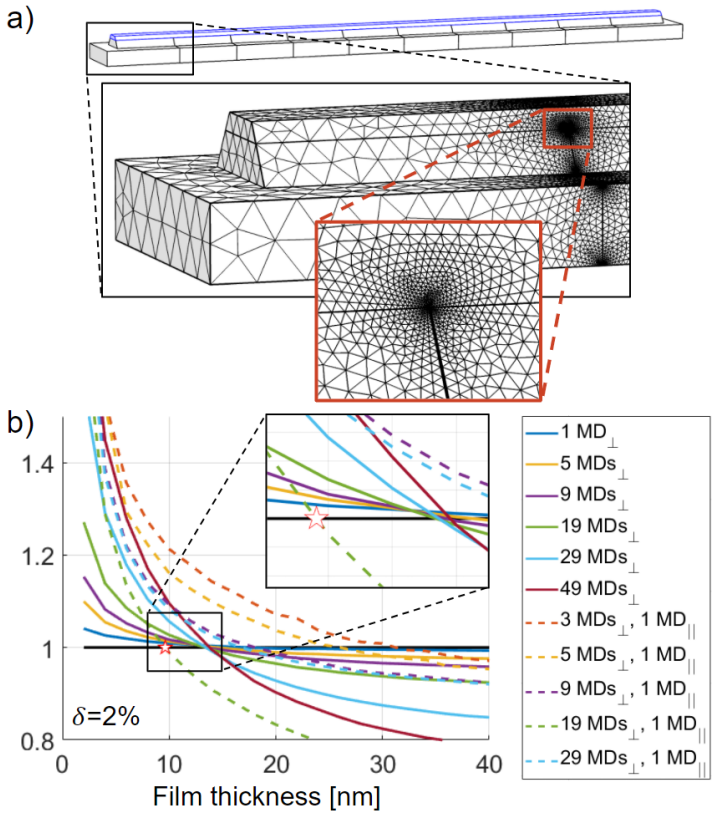

Figure 6.3: **Model and strain energy as function of film thickness. a)** Model along with a zoom section displaying a preliminary mesh with increased density near the dislocations. **b)** Total strain energy of different plastic configurations in units of the elastic configuration at the corresponding film thickness for a mismatch of $\delta = 2\%$. Note that the first plastic configuration to become favorable compared to the elastic case displays a network of MDs rather than one singular MD. The dimensions of the interface in the model are 125nm by 4μm.

matching the length of the Burger's vector and positive unity strain (normal to the planes) simulating "additional" crystal planes due to misfit dislocations at the interface. This ensures the correct effect of MDs in the transport channel, but leaves artifacts in the simulations of the buffer and substrate where the "additional" planes should not in general be strained relative to the surrounding material far from the interface. We emphasize that this method works for finite-size structures such as the SAG morphologies chosen here, and conversely this method is incompatible with simulations of pseudo-infinite systems using fixed position symmetry planes, because they inhibit the strain-relaxing displacement generated

by the additional crystal planes.

An alternate method simulates the same dislocations as "missing" planes in the transport channel with negative unity strain (figure 6.2e). This creates the correct effect in the buffer and substrate, while the unwanted artifacts are now found in the transport channel. The dislocation planes end at the nanowire-buffer interface where the dislocations are situated[115]. In panels 6.2a-c we compare these two methods to the analytical solution of stress fields associated with dislocations at the interface of two semi-infinite solids in 2D as found by Head (1953)[129], which combined with mesh convergence studies give us confidence that we have reached a sufficient resolution. While we find a clear convergence in the elastic simulations at cell sizes of 10-20nm, the characteristic cell size near the dislocation cores is on par with the length of the Burger's vector ($|\vec{b}| \approx 0.4$nm). The two methods can be combined graphically to yield the results shown in figure 6.2h, with a complete solution being to run both simulations and consider in each only the correctly affected domains. Since by far the biggest contribution to the strain energy ($\simeq 99\%$) is found in the transport channel on top of the buffer, we continue only with the MD model first described (figure 6.2d)

As seen in figure 6.2a-c, a small region around the dislocation cores becomes very highly strained. As a result, the elastic theory employed for evaluation of the SED is locally no longer valid, and an alternate method is needed if one wishes to evaluate the strain energy included in regions near the dislocations. We are concerned with the total strain energy in the nanowire, which comprises by far the dominant energy contribution compared to the buffer and substrate. In order to evaluate the "invalid regions" mentioned above, we modify the "Volterra method"[113] or "empirical method"[130], excluding slightly larger cylindrical cores of radius $r_{\text{core}} = |\vec{b}|/2$, with $\vec{b}$ being the Burger's vector, arguing that the dominant energy contribution inside this range is due to the rearrangement of chemical bonds. We account for these bonds by adding an energy per unit dislocation length from the melting approximation given as $E_m = Gb^2/2\pi$ where G is the shear modulus of the transport channel, in this case InAs. This is likely an overestimate of the dislocation line energy density, which we will reflect upon below.

Our simulations were carried out using models of the type in figure 6.3a (interface width 125nm, channel length 4μm), with "transverse" dislocations as equidistantly spaced "additional" planes in the substrate and then buffer. The orientation was chosen with $\langle 110 \rangle$ along the nanowire axis and $\{111\}$ type side facets (see figure 6.1a). The material composition of the buffer was varied with corresponding changes in material parameters according to Vegard's Law, and chosen to emulate mismatches from 1% to 4% corresponding to InAs on $In_xGa_{1-x}As$ with x between 0.86 and 0.44. In all cases the composition within each region (substrate, buffer, nanowire) was chosen as spatially uniform for simplicity, and the distribution of dislocations as equidistant to simulate an equilibrium layer-by-layer growth

as opposed to e.g. island growth. The thickness of the thin film was varied (akin to the method employed for figure 6.1d) to emulate different stages of approximate layer-by-layer growth throughout.

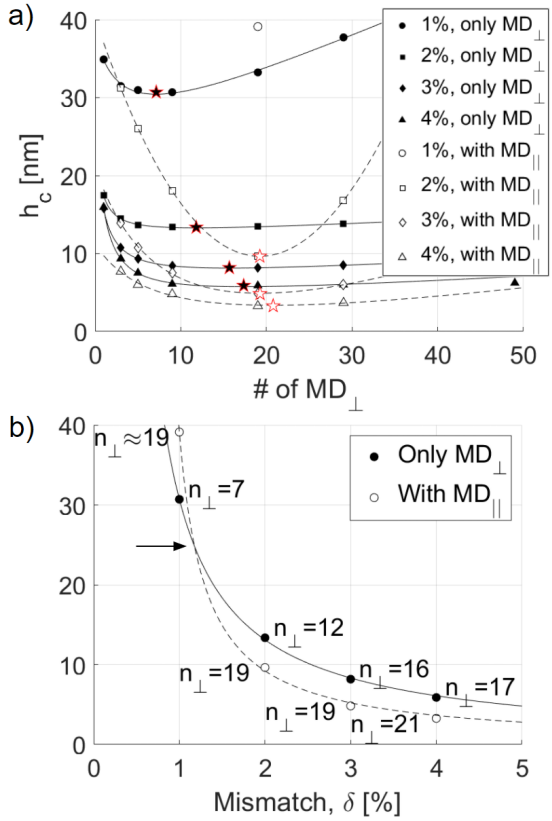

Figure 6.4: **Fitting critical thicknesses.** Panel **a)** shows the predicted critical thicknesses, assuming a set number of dislocations for each of the four mismatches. Markers denote minima from fits. Panel **b)** shows the minima from a) for each mismatch (δ) along with the corresponding number of dislocations found from fits. Fit types are described in the main text. The dimensions of the interface in the model are 125nm by 4μm.

6.4 Results

Figure 6.3b shows the strain energy of plastic configurations in units of the strain energy for the purely elastic configuration as a function of film thickness for a mismatch of $\delta = 2\%$. From closer examination we notice the first plastic configuration to become favorable is not the one with a singular

dislocation. This is a general feature across the mismatches examined, but more notable for higher mismatches. This suggests that onset of misfit dislocations at the critical thickness is a first order-like transition in an extensive parameter, to a state which becomes stable when a certain equilibrium MD density is achieved. The transition from elastically strained to a partially plastically relaxed state is characterized by both a critical thickness and a characteristic density of MDs. We note that a lower value for the dislocation line energy density would lead to configurations with a higher MD density being more energetically favored. Thus, our results for the characteristic density of MDs at the critical thickness should be considered a lower bound, based on the melting approximation mentioned in section 6.3 above.

In this study we have limited ourselves to one axial dislocation running along the center of the nanowire, and note that a more complete examination would have to deal with a much larger parameter space of both number and positions of axial MDs. We also note the general feature that higher mismatches tend to favor configurations with more MDs. For the 1% mismatch case the equilibrium configuration at the critical thickness has only transverse dislocations ($MD_\perp$), which could be interesting for engineering of MDs in heterostructures. However, for the mismatches of 2%, 3% and 4% the equilibrium configurations at the critical thicknesses have both the axial and transverse dislocations present. This could prove useful for analysis, as the lack of an axial MD from cross sectional TEM of a high mismatch structure could indicate that the entire structure is purely elastically relaxed.

The question of MD configuration at the critical thickness is examined further in figure 6.4a which shows the points where different configurations become favorable compared to the purely elastic case. For a given mismatch the lowest of the critical thicknesses is the predicted equilibrium critical thickness, and a specific MD density is associated with this. The guidelines in figure 6.4a are fits to the form $h_c = an_{\text{disl}} + b + c/(n_{\text{disl}} + d)$, where n_{disl} is the number of dislocations. The minima from figure 6.4a (marked) are extracted from the fits and plotted in figure 6.4b along with the associated number of MDs and new fits of the simpler form $h_c = \alpha/(\delta + \beta)$ where δ is again the mismatch.

The variables $\alpha_\perp = 22.8\text{nm}$, $\beta_\perp = -0.26\%$, $\alpha_\parallel = 12.1\text{nm}$, and $\beta_\parallel = -0.69\%$ are found from the fits for configurations without and with the axial dislocation, respectively. For mismatches below $\delta^*_\parallel = 1.2\%$ (marked by an arrow in figure 6.4b), the configuration at the critical thickness shows no axial dislocation. Interestingly, the density of transverse MDs at the critical thickness only increases slightly while increasing the lattice mismatch from 1% to 4%. In the entire range, spacing between MDs is found to be around 200nm, corresponding to a partial plastic relaxation of approximately 0.2% misfit strain (emphatically *not* 0.2% *of* the misfit strain). In the case of 2% misfit we thus find the fraction of plastic relaxation to be 1/10. The weak dependence on misfit strain and low value suggest the

equilibrium configuration at the critical thickness is more dependent on e.g. morphology, and the melting approximation overestimating the dislocation line energy density. Further work for investigating this is discussed below.

The fit forms and variables found suggest a divergence of the critical thickness at a mismatch of a quarter of a percent. To ensure a fully elastic growth in stage 1 however, it is only necessary for the critical thickness to be larger than the thickness of the transport channel grown. Due to the geometry chosen for the model, the stage 1 transport channel can grow to a maximum thickness of $h_{\max} = w/\sqrt{2}$, where $w = 125$nm is the width of the interface. In our model this can be accommodated elastically at a mismatch of $\delta^* = 0.52\%$, meaning a buffer of $In_{0.93}Ga_{0.07}As$. While a buffer this high in In concentration may cause issues in containing the wavefunction to an intended transport channel, we note the height of 125nm is only an example, as is the chosen elements of In, As and Ga. We note that while all the critical thicknesses quoted are specific to the morphology, dimensions and materials, the method presented can be used for examination of other combinations and structures.

6.5 Discussion and conclusion

We find the mechanisms of strain relaxation in lattice-mismatched SAG nanowires to be distinctly different from reports in literature on planar heterostructures and on free-standing nanowires[125, 126]. Compared to planar thin films, the additional elastic relaxation for SAG stems from the rotational degree of freedom for relaxation transverse to the nanowire axis which in principle can overshoot the bulk relaxed values, giving additional room for elastic relaxation along the nanowire axis through the Poisson effect. We identify three different growth stages, all of which are energetically favorable compared to planar thin film growth, and all of which are sublinear but quickly become approximately linear with different dependencies on layer thickness, favoring stage II A).

Our findings establish a relationship between transport channel layer thickness and MD density for a SAG nanowire morphology, similar to that between nanowire radius and misfit percentage as found by Ertekin et al. (2005)[125] and Glas (2006)[126] for VLS nanowires. This highlights the difference between SAG and free-standing nanowires. For comparison we quote the experimentally found critical thickness of $h_{c,\text{film\%}} = 1.71$nm for planar thin film growth of InP on GaAs at 3.8% lattice mismatch [131]. This shows the ability for elastic relaxation in SAG nanowires as somewhere between the highly constrained planar thin films and the nearly unconstrained free-standing nanowires of VLS.

We compare to previous efforts in using FEM to analyze misfit dislocations such as Ye et al. (2009)[132], which also use initial strain as a numeric technique, but fails to include both elastic and plastic relaxation

simultaneously and naturally does not take the spatial freedoms and lattice directions of SAG nanowires into account. Therefore we believe our methods are novel and relevant for finite-size morphologies across materials, and the results can be compared to physical samples by analysis of e.g. atomic resolution TEM with GPA[133, 134].

It is appropriate to discuss this abrupt and collective formation in relation to observed formations. As done by LeGoues et al (1994)[135], UHV TEM can be used in situ to observe singular MD formations in island growths, with accompanying changes in growth velocity immediately before and after nucleation events. They provide rudimentary theoretical considerations with equilibrium assumptions, but we consider their model incomplete as it does not include strain energy as a driving force and does not explain the preference for island growth over layer-by-layer. We understand that in our study we have specifically simulated an equilibrium environment, and created a rigorous framework incorporating strain energy and additional references. A later study by Merdzhanova et al (2006)[136] uses a more time-efficient AFM method, and notes higher growth temperatures consistently giving rise to more singular nucleation events, as well as a dramatic change in the size of islands. Particularly the balance between coalescence of neighbouring islands growing simultaneously, as opposed to islands growing smaller when located in the depletion zone of a larger island, is affected. They do not present a complete theory for this behavior, but suggest a scenario qualitatively involving material intermixing. We note these points to be different from the assumptions within our model, and that temperature dependencies agree well with a non-equilibrium nature of the process. As such we find the discrepancies to our model as expected, and they underline the potential in understanding the equilibrium and non-equilibrium divide in phenomena and behavior. In particular, the role of material intermixing could be introduced and studied within our framework, posing an immediate candidate for further work. Among other things it would affect the spatial distribution of strain, which may cause the optimal network of dislocation to be non-equidistant.

Additionally it would be possible to design an experiment using low growth rate, high temperatures and low mismatch, which would be a better representation of the simulation in reality. High energy presumably allows for breaking of kinetic barriers and avoiding local minima, approaching our predicted global minimum of collective formation, and low mismatch with a low growth rate allows for true layer-by-layer growth, seeing as the island growth seen in literature cannot represent this system. We propsoe using in-situ observation of strain in the layer-by-layer growth, for instance using a curvature tool as done by Gilardi et al (2018)[137], to investigate to what degree the stationary (non-time dependent) assumptions of the model are correct, when the other conditions as described above are fulfilled. We expect the results to be strictly different from the discussed literature, where the conditions are not fulfilled.

In summary we present a novel method for introducing plastic relaxation from MDs as localized FEM features in heterostructure simulations, allowing an examination covering different morphologies and MD densities. This leads to our prediction of collective rather than singular onset of MDs at the critical thickness, which is a novelty. For SAG nanowire growth in stage I, we find critical thicknesses of $h_{c,1\%,\perp} = 30.7$nm, $h_{c,2\%,\parallel} = 9.6$nm, $h_{c,3\%,\parallel} = 4.8$nm, and $h_{c,4\%,\parallel} = 3.3$nm for 1%, 2%, 3%, and 4% mismatch, respectively, as summarized in figure 6.4. In all cases we find that collective formation, as a first order-like transition as a function of film thickness, is favorable compared to singular onset. For mismatches below $\delta^*_\parallel = 1.2\%$ we find that the equilibrium configuration shows only transverse dislocations, while for mismatches above this value both axial and transverse dislocations are expected. At the critical thickness, the density of MDs suggests initial plastic relaxation of approximately 0.2% misfit strain in the range of misfits examined. Further studies are needed in order to examine in more detail how this initial plastic relaxation changes with morphology, compositions and different values for the dislocation line energy density. We argue that our results are relevant for general heterostructures, predicting that a first order-like transition in our finite-size case carries over to e.g. a pseudo-infinite planar heterostructure.

6.6 Supplementary information

COMSOL models for FEM simulation

The FEM simulations were carried out as 3-dimensional Stationary studies with the Solid Mechanics part of the Structural Mechanics module in COMSOL Multiphysics[128]. In COMSOL, materials are defined with a variety of different properties, either from scratch or from a library of predefined materials. The important properties are the Bulk Modulus, Poisson ratio and elasticity matrix. The entries of the elasticity matrix are also used for calculations of strain energy density from linear elastic theory. The Linear Elastic Material sub-menu of the Solid Mechanics part of the interface allows for imposing initial strain in select parts of any geometry built.

Initial tensile strain is employed (in-plane with the interface) in the nanowire corresponding to a chosen lattice mismatch between nanowire and the buffer, from which a balance of forces on each mesh point yields the final configuration with forced coherence at the interface. The strain energy density (SED) is found locally from derivatives of the displacement according to equation 6.1:

$$U_{\text{SED}} = \sum_{ijkl} \frac{1}{2} c_{ijkl} \varepsilon_{ij} \varepsilon_{kl} \tag{6.1}$$

with c_{ijkl} being the stiffness coefficients and ε_{ij} components of the strain tensor. Evaluations of the resulting strain must properly account for the initial strain imposed. The relevant bulk parameters are the lattice and elastic constants and for $In_xGa_{1-x}As$, where we assume linear interpolation between the respective parameters of the component materials (Vegard's law).

Some drawbacks do arise from the static and continuous simulations of a dynamic and atomistic physical system, and we should address those here. Drawbacks include but are not limited to a lack of polarity, static elasticity and lattice constants, and an assumption of uniform composition within each region. While these drawbacks are relevant and present, plenty of results are still obtainable, and simulations of strain relaxation and dislocations in SAG heterostructures could prove a central tool for achieving dislocation free, scalable, high mobility devices.

Finite length effects

Turning our attention to the regions near the nanowire ends, figure 6.5a shows a nanowire morphology for stage I growth with only two symmetry planes imposed to examine finite length and the corresponding gradient in elastic strain energy density towards the end of the nanowire. The translationally invariant nanowire segments investigated in the main text relax strain primarily by rotation of crystal planes in directions perpendicular to the nanowire axis. Near the ends of the nanowires, rotation along the nanowire axis provides an additional degree of freedom for relaxation.

Figure 6.5b shows the distribution of SED in the stage I model. Unsurprisingly, the general trend shows a higher SED near the interface tapering off with distance. For the stage I growth we see the SED decreasing as we move from the middle towards the nanowire sides. Figure 6.5c shows a comparison of the average strain energy density of 50nm sections in the center and end of the nanowire. The simulations are run for a ⟨100⟩ type nanowire at 3% mismatch ($InAs/In_{0.58}Ga_{0.42}As$) nanowire, and we investigate the geometric parameters of nanowire length and buffer height. We notice a clear trend of the end region converging faster and at lower values. We also see target dimensions of a buffer in order to minimize strain energy. This method can be employed for examination of parameters in both fully elastic and plastic configurations.

Strain formulation

For pedagogical reasons, the explanations above are phrased in terms of linear strain, that is the "intuitive" strain:

$$\varepsilon_l = \frac{L - L_0}{L_0} = \frac{L}{L_0} - 1 \tag{6.2}$$

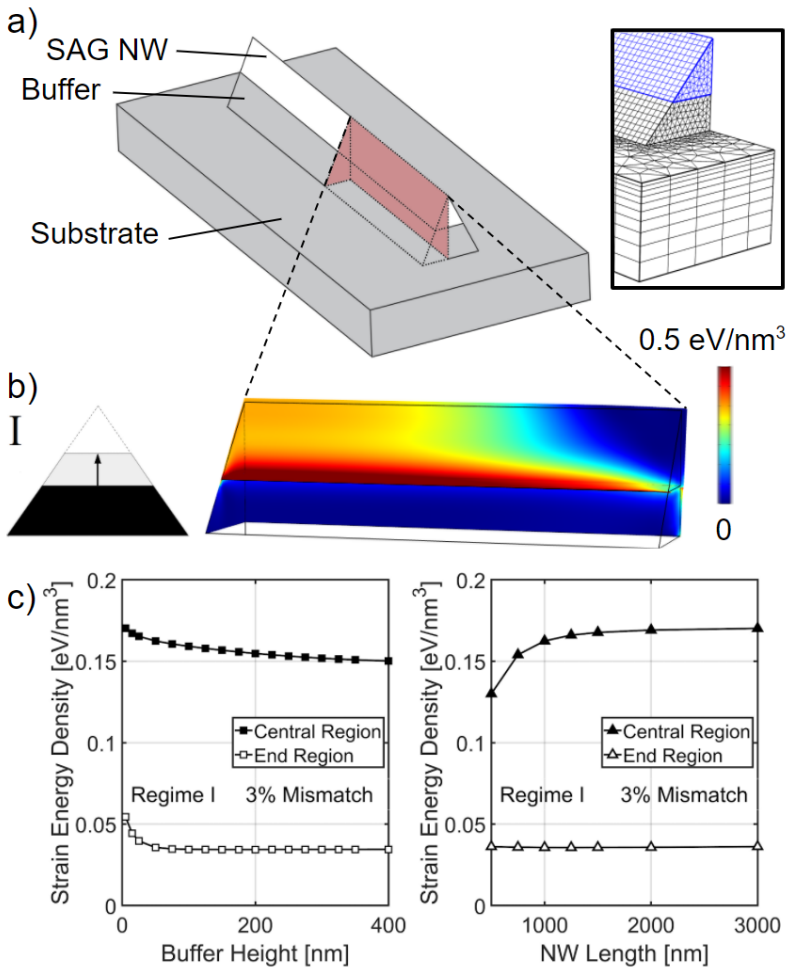

Figure 6.5: **Finite length effects, 3% mismatch** ($InAs/In_{0.58}Ga_{0.42}As$)**. a)** Illustration of end section with symmetry planes. **Box:** Example mesh of end section. **b)** Distribution of strain energy density on buffer-nanowire interface as well as both symmetry planes for a fully triangular shaped nanowire (fully grown stage I). **c)** Strain energy in a central cube as a function of size parameters, showing length scales for decoupling of the center to the end effects.

with ε_l being the linear strain and L being the final length of an object with unstrained length L_0. In this linear strain framework, the strain is just the fractional elongation of the object. The reader should note, that several frameworks for strain are available, and notably that strain in the Solid Mechanics module of COMSOL[128] is Green-Lagrange strain:

$$\varepsilon_{GL} = \frac{1}{2}\left[\left(\frac{L}{L_0}\right)^2 - 1\right] \tag{6.3}$$

The reason is that GL-strain is appropriate for larger strains where linear approximations do not function. Other FEM packages may employ different strain frameworks such as Almansi or logarithmic strain, and adequate adjustments should be taken to account for this. E.g. we note that $\varepsilon_l = +1$ corresponds to $\varepsilon_{GL} = 3/2$, while $\varepsilon_l = -1$ corresponds to $\varepsilon_{GL} = -1/2$. For the purposes of this supplemental, we shall continue to phrase strain in the linear terms, since it allows for a more intuitive understanding, keeping in mind that the specific implementation is recast depending on the strain framework of the FEM software.

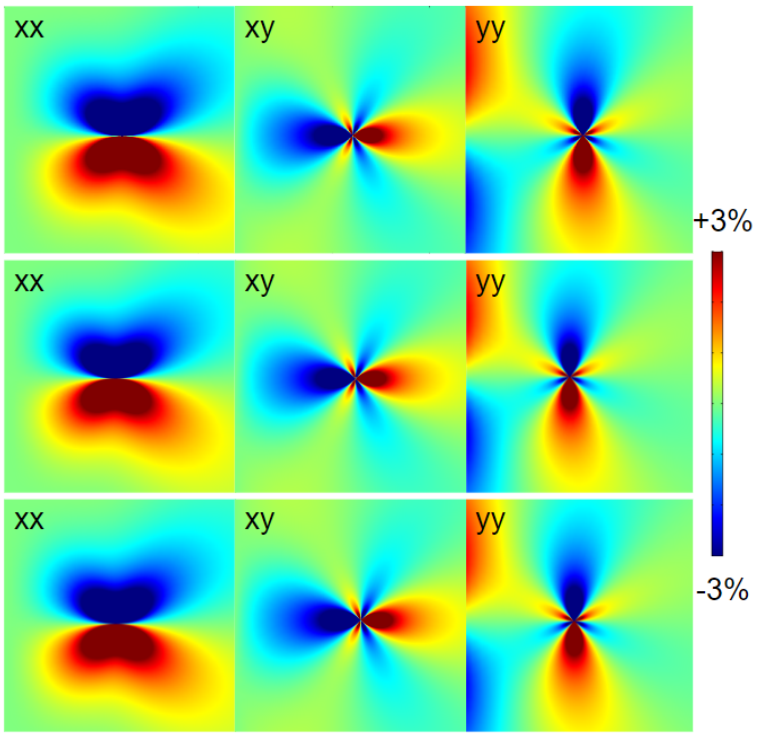

Figure 6.6: **Method comparison:** Stress components caused by an edge dislocation near a fixed surface (left side). **Top row:** Analytic solution by Head [129]. **Mid row:** Simulation using (+1) strain method. **Bottom row:** Simulation using (−1) strain method. The middle column is also shown in grayscale in figure 6.2 above.

Analytic solution and method equivalence

The default simulation including MDs modeled as planes with +1 strain in the buffer, corresponding to the "additional" crystal planes. As mentioned in the main text, this ensures correct boundary conditions from the interface and above, while the boundary conditions inside the lower part are obviously incorrect, since the imposed planes are not actually strained compared to the surrounding material, as confirmed in e.g. geometric phase analysis of atomic resolution TEM. This method is especially viable, since we are mostly concerned with the variations in the transport channel. Equivalently we can model the MDs as planes with −1 strain in the wire, corresponding to the "missing" crystal planes. This method ensures correct boundary conditions from the interface and below.

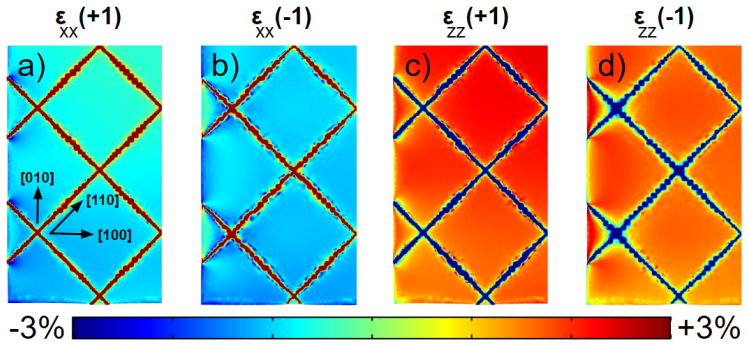

Figure 6.7: **Interface strain comparison:** Top views of a section of the nanowire at the interface between nanowire and buffer for a {100} type nanowire. **a)** Transverse (horizontal) strain component using the method with +1 strain in the buffer. **b)** Same as a, using the method with −1 strain in the nanowire. **c)** Out of plane strain component, +1 strain method. **d)** Same as c, using −1 strain method.

The simulation results should agree with analytic solutions, e.g. solutions by Head [129]. Figure 6.6 shows different components of a 2D stress fields caused by an edge dislocation, as analytic solution or modeled by the methods mentioned above. The figure shows a clear equivalence between all three methods, validating the simulation method. For the purposes of our simulation the concept is straight-forwardly extended to three dimensions. Dislocations are associated with an energy, which is proportional to the square of the length of the Burger's vector. This makes the lowest energy MDs of zinc-blende those with Burger's vectors of type $\frac{a}{2}\langle 110\rangle$. For a $\langle 100\rangle$ nanowire on a (001) substrate, these types of MDs will simultaneously relax strain in two out of the three directions: axial, transverse and out of plane. In the case of a $\langle 110\rangle$ nanowire on a (001) substrate, there exist favorable MDs which relax strain in distinctly axial, transverse or out of plane directions as well as MDs which relax all direc-

tions simultaneously. This was illustrated in the main text with the model for formation of MDs. The method proposed here is equally well suited for MDs with other directions of Burger's vectors, as the strain associated with the MD can be defined independently of the MD plane.

Part III

Stencil based techniques

7

Stencil based techniques

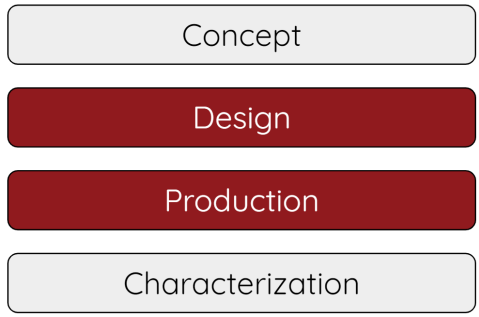

Figure 7.1: **Synthesis design and production stage:** These stages relate to the planned outcome of production as well as the actual synthesis of the circuit.

Switching from a mask-on-substrate to a stencil based technique, involves changes to the workflow of circuit synthesis. Specifically, it introduces the stencil as a stand-alone element with a separate design and production stage. We will expand on this below.

7.1 Introduction to stencils

Stencil lithography, employed in direct material deposition, presents a distinctly different approach compared to masks that adhere to the substrate. Stencils operate as separate entities positioned between the substrate and the beam source, creating patterns by casting shadows on the substrate. This blocks deposition[1] in all areas except those selected by the stencil apertures, essentially serving as an inverse representation of the desired pattern.

The advantages and disadvantages of stencil-based techniques, along with various use cases, are comprehensively reviewed by Vazquez-Mena et al. (2015)[138]. Here, we highlight some key aspects of stencil lithography, especially in the context of quantum applications:

Resistless patterning: One of the major benefits of stencil lithography is its resistless nature. In quantum applications, even trace amounts of residual resist or etching roughness can significantly affect device performance. Stencil based techniques, being fully resistless, offer a higher level of cleanliness than mask-on-substrate based methods, ultimately offering a path to enhanced device fidelity.

[1] I will cover stencil lithography, as it is employed in direct material deposition. Other use types such as stencil defined etching, or stencils used for lithographic exposure do exist, but they entail other considerations (i.e. etching proximity effects and optic interference), and are not within the scope of this thesis.

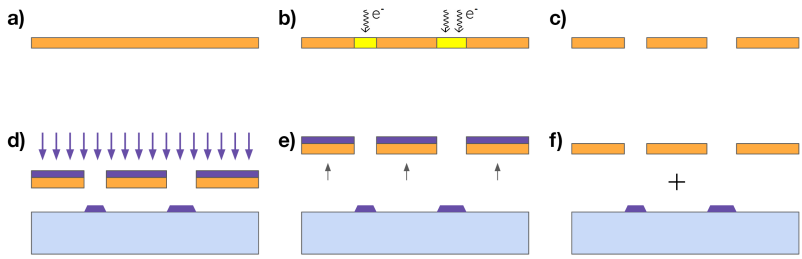

Figure 7.2: **Lateral patterning with stencil: a)-c)** A stencil (orange) made from e.g. Si or SiN is patterned with lithography and etching, leaving apertures in the stencil. **d)-e)** The stencil is mechanically mounted in a fixed position above the substrate (light blue), and material (e.g. a metal) is deposited. Material passes through the stencil apertures, leaving the intended pattern on the substrate, and the stencil is subsequently dismounted. **f)** The stencil can ideally be cleaned separately and prepared for reuse on another substrate.

Stencil reuse: Reusing stencils is not only cost-effective but also contributes to reproducibility, a critical factor in engineering and optimization processes[6, 7]. This reproducibility confirms the accuracy of identified process control parameters. The stencil itself acts as a checkpoint for characterization and optimization, separate from the in-situ ultra-high vacuum (UHV) device fabrication step which is usually associated with the majority of fabrication costs.

Topological restraints: Stencil based techniques face limitations with closed-loop type features due to the physical impracticality of having free-floating parts in the stencil. Unlike mask-on-substrate based methods, which do not have this issue since the mask directly adheres to the substrate, stencil techniques can overcome this through the use of stabilizer bridges[139], enhancing stencil stability for certain designs. We will explore this in more detail later in chapter 8.

Blurring/broadening: In the literature, blurring is typically attributed to two factors: geometric broadening from a finite source size and growth kinetics that permit material diffusion outside intended regions[139]. While geometric effects can be analytically treated and simulated, growth-related effects are more dependent on specific growth conditions. The interplay between pattern control and growth kinetics will be explored later, focusing on leveraging the advantages of blurring while mitigating its drawbacks through technical innovations.

In terms of pattern control, stencil based techniques merely control the flux distribution.

$$\frac{\partial \rho}{\partial t} = D\nabla^2 \rho - \rho\left(\gamma_{av} + \kappa_{as}\right) + \left(F(x) + \kappa_{sa}\right) \tag{7.1}$$

Equation 7.1 mirrors equations 2.12 and 3.1 but underscores the primary control input in stencil patterning: the flux distribution, explicitly represented as $F(x)$. This highlights the significance of a non-uniform flux distribution. Similar to Selective Area Growth (SAG), adjustments in temperature and pressures in stencil lithography uniformly impact all parameters. However, a key differentiator for stencil methods is the ability to modulate conditions through a controlled, non-uniform flux distribution.

Stencil circuit production workflow

The introduction of stencils in the circuit production workflow brings forth transformative changes compared to mask-on-substrate based methods. In mask-on-substrate approaches, the substrate is introduced post-design, followed by resist mask deposition and lithography. This process often suffers from conflation of multiple control parameters, as seen in figure 7.3 (left side, from the arrow and down). The substrate and mask go through a complex process step, where process control is intricate and the output is a function of a plethora of inputs.

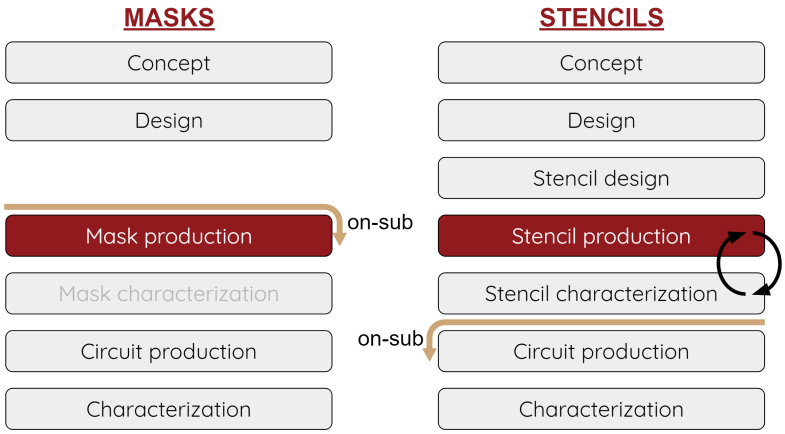

Figure 7.3: **Mask and stencil workflows: Left column)** A simplified workflow for the mask based technique. Once the desired design is decided upon, the mask production (resist coating, exposure, etching) commences, and everything occurs on the substrate. **Right column)** A simplified workflow for the stencil based technique. The additional steps from stencil design to stencil characterization are introduced, all before the substrate enters the workflow.

In contrast, stencil lithography offers a strategic checkpoint in the workflow. As depicted in figure 7.3 (right side), after the stencil is produced, it can be independently characterized, decoupling stencil creation from

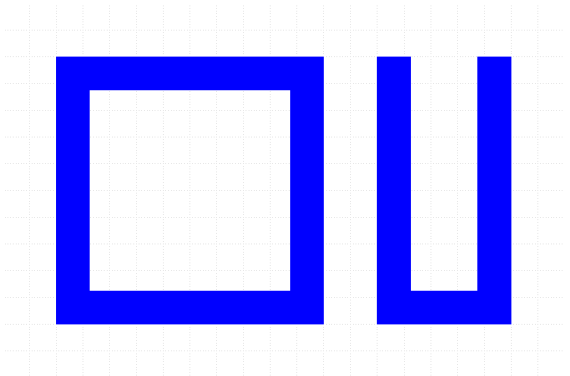

Figure 7.4: **Problematic stencil topologies:** Blue parts are design elements intended for deposition on the substrate. Surrounding white space is where the stencil would have to block deposition in order to achieve the intended pattern. The "square ring" on the left is topologically problematic with a stencil based technique, as the middle part would be detached from the surrounding stencil. The U-shape on the right has a cantilever extending from the top, which may or may not be mechanically unstable, depending on stencil material, preparation, thickness etc.

circuit production. This separation allows for an optimization loop specific to stencil production, facilitating improvements without involving the substrate or the ultra-high vacuum (UHV) system. This makes the process cost-effective and responsive to feedback.

Moreover, the use of cleanable and reusable stencils enhances reproducibility. The pattern-defining phase of production is standardized, ensuring consistent results across multiple manufacturing cycles. In essence, stencil lithography not only brings practical benefits like cleanliness and resistless patterning but also fundamentally restructures the circuit production workflow. This restructuring enables more efficient process control and optimization, crucial for the advancement of sophisticated technologies, particularly in the realm of quantum applications.

7.2 Stencil and source geometry

Considering the scenario of a stencil used in material deposition, we can explore how the stencil geometry influences the flux incident on the substrate. This exploration begins with a basic setup where a stencil of thickness τ is positioned above a substrate, separated by a gap g, with the stencil edge aligned at $x = 0$. This arrangement leaves the left side of the substrate covered by the stencil, while the right side is exposed, as illustrated in figure 7.5a. In this setup, the broadening effect of the flux near the stencil edge can be understood through geometric considerations. We assume

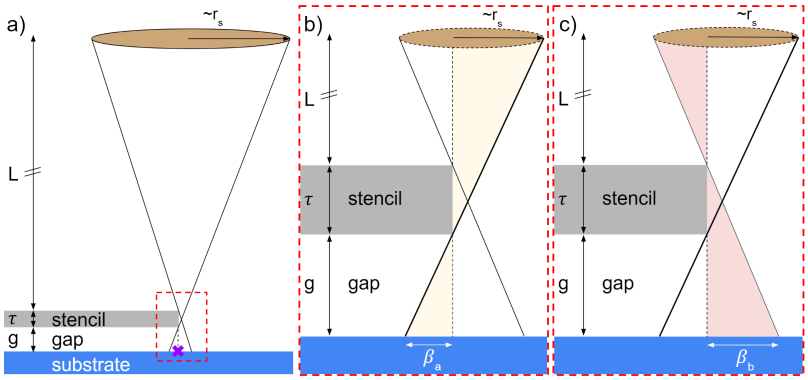

Figure 7.5: **Flux broadening at stencil edge: a)** Cross-sectional overview schematic (not to scale) of flux at normal incidence. Beam source of radius r_s is far away upwards at a distance of L. Purple cross denotes $x = 0$, directly beneath the stencil edge, with the stencil extending to the left. Red dashed box indicates zoom to relevant region in the following two panels. **b)** β_a is the distance from $x = 0$ to the furthest point under the stencil where direct flux still impinges due to the finite size of the source. **c)** β_b is the lateral distance from $x = 0$ to the furthest point on the open substrate where flux is still partially imparied by the stencil.

the flux source is circular, with a radius r_s, and located at a distance L from the top of the stencil. This distance L is measured from the flux source to the stencil top, but due to the micro- or nanoscale dimensions of τ and g, L can effectively be considered as the distance from the source to the substrate surface[2]:

$$(L + g + \tau) \approx L \tag{7.2}$$

When the stencil edge is aligned with the center of the flux source ($x = 0$), the point on the substrate directly beneath the stencil edge (marked with a purple cross in figure 7.5a) receives half the nominal flux, as it has a direct line of sight to exactly half of the source. This holds when the source size r_s is significantly larger than the active region on the substrate, making the lateral position of the stencil edge negligible in terms of flux distribution. In other words, we are neglecting wafer scale variations which may be of significance[140], depending on the dimensions of the system in question. With this in mind, we may also infer a *large source size approximation*, considering any point on the substrate approximately aligned with the center of the source[3].

[2] In our case of a micro- or nanoscale deposition, L is likely measured in 10s of cm with τ and g in the 100s of nm to a few μm range

[3] Note that this **does not** imply that every point on the substrate has direct line of sight towards half the flux source. Instead, it implies that the lateral position of the stencil edge makes a negligible difference in the case of a large flux source, as the entire stencil is approx-

Figure 7.5 also illustrates two types of broadening phenomena caused by the stencil. Despite the stencil blocking direct flux, the non-collimated nature of the beam allows for some flux to reach areas of the substrate underneath the stencil. This flux reaches the substrate at an angle (figure 7.5b), resulting in a broadening effect up to a distance β_a from the stencil edge. The extent of this broadening, β_a, can be estimated using the geometry of similar triangles illustrated in figure 7.5b:

$$\beta_a \approx \frac{g r_s}{L} \tag{7.3}$$

where we have used the large source size approximation along with equation 7.2.

Similarly, we observe partial obstruction of the flux by the stencil even in regions that are nominally unobstructed. This occurs within a distance β_b from the stencil edge, where the flux is gradually restored to its maximum value as the distance from the stencil edge increases. The situation is depicted in figure 7.5c. Here, β_b is likewise determined using the geometry of similar triangles shown in the figure:

$$\beta_b \approx \frac{(g+\tau) r_s}{L} \tag{7.4}$$

Thus, $\beta_a \leq \beta_b$, and $\beta_a \approx \beta_b$ applies whenever the stencil is very thin: $\tau \ll g$[4].

7.3 Flux tapering function

The function that describes how the flux varies from $x = -\beta_a$ to $x = \beta_b$ will depend on the characteristics of the flux source. Assuming a circular source with uniform and isotropic flux output, the tapering function, $f(x)$, should relate to the area of a circle as we traverse its diameter. This function should satisfy $f(0) = 1/2$ and $f(\beta_b) = 1$, all expressed in nominal flux units (fraction of source circle within direct line of sight). Our movement with x across the diameter should be normalized to β_a on the left side, and to β_b on the right side.

For a unit circle described by $x^2 + y^2 = 1$, we find $y = \sqrt{(1 - x^2)}$, which gives the height of a semi-circle at any given point along its diameter. Doubling this value gives the full circle height. To obtain the integrated area under this curve (and hence, the flux distribution), we take the anti-derivative:

imately aligned with the source center. For reference, the source size will often be on the order of a few cm, with stencil designs displaying lateral distances on the order of hundreds of μm.

[4] A similar geometric examination of β_a broadening is included in a paper by Vazquez-Mena et al. (2009)[141]. However, their derivation primarily considers β_a in the case of a thin stencil ($\tau \ll g$), and the flux slope from partial shadowing labeled β_b here is thus neglected. Similarly, no considerations for cases other than normal incidence are included.

$$p(x) = 2\sqrt{\left(1-x^2\right)} \quad \Rightarrow \quad P(x) = x\sqrt{\left(1-x^2\right)} + \arcsin(x) + c \tag{7.5}$$

where our circle now runs the x-coordinates from negative unity to positive unity. Normalizing the area from integration to unity instead of π for the unit circle, and using the integration constant c to adjust our function to meet the requirements listed above, it turns out that we can conveniently express the function for any value of x as the real part of the quantity implied by equation 7.5 above:

$$f\left(x'\right) = \mathrm{Re}\left\{\frac{1}{2} + \frac{x'\sqrt{\left(1-x'^2\right)} + \arcsin(x')}{\pi}\right\} \tag{7.6}$$

with

$$x' = \begin{cases} \frac{x}{\beta_a} & \text{for} \quad x < 0 \\ \frac{x}{\beta_b} & \text{for} \quad 0 \leq x \end{cases} \tag{7.7}$$

where the introduction of x' serves to normalize our x-interval to the distances in equations 7.3 and 7.4 above. The function in equations 7.6 and 7.7 is shown in figure 7.6 for at chosen set of parameters with $\tau = g/2$.

The value should decrease from unity towards the far right, as the angle relative to source normal increases. However, as the size of the design is much smaller than the size of the flux source, this effect is negligible within our window of relevance.

7.4 Aperture size α

Turning our attention to a stencil with an aperture, this merely resembles stencils approaching from both sides, thus giving rise to the tapering mentioned above at either edge. With a large aperture size α (figure 7.7a), the flux approaches the nominal value in the middle of the aperture, far away from either edge. If the aperture becomes sufficiently small ($\alpha < 2\beta_b$), the two broadening regions of size β_b can no longer be contained inside the aperture, with the result that the flux no longer reaches the full nominal value anywhere (figure 7.7b).

The introduction of the aperture size, α also introduces restrictions on the quantities above. Specifically, the ratio α/τ imposes a limit on the angle of line of sight for the flux. This corresponds to setting upper bound on the effective source size in the two distances:

$$\begin{aligned} \beta_a &\approx \frac{g r_s}{L} \qquad \text{but with} \quad \beta_a \leq \frac{g\alpha}{\tau} \\ \beta_b &\approx \frac{(g+\tau) r_s}{L} \quad \text{but with} \quad \beta_b \leq \frac{\alpha}{2} \end{aligned} \tag{7.8}$$

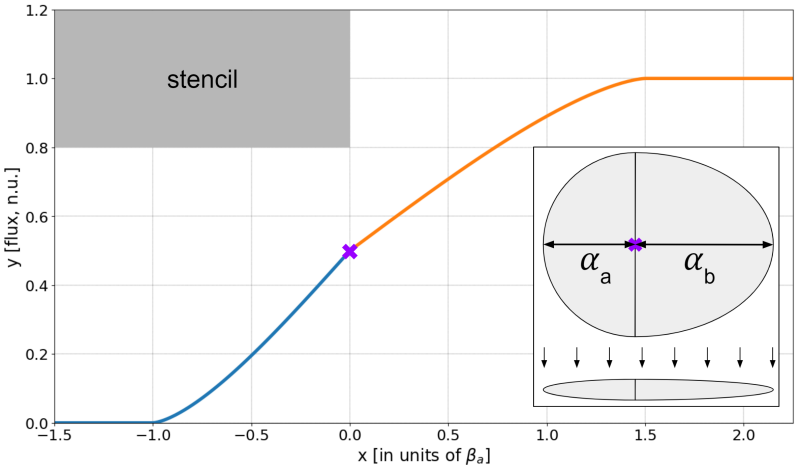

Figure 7.6: **Flux tapering function:** The tapering function in equation 7.6 visualized for a case of $\tau = g/2$. The stencil edge is at $x = 0$ with distance on the x-axis expressed in units of β_a. Insert shows the "circle" for integration with the right hand side "stretched" to accomodate $\beta_b = 1.5\beta_a$ in accordance with $\tau = g/2$ along with equations 7.3 and 7.4.

This merely means evaluating the two quantities in the first line of equation 7.8, with β_a assuming the lower of the two values. Then repeating the procedure for the second line to find β_b, where the limitation states that the broadening on the inside of the aperture can be no larger than half the aperture size. The full length of the broadening region in each side is then given as $\beta_a + \beta_b$.

7.5 Angled deposition pattern changes

Now, allowing for an angled deposition (non-normal incidence), we initially notice two discrepancies between the apertures in the stencil and the pattern left on the substrate (see figure 7.8b): the backside of the pattern on the substrate (right side in aforementioned panel) is shifted in the in-plane direction of the beam by the distance Δs. Similarly, the frontside of the pattern is shifted by the distance $(\Delta s + \Delta\alpha)$:

$$\Delta s = g \tan(\theta) \tag{7.9a}$$
$$\Delta\alpha = \tau \tan(\theta) \tag{7.9b}$$

Consequently, the pattern deposited on the substrate is shorter in length than the aperture itself, specifically shortened by an amount denoted as $\Delta\alpha$. This reduction in length scales with the stencil thickness τ, while the shift in position scales with the gap g.

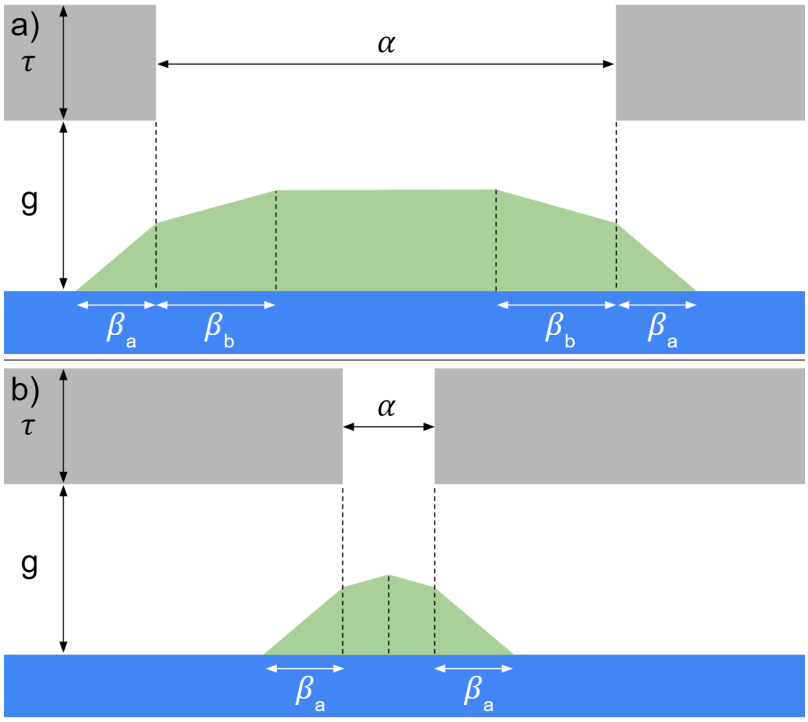

Figure 7.7: **Flux tapering in aperture:** Stencil (grey) with an aperture in the middle, tapering function sketched in green originating from either side. The sloped regions are subject to partial shadowing from the stencil edges.

7.6 Angled deposition broadening

When the deposition is angled, θ now denotes the angle between source-normal and stencil-normal (substrate and stencil are always assumed parallel). The distance L is now measured along the source-normal, which is consistent with the previous section. Measuring the stencil-normal distance to the center of the source will then yield $L\cos(\theta)$, rather than L[5].

Again, starting from a stencil covering the left side but not the right side, figure 7.9a shows a schematic of our setup for rotations $\theta \geq \arctan(r_s/L)$[6]. Again, $x = 0$ is aligned with the stencil edge (purple cross in figure 7.9a). We can trace the angled line from the vertex at the top of the stencil extending

[5]The primary reason for our choice in measurement is the typical constellation of flux sources in high or ultra-high vacuum deposition systems. This way, the flux sources can be thought of as positioned on a hemisphere, with the angular positions being variable but the radius of the hemisphere being fixed.

[6]For smaller rotations, the cutoff may be defined by the stencil bottom rather than the stencil top in figure 7.9. This is a more or less uninteresting special case, and for our system parameters, the rotation angle required amounts to $\theta \geq 1.91°$. The rotation is drawn rather large in figure 7.9, owing to the lever arm L not being drawn to scale.

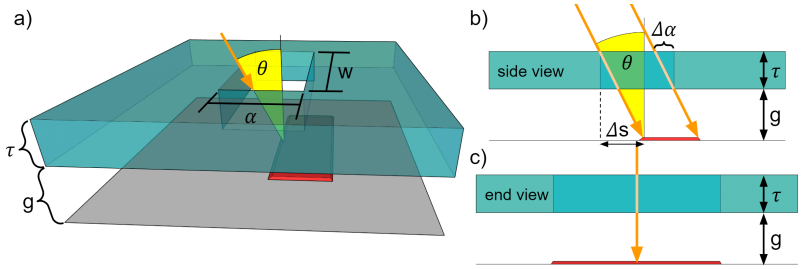

Figure 7.8: **Pattern changes for angled depositions: a)** Overview of stencil (teal) and substrate (grey) with beam direction indicated by an orange arrow. Note the mask thickness τ, mask-substrate-gap g, and incidence angle θ measured relative to substrate normal. A red patch of material is shown as deposited onto the substrate. **b)-c)** Side and end view of the same simple aperture system. Note the horizontal shift from aperture to deposition area and position on the substrate in the side view.

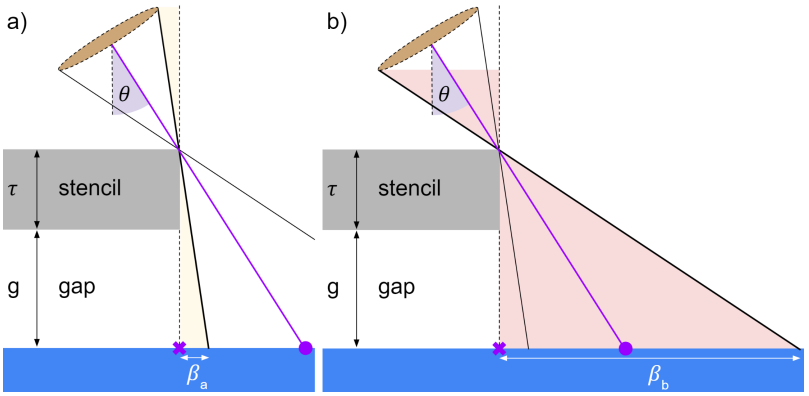

Figure 7.9: **Flux broadening at stencil frontside: a)** β_a is the distance from $x = 0$ to the furthest point on the open substrate, where the flux is still fully shadowed by the stencil. **b)** β_b is the distance from $x = 0$ to the furthest point on the open substrate where flux is still partially impaired by the stencil. Note that the angle θ is drawn quite wide due to the lever arm L not being drawn to scale.

to the substrate.[7] This leaves us with the point of half flux (purple circle in figures 7.9b and 7.9c):

$$x_{\text{half,front}} = (g + \tau)\sin(\theta) \tag{7.10}$$

which reduces to our initial condition for normal incidence at $\theta = 0$.

The lower limit on θ means that the flux no longer creeps below the stencil which is extending from the left side. Instead, part of the otherwise

[7] Any point is approximately aligned with the center of the source, by the same logic as in the previous section.

exposed substrate is still shadowed by the stencil as seen in figure 7.9a. We identify the importance of the leftmost and rightmost points on the source, and their coordinates are found as follows. The coordinates of the leftmost and rightmost points on the source before rotation by angle θ (see figure 7.5a) are simply $\vec{s}_l \approx (-r_s, L)$ and $\vec{s}_r \approx (r_s, L)$, where we have again used the approximation for L in equation 7.2. We can rotate each of our coordinates counterclockwise by the angle θ about the point $(x, y) = (0, 0)$ with the rotation matrix:

$$M_\theta = \begin{bmatrix} \cos(\theta) & -\sin(\theta) \\ \sin(\theta) & \cos(\theta) \end{bmatrix} \tag{7.11}$$

which gives us easy access to the two sets of coordinates after rotation of the source by the angle θ:

$$\begin{aligned} \vec{s}_{l,\theta} = M_\theta \vec{s}_l &= \begin{bmatrix} \cos(\theta) & -\sin(\theta) \\ \sin(\theta) & \cos(\theta) \end{bmatrix} \begin{bmatrix} -r_s \\ L \end{bmatrix} \\ &= \begin{bmatrix} -r_s\cos(\theta) - L\sin(\theta) \\ -r_s\sin(\theta) + L\cos(\theta) \end{bmatrix} \end{aligned} \tag{7.12}$$

and similarly:

$$\begin{aligned} \vec{s}_{r,\theta} = M_\theta \vec{s}_r &= \begin{bmatrix} \cos(\theta) & -\sin(\theta) \\ \sin(\theta) & \cos(\theta) \end{bmatrix} \begin{bmatrix} r_s \\ L \end{bmatrix} \\ &= \begin{bmatrix} r_s\cos(\theta) - L\sin(\theta) \\ r_s\sin(\theta) + L\cos(\theta) \end{bmatrix} \end{aligned} \tag{7.13}$$

From the similar triangles formed in figures 7.9a and 7.9b, we express the distances β_a and β_b in the case of angled depositions:

$$\beta_{a,\text{front}} \approx (g + \tau) \cdot \left| \frac{r_s\cos(\theta) - L\sin(\theta)}{r_s\sin(\theta) + L\cos(\theta)} \right| \tag{7.14}$$

$$\beta_{b,\text{front}} \approx (g + \tau) \cdot \left| \frac{-r_s\cos(\theta) - L\sin(\theta)}{-r_s\sin(\theta) + L\cos(\theta)} \right| \tag{7.15}$$

$$\left|\beta_{\text{front}}\right| = \beta_{b,\text{front}} - \beta_{a,\text{front}} \tag{7.16}$$

We find that $\beta_{a,\text{front}} \leq \beta_{b,\text{front}}$, and due to the angle θ, there is a region from $x = 0$ to $x = \beta_a$, not directly covered by the stencil, which still receives no direct flux from the source (figure 7.9a). Similarly, due to the angle, the shadowing from the stencil reaches farther into the otherwise open area to the point $x = \beta_b$. The "front" subscript is a reminder that this treats the frontside case where the flux impacts first, with the backside case being a stencil covering the right side as follows:

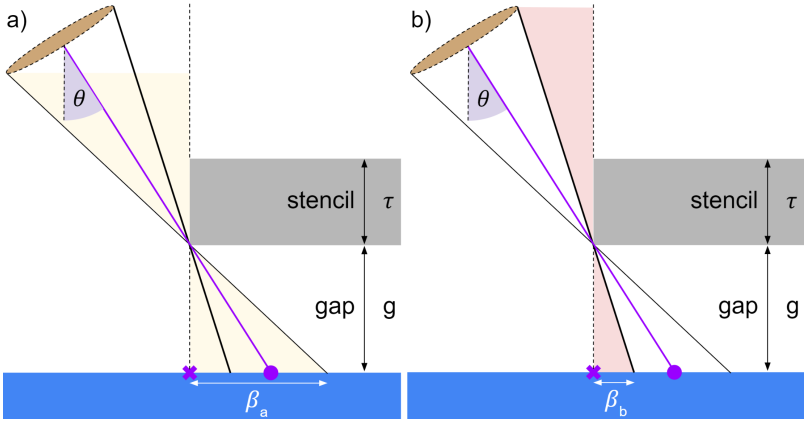

Figure 7.10: **Flux broadening at stencil backside: a)** β_a is the distance from $x = 0$ to the furthest point under the stencil, where the flux is still partially impinging. **b)** β_b is the distance from $x = 0$ to the furthest point under the stencil, where the flux is still nominal and fully unimpaired by the stencil.

If a stencil covers right side instead of the left, the problem is sketched in figure 7.10 instead. Again, we can trace the line to the point of half flux:

$$x_{\text{half,back}} = g\sin(\theta) \tag{7.17}$$

From considerations of similar triangles in figures 7.10a and 7.10b we find:

$$\beta_{a,\text{back}} \approx g \cdot \left| \frac{-r_s\cos(\theta) - L\sin(\theta)}{-r_s\sin(\theta) + L\cos(\theta)} \right| \tag{7.18}$$

$$\beta_{b,\text{back}} \approx g \cdot \left| \frac{r_s\cos(\theta) - L\sin(\theta)}{r_s\sin(\theta) + L\cos(\theta)} \right| \tag{7.19}$$

$$\left|\beta_{\text{back}}\right| = \beta_{a,\text{back}} - \beta_{b,\text{back}} \tag{7.20}$$

We find that $\beta_{b,\text{back}} \leq \beta_{a,\text{back}}$. From comparison of equations 7.16 and 7.20 we find the simple relationship which just expresses that the frontside and backside fluxes are effectively cut off by the top and bottom of the stencil, respectively:

$$\frac{\left|\beta_{\text{front}}\right|}{\left|\beta_{\text{back}}\right|} = \frac{g+\tau}{g} = \left(1 + \frac{\tau}{g}\right) \tag{7.21}$$

In the case of angled deposition through an aperture of size α, the four broadenings are given by equations 7.14, 7.15, 7.18, and 7.19 with the limitations from the aperture as in the previous section:

$$\beta_{a,\text{front}} \leq \beta_{b,\text{front}} \leq \frac{(g+\tau)\,\alpha}{\tau}$$
$$\beta_{b,\text{back}} \leq \beta_{a,\text{back}} \leq \frac{g\alpha}{\tau} \tag{7.22}$$

This establishes a basis of geometric considerations for depositions through stencils. In the following section we will expand on these ideas with the introduction of a novel method for stencil shadowing, exploring additional parameters which appear as a result.

8

Flux filtering stencils

Patent application number PCT/EP2023/066474 covering the techniques described in this chapter was filed on June 19th 2023.

8.1 Introduction to flux filtering stencils

Several lateral patterning techniques have played pivotal roles in advancing quantum device fabrication to its current state. Organic and oxide-based lithographic resist masks have been extensively employed for selective growth or etching processes. Additionally, they have been integral to the widely used *lift-off* technique (see part II), where undesired portions of a deposition layer are removed in a final stripping and cleaning step. These techniques have a long-standing history of success in the large-scale fabrication of conventional electronics and have thus proven their reliability. However, the limitations of these masking techniques are becoming increasingly evident, as the quality bottleneck for quantum devices is progressively shifting towards the aspects of purity and cleanliness at all stages of fabrication and operation[142, 143]. The resist agents utilized in the lithographic process present a unique challenge, as even trace amounts of these agents or residual roughness left behind by stripping and cleaning procedures can significantly degrade the quality of quantum devices. In some cases this becomes the bottleneck for device fidelity. The next significant leap in materials synthesis and fabrication may entail eliminating the need for these resist materials entirely while maintaining precise control over lateral patterning at the highest level. This next step requires significant improvements upon the existing stencil methods for reasons outlined in the previous chapter 7.

Conventional stencil techniques comprise a single pattern for deposition of a material onto a substrate, and additional materials in different patterns will have to be deposited by removal of the original stencil, realignment of a new stencil with the substrate and subsequent deposition. This usually entails breaking the UHV conditions for stencil dismounting and remounting, which degrades the purity of the growth. It also entails a substantial effort in realignment between deposited patterns and subsequent stencils. The default stencil technique employs conventional selectivity; all materials pass through the stencil in a similar and unhindered fashion, and the stencil apertures thus define where materials land during deposition.

The flux filtering stencil technique relies on the use of a robust stencil mask with arrays of nano-apertures separated by a series of parallel "bridges". Note that the bridges envisioned here are equidistantly placed in parallel, contrary to e.g. the rendition in figure 8.1b. The series of bridges serve a dual purpose: firstly, they provide mechanical stability to the mask, particularly across larger apertures and near stencils with extended cantilever type parts which are otherwise susceptible to bending and breaking[139]. This also lifts the topological restraints mentioned

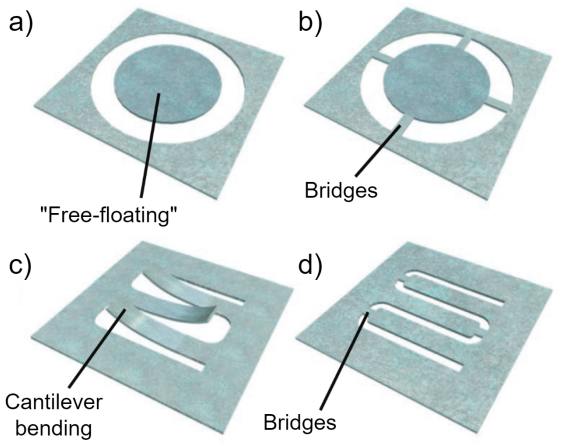

Figure 8.1: **Ring and cantilever stability:** The addition of stabilizer bridges lifts topological restraints and increases stability for e.g. cantilevers which are otherwise susceptible to bending. Top and bottom row show a ring and resonator type design, respectively. Bridges are added, keeping loose stencil parts fixed to surrounding structure. Figure adapted from ref. [139].

back in section 7, which carries important applications for i.e. the superconducting and photonic qubit platforms, as "ground plane"[1] features are now possible due to the otherwise "free-floating" parts now being connected by bridges (figure 8.1b). Secondly, they act as barriers, shadowing particles from the deposition beam from reaching the substrate, whenever their trajectories are misaligned relative to the aperture orientation. This is due to a finite stencil thickness, τ, with a typical size of a few μm. We start from an examination of an array of stencil apertures, each with the same characteristic width w and separated from one another by bridges of width b (figure 8.2).

8.2 Stabilizer bridges

The addition of stabilizer bridges[2] brings about the new parameters w and b, the width of apertures and width of stabilizer bridges, respectively (see figure 8.2a). Other parameters remain unchanged with respect to

[1] Ground planes are large conducting planes surrounding regions with other defined design elements. In a default stencil approach, the connected plane would require a "closed loop" stencil topology akin to that in figure 8.1a with the inside design element being defined in the "free-floating" part.

[2] The schematic in figure 8.2 shows a rectangular design element being divided into sections by bridges. The simple rectangular shape is chosen for simplicity and for illustrative purposes, but a similar procedure would be applicable to more intricate design elements.

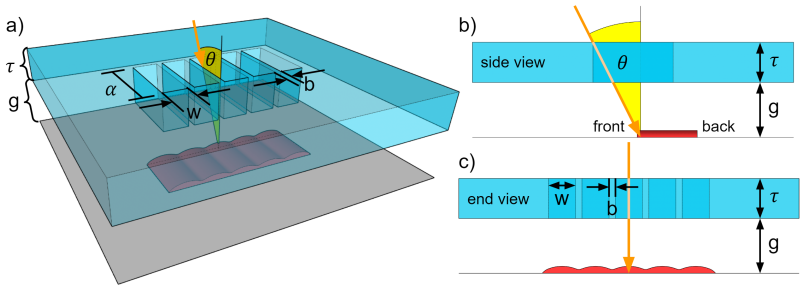

Figure 8.2: **Orientation of stabilizer bridges:** The addition of stabilizer bridges adds the new parameters b and w. Note that the angle of incidence θ lies in a plane parallel with the bridges; the bridges are oriented along the in-plane direction of the beam, ϕ.

the previous chapter. Note that the bridges are aligned with the in-plane direction of the beam[3], which we will label ϕ.

The side view (figure 8.2b) corresponds to the case presented in figures 7.7 and 7.9, and the frontside and backside broadenings will follow the same expressions as derived in section 7.6 before the addition of stabilizer bridges: in terms of the frontside and backside broadening lengths, each aperture acts as the single aperture we examined earlier.

In the end view (figure 8.2c) we note that the "absence" of the angle of incidence, as the viewing angle is parallel with the in-plane direction of the beam ϕ and with the direction of the stabilizer bridges. Thus, the case is directly analogous to the situation in section 7.4 with broadenings given by equation 7.8 – but with aperture size w instead, and the distance to the beam source having a trigonometric coefficient: $\alpha \to w$ and $L \to L\cos(\theta)$:

$$\begin{aligned} \beta_a &\approx \frac{g r_s}{L\cos(\theta)} \quad \text{but with} \quad \beta_a \leq \frac{g w}{\tau} \\ \beta_b &\approx \frac{(g+\tau) r_s}{L\cos(\theta)} \quad \text{but with} \quad \beta_b \leq \frac{w}{2} \end{aligned} \tag{8.1}$$

The broadening in equation 8.1 allows flux to directly impinge underneath stabilizer bridges, allowing for a continuous flux distribution; we can add stabilizer bridges, and still have continuous flux underneath. In order to ensure direct impingement of flux directly underneath each stabilizer bridge, we will obviously require $\beta_a > b/2$. This merely ensures a continuous flux, but not uniformity. The details of the flux distribution are now more involved than what was derived back in section 7.3, since the effective source size will often be restricted due to a limited aperture width w (equation 8.1), and the flux tapering functions from equation 7.6 cannot generally be assumed to apply. This will prompt us to turn to

[3]The in-plane direction of the beam is merely the projection of the trajectory vector (orange arrow, figure 8.2) onto the stencil or substrate surface.

more involved simulations of the flux based on stencil aperture designs and flux beam input parameters later in this chapter. The key point is that the broadening (called "blurring" back in section 7) scales with the gap g, and sufficient broadening lets us introduce stabilizer bridges without flux discontinuities.

8.3 Flux blocking from in-plane misalignment

With the addition of stabilizer bridges, the design now has an intended in-plane direction ϕ for the flux beam angle, that is, an intended particle trajectory. The flux beam can be characterized by two angles: the pre-existing incidence angle, where $\theta = 0°$ represents normal incidence, and the newly introduced azimuth in-plane angle ϕ, with an in-plane deviation of $\Delta\phi = 0°$ indicating a direction parallel with the bridges (see also figure 8.7a). While the flux beam is aligned with this in-plane direction, the beam will pass through the aperture array as intended[4]. If the in-plane direction of the beam is changed, $\Delta\phi > 0$, at some point the beam will be unable to pass through the apertures due to θ picking up an increasing component in the end view (orange arrow off-vertical in figure 8.2c). We will label this component $\theta_\perp$ since it exists in the plane perpendicular to ϕ. For similar reasons we will label the component in the side view (figure 8.2b) $\theta_\parallel$, since it exists in a plane parallel with ϕ.

We can derive the critical angle for flux blocking from figure 8.3 as follows. Let $\boldsymbol{v} = (v_x, v_y, v_z)$ be the beam vector after misalignment by rotation around the z-axis by the amount $\Delta\phi$. This leaves the angle θ relative to the z-axis unchanged. First, by projection onto the xy-plane we find that:

$$v_y = v_x / \tan\left(\Delta\phi\right) \tag{8.2}$$

and that the z-component of $\mathbf{v}$ can be expressed as:

$$v_z = \frac{\sqrt{v_x^2 + v_y^2}}{\tan\left(\theta\right)} \tag{8.3}$$

where the numerator is just the length of the projection of $\boldsymbol{v}$ onto the xy-plane. Substituting equation 8.2 into equation 8.3 leaves us with the expression:

$$\begin{aligned} v_z &= \sqrt{v_x^2 + \left(\frac{v_x}{\tan\left(\Delta\phi\right)}\right)^2} \Big/ \tan\left(\theta\right) \\ &= v_x \sqrt{1 + \cot^2\left(\Delta\phi\right)} \Big/ \tan\left(\theta\right) \end{aligned} \tag{8.4}$$

[4] Passage also requires a certain ratio of other parameters: $\tan(\theta) < \alpha/\tau$, we will however assume for this to be the case, in part due to our ability to compensate for $\Delta\alpha$ from equation 7.9, which will also be described in more detail in the following chapter 9.

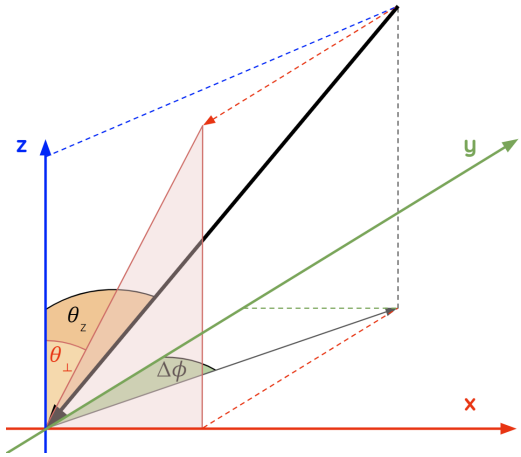

Figure 8.3: **Perpendicular angle component:** The beam vector (solid black) is originally aligned with the y-axis (and ϕ), but is then misaligned by rotation about the z-axis in the clockwise direction by the amount $\Delta\phi$. This gives the beam vector non-zero component $\theta_\perp$ in the zx-plane or end view.

and now from projection of $\boldsymbol{v}$ onto the zx-plane instead we find:

$$\tan(\theta_\perp) = v_x / v_z \tag{8.5}$$

Substituting equation 8.4 into equation 8.5 yields:

$$\begin{aligned} \tan(\theta_\perp) &= \frac{\tan(\theta)}{\sqrt{1+\cot^2(\Delta\phi)}} \\ &= \frac{\tan(\theta)}{|\csc(\Delta\phi)|} \end{aligned} \tag{8.6}$$

or equivalently

$$\theta_\perp = \arctan\left(\frac{\tan(\theta)}{\sqrt{1+\cot^2(\Delta\phi)}}\right) = \arctan\left(\frac{\tan(\theta)}{|\csc(\Delta\phi)|}\right) \tag{8.7}$$

Expressing the maximum perpendicular angle, at which the beam is still able to pass through the apertures (end view, figure 8.2c):

$$\theta_\perp^* = \arctan\left(\frac{w}{\tau}\right) \tag{8.8}$$

and setting equation 8.7 (square root expression) equal to equation 8.8 directly leads to the critical deviation angle at which the beam is fully blocked by the flux filtering apertures:

$$\Delta\phi^* = \arctan\left(\left[\left(\frac{\tau}{w}\right)^2 \tan^2(\theta) - 1\right]^{-1/2}\right) \tag{8.9}$$

It is worth noting the physical limitation $\Delta\phi \leq 90°$ since misalignment beyond 90° merely results in an increased alignment with the anti-parallel direction. Consequently, equation 8.9 yields imaginary values for $\Delta\phi^*$ for parameter combinations that would render full blocking by misalignment impossible, specifically when $w > \tau \tan(\theta)$. Notice the direct implication of equation 8.9: flux filtering stencils allow selectivity based on particle direction, i.e. position of the beam source relative to ϕ, the orientation of the bridges.

The same type of derivation can be made for the "parallel" component $\theta_\parallel$ for evaluation of how much the "effective" θ measured parallel with the bridges (side view, figure 8.2b) changes due to misalignment in ϕ, leading to an expression more or less similar with equation 8.6:

$$\begin{aligned}\tan\left(\theta_\parallel\right) &= \frac{\tan\left(\theta\right)}{\sqrt{1+\tan^2\left(\Delta\phi\right)}} \\ &= \frac{\tan\left(\theta_z\right)}{\left|\sec\left(\Delta\phi\right)\right|}\end{aligned} \tag{8.10}$$

For approximation purposes, we expand both expressions in $\Delta\phi$:

$$\begin{aligned}\theta_\perp &= \arctan\left(\frac{\tan(\theta)}{\sqrt{1+\cot^2(\Delta\phi)}}\right) \\ &= \Delta\phi\tan(\theta_z) - \Delta\phi^3\left(\frac{\tan(\theta)+2\tan^3(\theta)}{6}\right) + O\left(\Delta\phi^5\right)\end{aligned} \tag{8.11}$$

$$\begin{aligned}\theta_\parallel &= \arctan\left(\frac{\tan(\theta)}{\sqrt{1+\tan^2(\Delta\phi)}}\right) \\ &= \theta_z - \Delta\phi^2\left(\frac{\sin(2\theta)}{4}\right) + O\left(\Delta\phi^4\right)\end{aligned} \tag{8.12}$$

showing the perpendicular component $\theta_\perp$ with an approximately linear dependence with $\tan(\theta)$ coefficient, and and approximately constant value for the parallel component $\theta_\parallel$ at small $\Delta\phi$. For an incidence angle $\theta = 40°$ (see fig. 8.4) we find that the linear approximation for $\theta_\perp$ (equation 8.11 up to first order in $\Delta\phi$) is accurate to within one quarter degree for $\Delta\phi < 13.71°$, and the constant approximation for $\theta_\parallel$ (equation 8.12 constant term) is accurate to within one quarter degree for $\Delta\phi < 7.76°$.

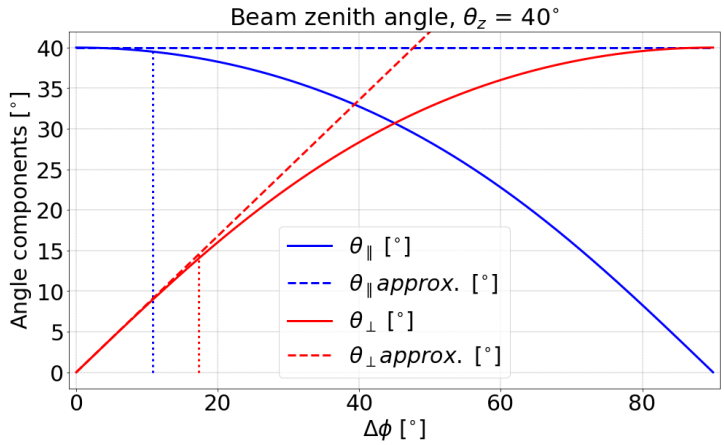

Figure 8.4: **Angle approximations:** The components in the side and end view and their approximations from equations 8.12 and 8.11 for $\theta = 40°$. The vertical dotted lines indicate when the approximations deviate from the accurate expressions by one quarter degree.

Equation 8.9 provides the means to calculate when the beam is blocked due to misalignment relative to the intended in-plane direction. This characteristic transforms the nano-apertures into flux filters for depositions that are misoriented relative to one another. This relative misorientation can be conveniently achieved by rotating the entire substrate-stencil system. Furthermore, if the deposition scheme necessitates blocking the beam at a specific critical angle $\Delta\phi^*$ then the critical aperture width is given by:

$$w^* = \frac{\tau \tan(\theta)}{\sqrt{1+\cot^2(\Delta\phi^*)}} = \frac{\tau \tan(\theta)}{|\csc(\Delta\phi^*)|} \tag{8.13}$$

Equation 8.9 facilitates planning based on a given aperture width w, providing the "misalignment" required to maintain independent depositions. Conversely, equation 8.13 enables planning based on a given critical angle $\Delta\phi^*$ establishing an upper limit on the aperture width permissible in the stencil design. This will prove particularly useful if i.e. the positions of the beam sources are "locked" in place, and rotation of the substrate-stencil system is undesirable or difficult.

Finally, isolating the stencil thickness τ instead might come in handy for analysis based on intentionally misaligned depositions. If the aperture width w is known for a series of aperture arrays with increasing misalignments, then one should be able to determine $\Delta\phi$ within a certain range and thus derive a stencil thickness:

$$\tau = \frac{w\sqrt{1+\cot^2\left(\Delta\phi^*\right)}}{\tan(\theta)} \tag{8.14}$$

This is the method used in ref. [P4] for estimating the thickness of stencils made from pre-fabricated membranes with a large thickness standard deviation. We will get around to an example of this in section 8.5 below.

8.4 Number of deposition angles

Equation 8.9 establishes the relationship between mask dimensions w and τ and the beam angles θ and $\Delta\phi^*$. A fundamental feature of the flux filtering stencil approach is the potential for multiple independent depositions from a single stencil. Once the parameters mentioned above are chosen for a particular deposition i, we can consider the angle associated with the i'th deposition $(\phi_i \pm \Delta\phi_i^*)$ as occupied. There is one additional correction that also holds significance: due to the finite size of the beam source, there is an inherent spread in the angles θ and $\Delta\phi$ that describe the beam vector angle. Therefore, when planning for multiple independent depositions based on equations 8.9 and 8.13, one must evaluate θ and $\Delta\phi$ from the most conservative values. In a first approach, this uncertainty can be approximated as $\sigma \approx \arctan(r_s/L) \approx 1.9°$. Moving forward, we will assume that any issues related to beam angle uncertainty and finite source size have been appropriately addressed.

In the special case where all depositions for a given substrate are designed with the same critical deviation angle $\Delta\phi^*$, we can straightforwardly deduce the number of deposition directions available:

$$n_{dep} = \left\lfloor \frac{180°}{\Delta\phi^*} \right\rfloor \tag{8.15}$$

where the "floor brackets" denote rounding down to nearest integer.

A general visualization illustrating the number of possible in-plane deposition angles based on equations 8.9 and 8.15 is presented in figure 8.5. This visualization includes an angle uncertainty of 5° directly added to $\Delta\phi^*$ before applying equation 8.15. It is important to note that for scenarios such as $(\tau/w) = 40$ and $\theta_z = 40°$, where the critical misalignment angle from equation 8.9 is as small as $\Delta\phi^* \approx 1.7°$, the angle tolerance of 5° is responsible for the majority of angle occupation. However, in practical engineering terms, an uncertainty in beam angle control on the same order as or larger than $\Delta\phi^*$ would lead to highly inconsistent experimental results. This extreme case is more theoretical and less sensible for fabrication purposes.

Figure 8.5 demonstrates that it is quite feasible to achieve a high number of independent deposition directions, at least from the perspective of angle independence. This is attainable as long as the lithography and etching processes allow for stencil apertures with narrow widths compared

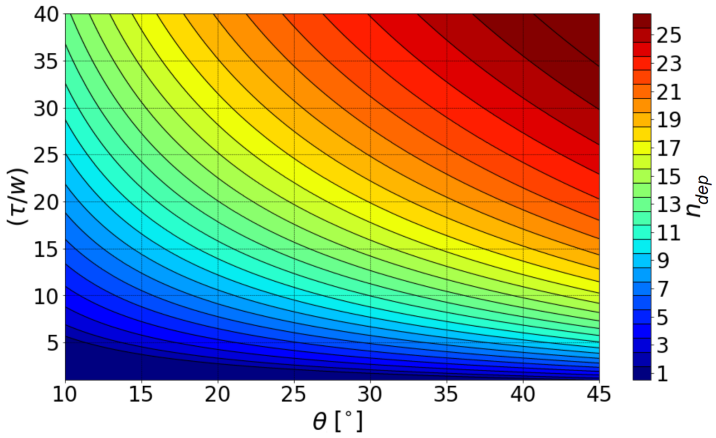

Figure 8.5: **Number of independent depositions:** The number of independent angles is a function of the parameters chosen for each deposition. Assuming the same incidence angle θ and characteristic aperture width w for all depositions, the number of independent depositions n_{dep} can be evaluated.

to the stencil thickness. As demonstrated in ref. [P4], a ratio of $(\tau/w) \approx 40$ is easily within realistic bounds from a lithography and etching standpoint ($\tau \approx 2\mu$m, $w \approx 500$nm).

While it is clear from equation 8.15 that a small value for $\Delta\phi^*$ is desirable to accommodate many depositions within one stencil, it is important to recognize that a small $\Delta\phi^*$ also imposes stricter requirements for deposition angle control, increasing the impact of small angle deviations on the flux distribution. A better approach might be to plan for a certain number of depositions and calculate the bounds on θ and w^* using equation 8.13, allowing a higher tolerance by a higher critical misalignment angle, $\Delta\phi^*$.

8.5 Flux simulation results

The analytical examinations in chapter 7 provide a good vantage point for understanding flux distributions. However, the analytical approach becomes less attractive with increasing design complexity, and more generally applicable ways of examining flux distributions are warranted. To this end, I constructed a three-dimensional model which includes the substrate, stencil, and beam source[5]. I sampled the flux incident at set positions on the substrate as a fraction of the beam source visible through the stencil apertures from that particular point. While this approach assumed a uniform circular source, it is worth noting that other source types could be treated as a series of sources with varying partial fluxes. For instance, a

[5]The flux simulation setup is described in more detail in section 9.2.

α	w_s	w_a	b	τ
2μm	2μm	500nm	100nm	2μm
g	r_s	L	θ	$\Delta\phi$
5μm	1cm	30cm	30°	0°

Table 8.1: Default values for geometric parameters used in flux simulations. The s and a subscripts denote simple aperture model and array aperture model, respectively.

source with circular symmetry could be modeled as a series of concentric rings, each contributing to the overall beam flux. This modeling approach enabled me to generate maps of the flux distribution across a chosen substrate region. Additionally, by sampling a line of points on the substrate, I was able to obtain line scans that would correlate with the amount of material deposited in the hit-and-stick mode (including no crystal growth related effects). For a parameter examination, a set of *default values* were chosen, displayed in table 8.1, where the deviation from default applies solely to the parameter under examination in each simulation series.

The results for a simple rectangular aperture are shown in figure 8.6 along with a schematic of the setup. Line scans are taken in side view from figure 7.8b, along ϕ, the in-plane direction of the beam. Thus, the broadenings of the profiles conceptually correspond to those in figures 7.9 and 7.10. Figure 8.6b here shows the impact of a variation in the gap parameter, where the direct scaling of both the frontside and backside broadenings with g is readily apparent. We also note asymmetry, in that the frontside broadening region is generally wider than the backside region, as predicted from equation 7.21. As expected, this broadening asymmetry is more pronounced for lower gap values where $(g+\tau)/g$ is noticeably larger than unity. The increasing displacements Δs (equation 7.9b) have been omitted for easier comparison.

Figure 8.6c shows variation in the stencil thickness τ. The broadening asymmetry is most notable for larger thicknesses, and the width of the exposed substrate region is substantially shortened with larger $\Delta\alpha$ (see equation 7.9a). For the default values, a stencil thickness of $\tau^* \approx 3464$nm corresponds to $\Delta\alpha = 2000$nm, and thus the flux should fully vanish for stencil thicknesses of $\tau > 3.5\mu$m and above due to restrictions on the incidence angle from the aperture length α.

Finally, figure 8.6d primarily shows three effects of increasing incidence angle θ. First, the shortening of the flux region $\Delta\alpha \propto \tan(\theta)$ leads to the flux almost disappearing at $\theta = 45°$, where the $\Delta\alpha(\theta = 45°) = \tau$, and the remaining flux is caused by spread in beam angles[6]. Second, the

[6]When the beam source center has an incidence angle of $\theta = 45°$, some part of the beam source will still have an lower incidence angle due to the finite size of the source. For our default parameters, we estimated this spread in angles at $\sigma \approx 1.9°$ back in section 8.4.

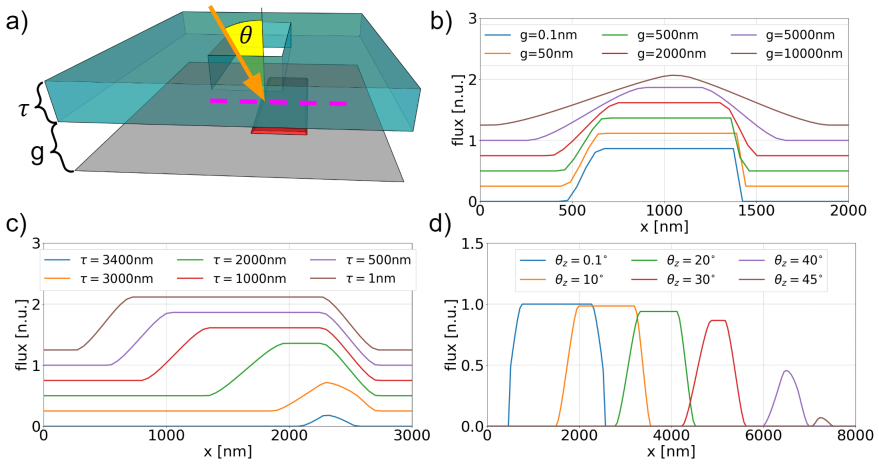

Figure 8.6: **Simple aperture model flux: a)** Schematic for flux simulations, dimensional parameters in table 8.1. Dashed magenta line on the substrate shows direction for flux line scan in following panels. **b)-d)** Simulated flux line scans for variations of the listed parameters. Other *default* values are found in table 8.1. Note the difference in axes between panels.

backside of the flux region on the substrate is shifted by Δs (equation 7.9b). At $\theta = 45°$, this shift should be $\Delta s(\theta = 45°) = g = 5\mu$m, which matches well with the result from simulation. Third, the overall flux now has a coefficient of $\cos(\theta)$ due to the same beam flux being spread over a larger area. Additionally, for the larger vales of θ, the flux no longer reaches the "full value" due to the aperture length α effectively limiting the source size as seen from any given point on the substrate.

Flux simulations for aperture arrays

Moving on to the flux simulations for aperture arrays, the setup is now shown in figure 8.7a. Note the two angles θ (yellow) and $\Delta\phi$ (green), and the new dimensional parameters w and b for width of apertures and width of stabilizer bridges, respectively, introduced back in section 8.2.

For these flux simulations, I constructed a 3-dimensional model[7] of an array with five parallel apertures, each with a width of w and separated by bridges of width b. As usual, the in-plane direction of the beam aligns with the orientation of the bridges. Our main interest is now the flux distribution as we scan across the array of apertures and bridges (dashed magenta line in figure 8.7a), that is, in the end view from the overview back in figure 8.2c, perpendicular to the in-plane direction of the beam, ϕ.

Starting with the variation in the gap parameter g in figure 8.7b, we observe that the flux profile becomes discontinuous for small gap values,

[7] The flux simulation setup is described in more detail in section 9.2.

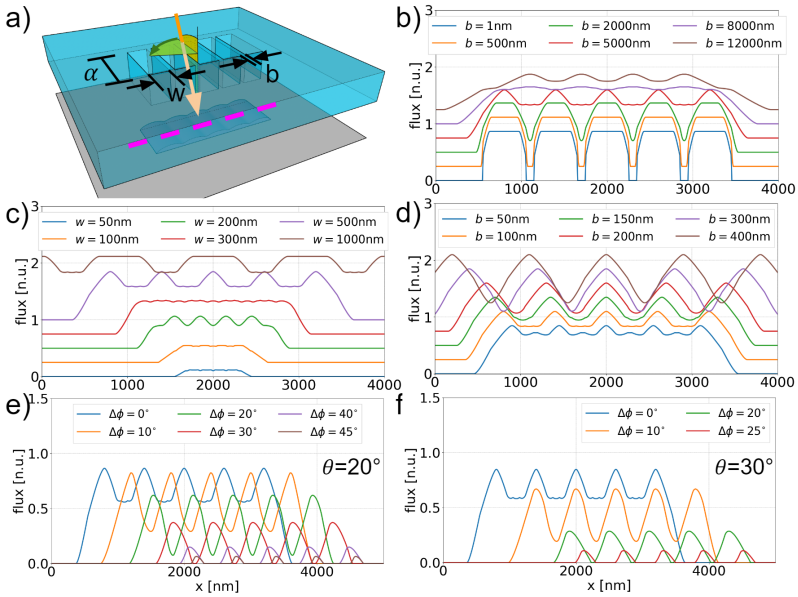

Figure 8.7: **Aperture array model flux: a)** Schematic for flux simulations, dimensional parameters in table 8.1. Dashed magenta line on the substrate shows direction for flux line scan in following panels. Angle marked in yellow is the incidence angle θ. Angle marked in green is the misalignment angle $\Delta\phi$, which is zero except for in the last two panels. **b)-d)** Simulated flux line scans for variations of the listed dimensional parameters. Vertical offset of 0.25 [n.u.] used for clarity. **e)-f)** Simulated flux line scans for variations in misalignment $\Delta\phi$ for two different values of the incidence angle θ. Note the different axis for the last two panels.

and the broadening regions are quite narrow. Referring back to equation 7.3, it is evident that broadening scales with the gap, and for small gaps, the broadening distance w_b is insufficient to cover the flux gaps in regions situated directly beneath the bridges. It is clear that the gap parameter predominantly controls the broadening, and once the gap reaches a sufficiently large value (approximately $g \geq 1\mu$m), a continuous albeit non-uniform flux is established underneath our aperture array. As such, a certain gap g is needed. While broadening facilitates the deposition of a continuous film, it also leads to the overall widening of feature outlines, potentially introducing undesirable artifacts, particularly for quantum applications. We will address this concern in chapter 10. For $g = 12\mu$m we see the phenomenon "flux inversion": the regions directly underneath each bridge receive more direct flux than regions directly underneath apertures. This seemingly counter-intuitive phenomenon occurs when "the sum of two broadenings" yields a higher flux than positions directly underneath an aperture that sufficiently restricts the effective source size.

Note also that the overall flux decreases with increasing gap, as this limits the effective source size: the same aperture appears smaller when viewed at a greater distance.

Shifting our attention to the aperture width w, we immediately observe that very narrow apertures significantly restrict the flux distribution, resulting in substantial variations in the flux maxima. Notably, certain parameter sets (e.g., $w = 200$nm) again lead to "flux inversion". The high degree of uniformity observed for $w = 300$nm is also noteworthy, suggesting the possibility of depositing a very smooth and uniform layer beneath an aperture array, even with bridges as wide as $b = 100$nm. The degree of uniformity displayed here depends on the interplay of various model parameters, and establishing a general condition for maximizing uniformity would require further analysis than what has been conducted here.

Lastly, for the width of the bridges parameter b in figure 8.7e, we observe the effects of variations in this parameter. Narrow bridges result in a more uniform flux distribution, as they block less of the total flux. As the bridges widen, the minima in the flux distribution become deeper, as wider bridges obstruct a larger portion of the flux beneath them. In the case of sufficiently wide bridges, points directly beneath them receive zero flux:

$$b \geq 2\beta_a \tag{8.16}$$

For our default parameters, equation 8.16 is satisfied when $b \geq 333.3$nm, with β_a evaluated using equation 7.3 as discussed previously. It is important to note that while the flux minima in figure 8.7e vary with the parameter b, the maxima remain constant and independent of b within the range of parameter values examined.

In-plane misalignment

The final two panels (figure 8.7e and 8.7f) show the results of in-plane misalignment ($\Delta\phi \neq 0$) for two different incidence angles, θ. From equation 8.9 it is obvious, that a higher incidence angle should "magnify" the impact of misalignment, which is also supported by the results here. We see that the initial in-plane misalignment causes a lowering of the flux minima, akin to the results for increasing bridge width b. A shift of the entire pattern is also noticeable, as the pattern shift Δs (section 7.5) picks up a component in the horizontal direction due to the rotation of the beam angle (see figure 8.7a). This shift is more noticeable for the higher incidence angle, θ, as we would expect from equation 8.7. Increasing the in-plane misalignment impacts both the flux minima and maxima, which corresponds to the bridges having a wider cross section when viewed at an angle, and the apertures thus appearing more narrow. This tendency eventually leads to full blocking of the beam source. We note that the default values (table 8.1) with equation 8.9 gives critical deviation angles of

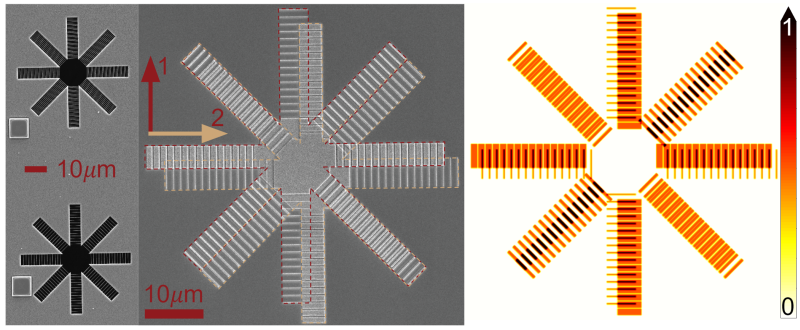

Figure 8.8: **Flower design overview:** Left panel shows an SEM image of the stencil with two different types of flower design, differing in the parameter values for w and b. Some interference effects are present. Middle panel shows an SEM image of the pattern left on the substrate after two sequential depositions following the arrows shown, for the flower pattern with $w = 1100$nm and $b = 150$nm at $\theta = 25°$. Dashed outlines added for clarity. Right panel shows the flux simulation for the same two depositions at $\theta = 25°$, $\tau = 2\mu$m and $g = 2\mu$m. The middle patch was omitted from simulations. *Stencil fabrication, deposition and SEM image credit: Michaela Eichinger.*

$\Delta\phi^*(\theta = 20°) = 43.38°$ and $\Delta\phi^*(\theta = 30°) = 25.66°$. The persistent appearance of flux in figure 8.7e even at $\Delta\phi = 45°$ is caused by the finite source size: even though the perpendicular angle is greater than the maximum allowed when measured towards the center of the source, some trajectories are still open from other parts of the beam source. This is caused by the beam angle spread from section 8.4, $\sigma \approx 1.9°$.

Comparison with experiment

The initial proof of concept for flux filtering stencils demonstrates that the flux incident on the substrate closely matches the results from simulations. To this end, we constructed a few different designs with series of aperture arrays for different geometric parameters, and increasingly misaligned relative to each other. The first type of design had aperture arrays laid out in a "flower" style, with different parameters for w and b, and misalignment increasing in steps of 45°. Figure 8.8 shows the stencil for such a design (left), the pattern left after after two sequential depositions through that same stencil (in-plane directions of depositions along arrows in middle panel), as well as the simulations of said depositions (right). Stencil fabrication and deposition details are available in ref. [144].

We first remark, that the combination of parameters and the relatively shallow incidence angle $\theta = 25°$ means that the beam should never be fully blocked by in-plane misalignment. From equation 8.13 we find $w^* \approx 932.6$nm, and our apertures of $w = 1100$nm should thus allow some

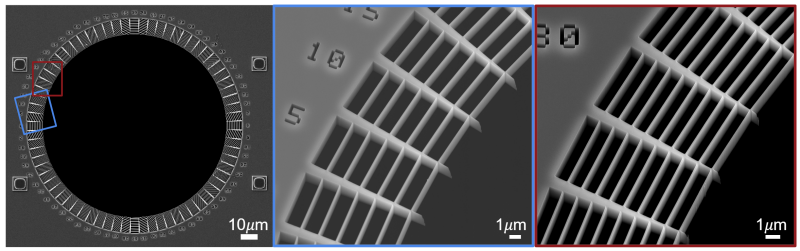

Figure 8.9: **Circle design overview:** SEM images with overview of circle pattern with apertures arrays laid out around the perimeter. Some interference effects are present. Boxes show zoom regions. Middle and right panels are zooms from two different circle pattern on the same stencil, differing in parameters w and b. *Stencil fabrication and SEM image credit: Michaela Eichinger.*

flux to pass through regardless of in-plane misalignment. Indeed this seems to be the case, as the entire pattern appears in two different iterations. Now, from a quick by-eye comparison between the deposition SEM and simulation in figure 8.8 we note that both patterns are shifted more in the in-plane direction than expected: the first deposition (red outline) is further north, and the second deposition (sand outline) is further east, than in the simulation, both by about 1 to 1.5μm. Settling at an estimate of 1.25μm, from equation 7.9a we find that this corresponds to a difference of $\Delta g = 1250\text{nm}\cot(25°) \approx 2860\text{nm}$ from the planned value, i.e. an actual gap in experiment of $g \approx 5\mu$m. More rigorous gap analyses protocols should be implemented part of future optimizations, but this seems unnecessary here, as the stencil mounting and deposition procedure was very rudimentary (see details in ref. [144]) due to the proof of concept nature of the experiment.

Another type of pattern included for characteristics had the aperture arrays laid out along the perimeter of a large circle, with the misalignment increasing in steps of 5°. Several iterations were included with different combinations of w and b parameters. Figure 8.9 shows such a pattern on a stencil, along with zoom on two regions for a detailed view. We remark that the two zoom regions shown are from two different "flower" patterns, differing in parameters w and b. Notice the sharp definition and high aspect ratio etch achieved by Michaela Eichinger by fine tuning of the CORE dry etch technique developed by Nguyen et al.[145, 146]. Description of the CORE etch technique can be found in refs. [145, 146], and details for the fabrication of these particular stencils in ref. [144].

Figure 8.10 top panel is an SEM image of the pattern left on the substrate after deposition, with the bottom panel being the corresponding flux simulation. Note the difference in $\Delta\phi^*$, with the simulation showing a completely blocked flux for arrays misaligned by $\Delta\phi = 25°$ or more ($\Delta\phi^* = 20.95^*$), while the AFM scan shows some material still impinging

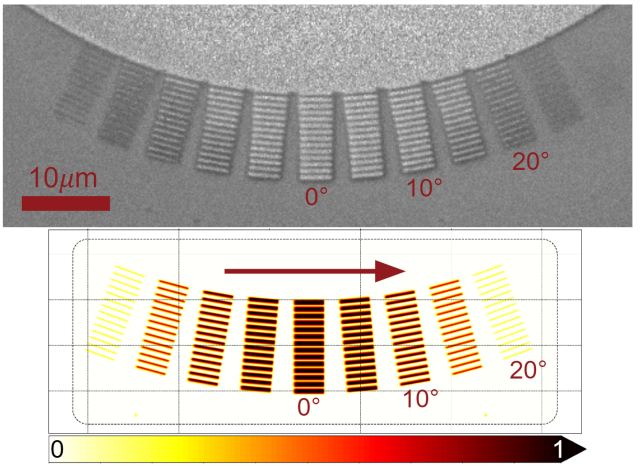

Figure 8.10: **Circle design comparison: Top)** SEM image of pattern deposited through a stencil design included for characteristics. Arrow shows direction of deposition. Aperture arrays are increasingly misaligned in intervals of 5° with parameters $w = 600$nm, $b = 150$nm. **Bottom)** Simulation of the same design with $\theta = 40°$ and $\tau = 2\mu$m. *Stencil fabrication, deposition and SEM image credit: Michaela Eichinger.*

on the substrate for arrays misaligned by $\Delta\phi = 25°$. The critical misalignment angle derived from the experimental result, $\Delta\phi^*$ in the range of 25° to 30°, allows us to estimate the stencil thickness from equation 8.14 of τ somewhere in the range of 1430nm to 1690nm. This is in reasonable agreement with the prefabricated base membranes used in these experiments, with specifications of $\tau = 2\mu$m with a tolerance of ±20%.

The discrepancies described in section 7.5 can all be counteracted with rule-based design adaptation, and automation of this type of procedure allows scaling to larger and much more complex designs, while ensuring consistency and reproducibility. The next chapter is therefore a much more practical walk through the transition from substrate design to stencil design, as well as the setup used for the flux simulations shown so far.

We remark that the flux broadening remains a concern at this point. Even assuming we can control the gap (which is not trivial, but more of a problem on the engineering side), we need a certain gap g and thus broadening to ensure continuous flux underneath stabilizer bridges. At the same time, we need to limit the broadening for sharp definitions at feature outlines. We will address this issue with another novelty in chapter 10.

9

Additional stencil considerations

The successful utilization of flux filtering stencils for nanoscale depositions hinges on the change in workflow outlined back in section 7.1. This new workflow entails stencil design, intended to produce a certain outcome on the substrate upon deposition. Since the usual workflow involves design for a substrate outcome, part of the change in workflow includes a translation or an adaptation from substrate design to stencil design. The adaptations necessary due to geometry described in section 7.2 can all be automated based on input designs. The first step is thus a set of rules for converting a substrate design into a stencil design – in a first approach, ignoring the broadening β_a partially shadowed by the stencil edge[1].

9.1 Rule-based design adaptation

The discrepancies described in the main text (primarily Δs and $\Delta\alpha$ from equation 7.9) carry a necessity to reverse-engineer a stencil from a substrate design. This process can be automated with a script in order to ensure consistency and increase efficiency, changing the usual process of design, fabrication, characterization and optimization. For this purpose we assume that a certain design has been chosen in advance, each element in a Computer Assisted Design (CAD) file corresponds to an area where material should be deposited into a pattern on the substrate, and each element can be fairly approximated as a polygon with a finite number of vertices.

The design adaptation process is "rule-based" and involves three steps:

1. Shifting elements to counteract Δs from equation 7.9a
2. Adding stabilizer bridges, slicing elements into smaller parts
3. Elongating elements to counteract $\Delta\alpha$ from equation 7.9b

A design can comprise an arbitrary number of elements, each of which ultimately corresponds to a patch of material which is to be deposited onto the substrate. In the conventional design process, this would typically be represented in a CAD file *before* adaptation by a polygon specified as a list containing the coordinates of the vertices. The polygon in our CAD file *after* adaptation should directly represent an aperture in the stencil, through which the particles will pass during deposition, leaving a pattern on the substrate. Our efforts in design adaptation and deposition procedures in some sense boils down to minimizing the discrepancy between the planned design and the pattern left on the substrate after deposition through our adapted stencil design.

Each design element, e.g. our polygon, belongs to a design "layer," which essentially groups elements together. For our purposes, we employ

[1] The main reasons for this approach is convenience, and the fact that we will address the broadening β_a explicitly in the next chapter 10.

layer grouping to indicate elements which share the set of parameters [θ, ϕ, b, w]. This means that elements within the same layer have attributes in common, such as the material, the planned layer thickness, and the deposition angles. In essence, elements belonging to the same layer are meant to be "activated" during the same deposition step. Multiple layers can be designed for activation at the same angles θ and ϕ but still belong to different layers due to distinction in other parameters, e.g. have different dimensions b for bridges and w for apertures in order to achieve distinct flux modulations (see figure 8.7c and 8.7d).

Assuming that the CAD files are read into a Python environment, each element comprises a polygon, represented as a list with positions of vertices. This type of setup is well suited for a 2-dimensional geometry package such as `shapely`[147], which additionally offers fast computing of set operations such as subtractions (`difference`) needed for stabilizer bridges, unions (`unary_union`) desirable for simultaneous operations on large sets of elements, and convex hull calculations (`convex_hull`) which is the workhorse for the later elongation of all convex polygons.

The elongation counteracts the effective aperture shortening $\Delta\alpha$ (equation 7.9b) caused by the mask thickness τ, and should straight forwardly alter all relevant parts of a design for a given deposition. The elongation should be unidirectional, strictly parallel with the in-plane direction of the beam, and should leave other dimensions unchanged, measured in the perpendicular direction, i.e. not merely stretching the polygon. With the relevant elements represented as 2D polygons, we find that some shapes lend themselves quite easily to elongation, while others are less cooperative. For starters we consider a simple case: a part of a substrate design which when viewed from above appears as a convex polygon. Convex polygons notably includes any triangular or parallelogram shapes, any regular n-sided polygons and any reasonable polygonal approximations of circular segments smaller than one half circle or full-circle. It also importantly includes any polygon arising as a result of splitting a convex polygon by a straight line.

If $\mathbb{P}$ denotes the set of vertices of the initial convex polygon, and $\mathbb{Q}$ denotes the same set of vertices displaced by $\Delta\alpha$ in the ϕ direction, then $\mathrm{Conv}(\mathbb{P} \cup \mathbb{Q})$ yields the correctly elongated polygon, that is the convex hull of the union of original and shifted sets of points (see figure 9.1 top row). In a broad range of cases, this is the most straight forward way of calculating the necessary elongation when translating from substrate design to stencil design. However, we also see that the very same scheme fails for the concave shape (figure 9.1 bottom row), where the original shape is not recovered upon elongation followed by shortening.

Closer inspection of a shape which does not do well upon arbitrary elongation, we consider a V-shape where horizontal elongation causes the "valley" to close up and eventually become a trapezoid (figure 9.2 top row). Deposition back through our trapezoidal aperture would return a

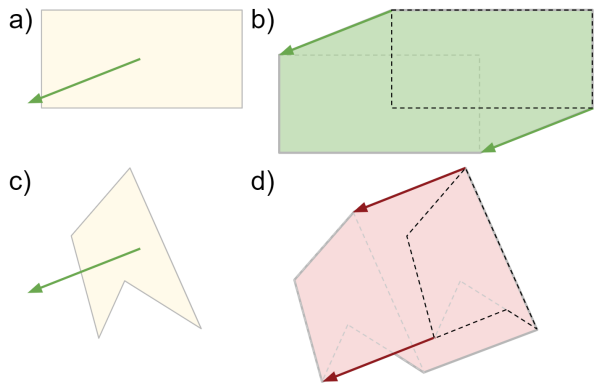

Figure 9.1: **Elongation of convex and concave polygons: a)** Simple rectangular (convex) element to be deposited on substrate. Green arrow shows direction and magnitude of elongation needed to counteract $\Delta\alpha$. **b)** Elongation of rectangular element. Two dashed outlines show $\mathbb{P}$ and $\mathbb{Q}$, respectively. Green shading shows Conv($\mathbb{P} \cup \mathbb{Q}$). Black dashed outline shows pattern after directional shortening by $\Delta\alpha$, expected with deposition through aperture in green. **c)** Concave element to be deposited on substrate. **d)** Dashed grey outlines show $\mathbb{P}$ and $\mathbb{Q}$, with Conv($\mathbb{P} \cup \mathbb{Q}$) shaded in red. Black dashed outline shows pattern after directional shortening by $\Delta\alpha$, expected with deposition through aperture in red. Note the distortion of the pattern compared to the original element.

trapezoidal pattern on the substrate – but not the original V-shape; an inverse-elongation procedure does not yield the original V-shaped input. Keeping our V-shape example, we also note that if we were elongate vertically, the elongation and shortening procedure does yield the original V-shape back (figure 9.2 bottom row). As such, the success or failure of our procedure depends both on the input polygon and on the elongation direction. From considerations of the original V-shape, we see that horizontal elongation changes the distance between vertices in directions other than only horizontal. We state loosely and without proof a criterion for elongation: correct elongation is only possible along directions for which the distance between all vertices measured is constant in the direction perpendicular to the elongation when measured before and after elongation; distances may only change measured in the direction parallel with the elongation. In terms of deposition design, this means that some additional planning is warranted whenever one wishes to incorporate concave elements.

Elongation algorithm for concave polygons

For the elongation procedure in case of concave polygons, we treat each polygon as a series of vertices with the line segments between them defin-

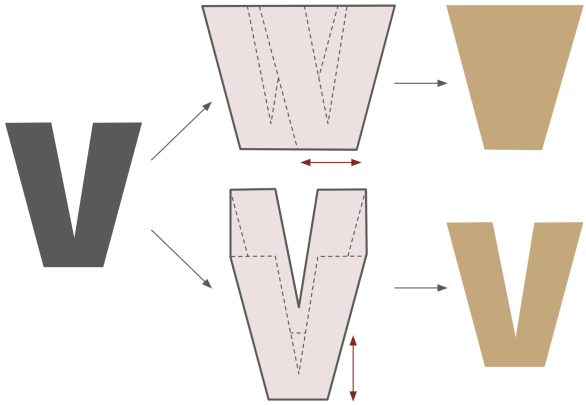

Figure 9.2: **Elongation directions: Top row)** Initial V-shape elongated in the horizontal direction, yielding an aperture where the cavity in the V is lost. Deposition following the elongation direction back through the aperture results in a trapezoid instead of a V-shape. **Bottom row)** Initial V-shape elongated in the vertical direction. Deposition back through the aperture returns the original V-shape.

ing the boundary. For each vertex we need to determine, whether the vertex should be represented by the original point ("keep"), by the version of said vertex shifted by the elongation vector $\overline{u_e}$ ("shift") or by both (see figure 9.3). A vertex which should not be represented in the elongated polygon in either of the two forms would either be a redundant point (not actually a vertex, i.e. a point somewhere on a straight boundary) or constitute a "point concavity", which would mark a breach of the elongation criterion. One example of a point concavity would be the vertex in the "valley" of the V-shape in figure 9.2 top row, which is not represented in the elongated polygon top middle.

Let p_n be one of the original polygon vertices. Let $\overline{u_e}$ be the elongation vector with length $\Delta\alpha$ given in the main text, following the in-plane direction of the beam ϕ. Let $\overline{v_e}$ be an infinitesimal version of $\overline{u_e}$. With

$$p_n^{\pm} = p_n \pm \overline{v_e} \tag{9.1}$$

we can classify the vertex p_n according to the relationship between p_n^+, p_n^- and the original polygon set $\mathbb{P}$ (compare with figure 9.3):

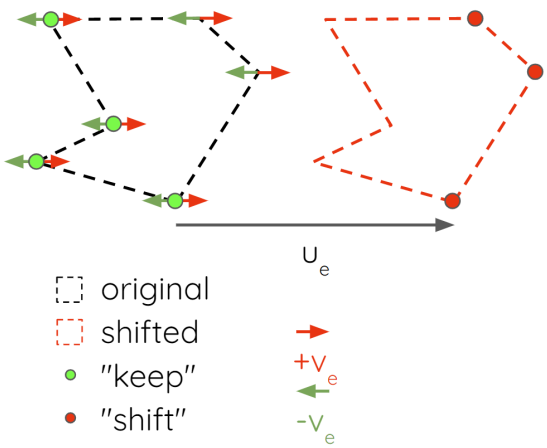

Figure 9.3: **Vertex classification:** The original and "shifted" polygons are shown along with the elongation vector $\overline{u_e}$ of length $\Delta\alpha$. The final shifts will pertain to certain vertices in order to achieve polygon elongation. Note that this is distinctly different from the shifts mentioned in the main text. The vectors $\pm\overline{v_e}$ are infinitesimal versions of the elongation vector. The elongated polygon can be constructed from the kept and shifted vertices (green and red circles, respectively). Note that the elongation is "allowed" as it does not violate the elongation criterion.

$$
\begin{aligned}
p_n^- \notin \mathbb{P} &\Rightarrow p_n\text{: "keep"} \\
p_n^+ \notin \mathbb{P} &\Rightarrow p_n\text{: "shift"} \\
\left(p_n^- \in \partial\mathbb{P}\right) \wedge \left(p_n^+ \in \mathbb{P}^o\right) &\Rightarrow p_n\text{: "keep"} \\
\left(p_n^- \in \mathbb{P}^o\right) \wedge \left(p_n^+ \in \partial\mathbb{P}\right) &\Rightarrow p_n\text{: "shift"} \\
\left(p_n^- \in \partial\mathbb{P}\right) \wedge \left(p_n^+ \in \partial\mathbb{P}\right) &\Rightarrow p_n\text{: "redundant"} \\
\left(p_n^- \in \mathbb{P}^o\right) \wedge \left(p_n^+ \in \mathbb{P}^o\right) &\Rightarrow p_n\text{: "concavity"}
\end{aligned}
\tag{9.2}
$$

where $\partial\mathbb{P}$ and $\mathbb{P}^o$ denote the boundary and the inner of $\mathbb{P}$, respectively. The first two conditions in equation 9.2 can hold true simultaneously for a given point p_n, leading to this point being represented by both the "keep" and "shift" versions. We emphasize that the "shift" here regards shifting the position of individual vertices in order to elongate a polygon, and that this is strictly different from the shifting of entire aperture positions, Δs, in equation 7.9a.

The type of evaluations in equation 9.2 can also be carried out with `shapely`[147] (e.g. using `covered_by` and `within`). While the classification of vertices could be done in a manner different from the one described in equation 9.2 above, this one is aimed as reducing redundancy in vertices (eliminating unnecessary vertices) and covers the possible combinations

for $p_n^{\pm}$. Construction of the elongated polygon now requires classifying an ordered list of the polygon vertices, then iterating over the ordered and classified list, adding to a new list of vertices either p_n in the case of "keep" or $(p_n + \overline{u_e})$ in the case of "shift". In the case of "both", the order of addition of vertices is determined by the classification of the neighboring vertices. Any "redundant" points can be discarded outright, as they were unnecessary to begin with[2]. The "concavity" type should not arise unless the elongation criterion is violated. Note that the definition in equation 9.2 "detects" violations of the criterion even if the relevant vertex does not disappear outright. The resulting new list is now an ordered list of the vertices for the elongated polygon.

Figure 9.4 shows the process from original design through rule-based design adaptation and simulation of resulting flux at depositions. The first step (not shown) is shifting of the pattern by the distance Δs due west, in the direction opposite of the beam direction. This will only matter if the absolute position matters, i.e. if several layers are being aligned relative to one another, or if the deposition is aligned relative to an alignment mark on the stencil – but should be included for consistency. The second step is dividing our circle into smaller pieces by subtracting a set of appropriately oriented stabilizer bridges. For our choice of parameters $w = 300$nm and $b = 100$nm, this leaves us with a circle cut into six separate polygons (figure 9.4b). The act of dividing a convex polygon by a straight line will always result in exactly two convex polygons. Meanwhile, the act of dividing a concave polygon may yield an arbitrary number of polygons, which may be convex or concave. Practically speaking, this will help contain the problematic vertices (those classified as "concavity" by equation 9.2 above) to smaller polygons[3], often leaving most of the resulting polygons as concave and easily treatable. With luck, some concave polygons may reduce to convex polygons, making for an easier procedure. We remark that the appearance of multiple polygons is a nice opportunity for `multiprocessing` (readily available Python package), as the polygons can be treated as fully independent, and speedups of a factor 5x or more are easily achievable[4]. Of course, for a realistic design, multiple polygons would probably be present before division, regardless. The next step is elongation, where convex polygons are treated by the Conv($\mathbb{P} \cup \mathbb{Q}$)

[2] The term "redundant" here refers to a vertex on an otherwise straight line, such that removing said vertex leaves the polygon unchanged. It is the technical detail separating a convex polygon from a "strictly convex" polygon; a strictly convex polygon contains no redundant vertices.

[3] Specifically, if a polygon was to be split by a straight line through a "concavity" vertex along an allowed elongation direction (i.e. vertically through the vertex in the bottom of the valley of the V-shape in figure 9.2), this would remove the vertex concavity all together. However, this would be of little benefit, as the elongation along this direction was possible to begin with, as described in section 9.1.

[4] The speedup depends on the number of cores and threads available, and some overhead is associated with distributing the workload, opening and closing processes etc. However, multiprocessing speedups of somewhere in the range of 5x to 20x are very realistic.

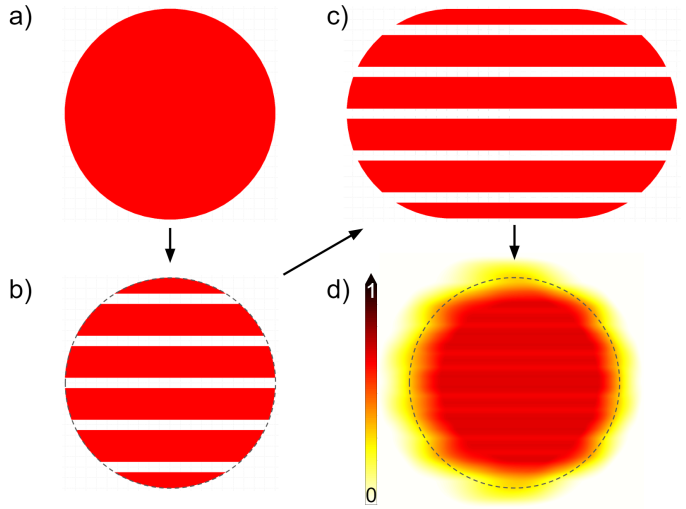

Figure 9.4: **Rule-based design adaptation: a)** Our intended design is a simple circle of radius $r = 1\mu$m, in this case approximated as a regular 64-sided polygon. In-plane shift to counteract Δs not shown. **b)** The intended deposition direction is from west to east, which determines the horizontal alignment of our bridges. Inspired by the results in figure 8.7c, we choose parameters $w = 300$nm and $b = 100$nm, expecting a more or less uniform flux of around two thirds of the nominal value. This leaves us with six apertures instead of our original circular one. **c)** Each of our six original polygons are elongated in the horizontal direction. Since each is a convex hull, we elongate by the "easy" convex hull procedure described in section 9.1. Parameters are $\theta = 30°$, $\tau = 2\mu$m. **d)** Simulation of deposition through a stencil with apertures from our adapted design with $g = 5\mu$m and the same set of parameters as we used for elongation. Dashed outline shows intended target area.

procedure mentioned above. Concave polygons resulting from division (necessarily from division of an initially concave polygon) are treated with the procedure in section 9.1. The result after elongation (figure 9.4c) is written to a design file, which can be read by CAD software. Finally, we conduct a check by simulating the flux on the substrate from our resulting set of apertures. The result is shown in figure 9.4d, along with a dashed outline showing the intended shape. We remark, that the shape in the original design is always highly idealized, as it pertains to the conceptual stage from back in section 1.2.

9.2 Flux point evaluation

The main area of interest is the pattern deposited on the substrate, and simulations of the flux arriving on to the substrate should prove highly use-

ful for both static and time-dependent growth simulations. For instance, flux simulations directly allow visualization of the broadening mentioned in the main text in the case where the incoming atoms behave in a hit-and-stick manner. Simulations also serve as a check; after reverse engineering our stencil, we now wish to evaluate the results expected from deposition through this.

In the special case where the source can be approximated as uniform and the material distribution is approximately isotropic, the relative flux directly impinging on a point on the substrate is directly proportional to the relative total source area visible from this point. We are neglecting differences in intensity due to distance to the source, since the distance to the source will be approximately constant across the exposed substrate. Thus, for any given point on the substrate and a given apertures, it is sufficient to evaluate the "intersection" of the apertures at the stencil bottom, at the stencil top, and the source as seen from the substrate point. Since the stencil top and stencil bottom are situated in two different parallel planes, a straight forward intersection would yield the empty set, thus the quotation marks. The intersection should be carried out for these sets relative to the substrate point in question and in one common plane. This can be determined by "point-projection" onto the plane of the stencil bottom[5] as shown in figure 9.5.

Now working in the plane of the stencil bottom and referencing the right side in figure 9.5: let $\mathbb{B}_n$ be the set of points enclosed by the bottom aperture n (grey rectangle). Let $\mathbb{T}_n$ be the set of points enclosed by point-projection of aperture n from the top of the stencil to the bottom (red rectangle). Let $\mathbb{S}$ be the set of points enclosed by point-projection of the source onto the stencil bottom (green circle). Note that both $\mathbb{T}_n$ and $\mathbb{S}$ are implicitly functions of our choice of substrate point. We can now evaluate the total relative flux at a given substrate point:

$$\begin{aligned} \frac{J}{J_{max}} &= \text{area}\Big(\mathbb{S} \cap \bigcup_n \big(\mathbb{B}_n \cap \mathbb{T}_n\big)\Big) \Big/ \text{area}\,(\mathbb{S}) \\ &= \sum_n \text{area}\Big(\mathbb{S} \cap \big(\mathbb{B}_n \cap \mathbb{T}_n\big)\Big) \Big/ \text{area}\,(\mathbb{S}) \end{aligned} \tag{9.3}$$

where area($\mathbb{A}$) denotes evaluating the area of the set $\mathbb{A}$, and the "big cup", $\bigcup_n$ denotes a union across all n apertures. Note that the union is taken after each term is evaluated separately: for a particle to pass, it must pass through the stencil top and bottom for the same aperture n. We remark that for realistic system dimension we often find $\mathbb{S}$, the

[5] Working in the plane of the stencil bottom will cause issues, if one wishes to examine a hard contact stencil, $g = 0$, as all point projections will vanish into the substrate point. It is chosen here for efficiency (one less plane for which to do point projections of every polygon for every substrate point sampled) and for explanatory purposes. In a real implementation, the working plane could favorably be chosen at a set distance independent of the system parameters.

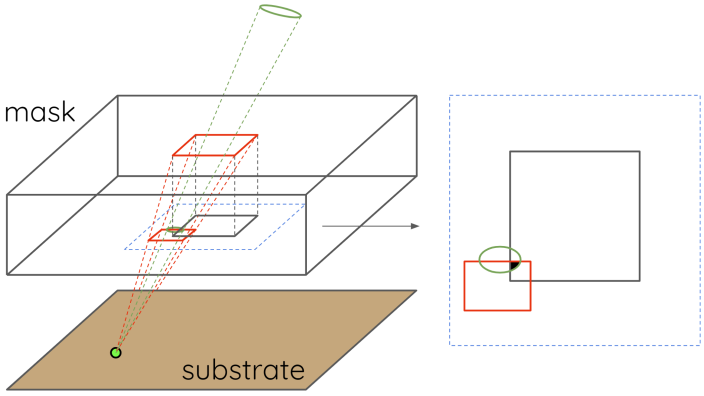

Figure 9.5: **Point projection for flux evaluation:** for the point on the substrate marked in bright green. **Left:** Stencil top aperture (red) and circular beam source (green) point-projected onto the plane of the stencil bottom. **Right:** Top-down view of the part enclosed by the border in dashed light blue. Evaluating the area of the intersection shaded in black relative to the area of the point projection of the beam source (green ellipsis) yields the relative flux at the chosen point on the substrate.

point projection of the source polygon onto the plane of the bottom of the stencil, to appear as very small compared to the set $\bigcup_n (\mathbb{B}_n \cap \mathbb{T}_n)$, and for a given substrate point some restrictions may be applied to selection of relevant apertures n for increased computational efficiency – often, many apertures in the design will be too far away from a given substrate point to carry any relevance. The fact that point projection and evaluation of equation 9.3 is carried out for each substrate point sampled, calls for `multiprocessing` for several substrate points in parallel, with significant speedups as a result.

Film thickness

As mentioned back in the early chapters 2, control of the flux is in some sense on the input side, with the output being a function of the kinetics and thermodynamics as well. A complete description of how the crystal growth related effects will interact with the flux distribution and the end result of this is unfeasible. We can however make a short remark on the effect of film thickness deposited, from the thermodynamics described back in chapter 2.

Our simulations of the flux distribution represents a statistical average; in an actual growth experiment, the distribution of the deposited material will be stochastic instead. As such, there will be areas with higher and lower flux than predicted. On top of this, the material will attempt to minimize

the free energy while growing, leading to the effects discussed back in chapter 2. The thermodynamics may cause the growing film to form islands near feature outlines where only partial flux impinges. One direct way to address parasitic islands caused by partial flux is through control of the film thickness deposited. Once an unwanted island is formed near a defined feature, additional material may be deposited. The additional material added onto and near the cluster will cause growth size both laterally and out of plane. The aspect ratio is given by the thermodynamic conditions which result in a specific contact angle. Sufficient film thickness will thus cause the islands in the broadening region to coalesce with the film, comprising a continuous layer. The thickness necessary depends on the energy considerations above, and the relationship between the film thickness and the lateral flux broadening thickness β_a, discussed back in section 7.2. If the conditions would a cluster to assume contact angle θ_{contact} with the substrate (see figure 5.2), then the cluster will be forced to coalesce with the main film if the height of the cluster h_{cluster} fulfills the condition:

$$h_{\text{cluster}} \geq \frac{\beta_a}{2} \tan(\theta_{\text{contact}}) \tag{9.4}$$

which is directly controllable by the amount of material deposited. The details of the coalescence will depend on the thermodynamic conditions; diffusion is needed both in order to have a well defined cluster morphology and for reconfiguration of the overall morphology upon coalescence. The resulting film will display a characteristic broadening length somewhere between that defined geometrically by the flux broadening β_b and the one determined by thermodynamics. An additional note in favor of thick film deposition (a few hundred nm) is a recent study which suggests that the film thickness has a high impact on i.e. superconducting Al circuits due to the ability to reduce oxide near the substrate-film interface[148].

As a final experimental note, we add that the growing morphology will create conditions different from the flat substrate that we assumed as a starting point; the initial flat substrate does not stay flat for long. Thus, the flux distribution during growth will become a function of the existing morphology as well as the original system geometry. This could for instance cause self-shadowing of growing structures, especially at low temperature and high incidence angles θ. This could in part be addressed by choosing incidence angles with a specific relation to the contact angle θ_{contact}:

$$0^\circ < \theta < 90^\circ - \theta_{\text{contact}} \tag{9.5}$$

which should eliminate self-shadowing effects for islands with morphology controlled by thermodynamics. Note that equation 9.5 reflects the fact that self-shadowing is inevitable for contact angles above 90°, regardless of incidence angle.

9.3 Potential III/V stencil growth

Growth of III/V semiconductors is fairly well studied, but still challenging for a number of reasons. As alluded to earlier in chapter 3, the Selective Area Growth method is often used for these compounds. The use of stencils is challenging for a number of reasons, one of those reasons being tied to the topological constraints mentioned earlier. The typical growth conditions for III/V involve high temperature and a high group V overpressure for surface stability, and a "normal" stencil will tend to block passage of the necessary group V beam.

With the stabilizer bridges introduced in chapter 8, we can use the central part of a stencil to define the pattern in question, leaving this part suspended in an elongated mesh or grid of stabilizer bridges, allowing the necessary flux to pass. If we further exploit the flux filtering feature of the stencils, we might choose the orientation of the apertures, such that the group V species is allowed maximum passage, keeping the passage of the group III species as our mode of selectivity. The basic idea is to orient our substrate normal towards the group V source, which for fixed beam sources will position the group III source at a given incidence angle θ. Subsequent rotation of the entire substrate-stencil system around the substrate-normal should allow free adjustment of the in-plane angle ϕ towards the group III source relative to the orientations chosen for the stencil[6]. To this end, we need the angle between the beam sources, which we can calculate from the "default coordinate system" (origo at holder center, z-axis as substrate normal) as follows:

For a given beam source i, we designate the position of the source first by negative rotation about the x-axis by the amount θ_i (leaning towards the positive y-axis), followed by a positive rotation by the amount ϕ_i about the z-axis (counter-clockwise when viewed from the positive z-axis above, towards the negative x-axis). This is consistent with the notation in figure 8.7 from the previous section, with the line scans running in the x-direction, the α parameter measured along the y-axis, and the z-axis as substrate normal. The matrix for negative rotation about x-axis by the amount θ_i is:

$$\begin{aligned} \boldsymbol{M_{\theta_i}} = \boldsymbol{R_x(-\theta_i)} &= \begin{bmatrix} 1 & 0 & 0 \\ 0 & \cos(-\theta_i) & -\sin(-\theta_i) \\ 0 & \sin(-\theta_i) & \cos(-\theta_i) \end{bmatrix} \\ &= \begin{bmatrix} 1 & 0 & 0 \\ 0 & \cos(\theta_i) & \sin(\theta_i) \\ 0 & -\sin(\theta_i) & \cos(\theta_i) \end{bmatrix} \end{aligned} \tag{9.6}$$

and the matrix for positive rotation about z-axis by the amount ϕ_i:

[6] We remark that this method would entail disabling the usual rotation of the substrate holder (figure 2.1), which is commonly used to aid uniformity in flux distribution.

$$\boldsymbol{M_{\phi_i}} = \boldsymbol{R_z(\phi_i)} = \begin{bmatrix} \cos(\phi_i) & -\sin(\phi_i) & 0 \\ \sin(\phi_i) & \cos(\phi_i) & 0 \\ 0 & 0 & 1 \end{bmatrix} \tag{9.7}$$

Gathering the two operations into one matrix, which applies the rotation for θ_i followed by the rotation for ϕ_i:

$$\begin{aligned} \boldsymbol{M_{\theta_i,\phi_i}} &= \boldsymbol{M_{\phi_i}} \times \boldsymbol{M_{\theta_i}} \\ &= \begin{bmatrix} \cos(\phi_i) & -\sin(\phi_i) & 0 \\ \sin(\phi_i) & \cos(\phi_i) & 0 \\ 0 & 0 & 1 \end{bmatrix} \times \begin{bmatrix} 1 & 0 & 0 \\ 0 & \cos(\theta_i) & \sin(\theta_i) \\ 0 & -\sin(\theta_i) & \cos(\theta_i) \end{bmatrix} \\ &= \begin{bmatrix} \cos(\phi_i) & -\cos(\theta_i)\sin(\phi_i) & -\sin(\theta_i)\sin(\phi_i) \\ \sin(\phi_i) & \cos(\theta_i)\cos(\phi_i) & \sin(\theta_i)\cos(\phi_i) \\ 0 & -\sin(\theta_i) & \cos(\theta_i) \end{bmatrix} \end{aligned} \tag{9.8}$$

This allows us to directly generate a vector which, starting from a unit vector pointing in the substrate normal direction $\boldsymbol{v_0} = (0,0,1)$ yields a unit vector pointing towards the beam source i:

$$\begin{aligned} \boldsymbol{v_i} &= \boldsymbol{M_{\theta_i,\phi_i}}\,\boldsymbol{v_0} \\ &= \begin{bmatrix} \cos(\phi_i) & -\cos(\theta_i)\sin(\phi_i) & -\sin(\theta_i)\sin(\phi_i) \\ \sin(\phi_i) & \cos(\theta_i)\cos(\phi_i) & \sin(\theta_i)\cos(\phi_i) \\ 0 & -\sin(\theta_i) & \cos(\theta_i) \end{bmatrix} \begin{bmatrix} 0 \\ 0 \\ 1 \end{bmatrix} \\ &= \begin{bmatrix} -\sin(\theta_i)\sin(\phi_i) \\ \sin(\theta_i)\cos(\phi_i) \\ \cos(\theta_i) \end{bmatrix} \end{aligned} \tag{9.9}$$

This unit vector points directly at the effusion cell for source i. Now, the angle between two arbitrary vectors $\boldsymbol{v_i}$ and $\boldsymbol{v_j}$ can be calculated as:

$$\theta_{i,j} = \arccos\left(\frac{\boldsymbol{v_i}\cdot\boldsymbol{v_j}}{|\boldsymbol{v_i}||\boldsymbol{v_j}|}\right) \tag{9.10}$$

where the denominator vanishes since we constructed our vectors as unit vectors. The "i,j" subscript is chosen, as this is the angle between source i and j. It is the effective incidence angle of the group III species, once the substrate-stencil system is appropriately oriented with normal towards the group V source. Thus, for the angle between our two sources:

$$\theta_{i,j} = \arccos\left(\begin{bmatrix} -\sin(\theta_i)\sin(\phi_i) \\ \sin(\theta_i)\cos(\phi_i) \\ \cos(\theta_i) \end{bmatrix} \cdot \begin{bmatrix} -\sin(\theta_j)\sin(\phi_j) \\ \sin(\theta_j)\cos(\phi_j) \\ \cos(\theta_j) \end{bmatrix}\right) \tag{9.11}$$

We are further free to choose the orientation of our in-plane coordinate system such that $\phi_i = 0$, leaving us with:

$$\begin{aligned}\theta_{i,j} &= \arccos\left(\begin{bmatrix}0\\ \sin(\theta_i)\\ \cos(\theta_i)\end{bmatrix}\cdot\begin{bmatrix}-\sin(\theta_j)\sin(\phi_{i,j})\\ \sin(\theta_j)\cos(\phi_{i,j})\\ \cos(\theta_j)\end{bmatrix}\right)\\ &= \arccos\left[\sin(\theta_i)\sin(\theta_j)\cos(\phi_{i,j}) + \cos(\theta_i)\cos(\theta_j)\right]\\ &= \arccos\left[\sin^2(\theta)\cos(\phi_{i,j}) + \cos^2(\theta)\right] \qquad (9.12)\end{aligned}$$

where $\phi_{i,j}$ is now the difference in in-plane angles between sources i and j[7] (see figure 9.6), and the last line is only valid in the special case where $\theta_i = \theta_j = \theta$, which applies in our case. For our local deposition system with sources placed in a circle above the substrate holder[8] (figure 9.6), each at an incidence angle of $\theta_i = \theta_j \approx 25°$, with the group III and group V sources placed at in-plane angles 135° apart, equation 9.12 gives a value of $\theta_{\text{Ga,As}} \approx 46°$. This value is now the effective incidence angle from the group III (Ga) source, when the substrate is oriented with the normal direction towards the group V (As) source. We will need this value for our stencil adaptations as outlined in the previous sections 9.1. Note also the position of the In source in figure 2.1. It is currently positioned directly across from the Ga source, which prohibits any flux filtering based on in-plane misorientation between In and Ga depositions – for default substrate orientations (flat on the substrate holder). The in-plane direction of the In source is also merely $\phi_{\text{In,As}} = 45°$, which yields quite a shallow incidence angle relative to the As source from equation 9.12 as $\theta_{\text{In,As}} \approx 18.6°$. For the III/V type depositions, we would obtain more freedom for flux filtering if the In source was moved, e.g. to the current position of the Al source (bottom right in figure 9.6). This would position the In and Ga sources at $\phi_{\text{In,Ga}} = 90°$ relative to one another, allowing for easy flux filtering selectivity. It would also position the In source at $\phi_{\text{In,As}} = 135°$ relative to the As source, akin to the current position of the Ga source.

Figure 9.7 shows a conceptual design for a nanowire oriented vertically. The group V source is at normal incidence, so the group V impinges everywhere more or less uniformly. Meanwhile, the group III species is arriving at an incidence angle given by equation 9.12, in our case $\theta \approx 46°$ with an in-plane direction from left to right. As such, the group III species can only pass through the stencil apertures indicated in red. The pattern left on the substrate will be narrowed by the amount $\Delta\alpha$ which we found back in equation 7.9. Due to misalignment flux filtering, no group III particles pass through apertures marked in blue. For the GaAs type deposition

[7] We note from equation 9.12 that we would have obtained a similar result, if we had chosen to orient our coordinate system such that $\phi_j = 0$ instead, as should be the case.

[8] The sources are really placed below the substrate with everything turned upside down, relative to how we have been picturing it so far – but we will stick with our current description to avoid unnecessary confusion.

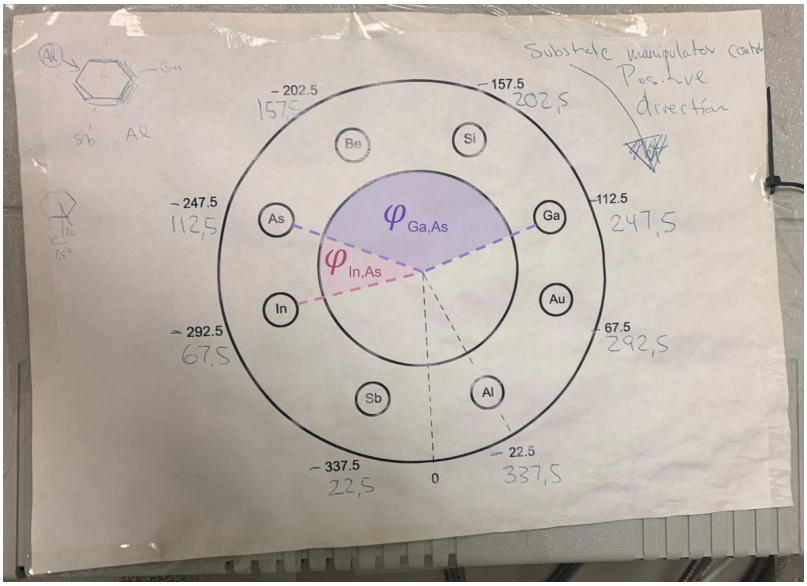

Figure 9.6: **MBE effusion cell layout:** Schematic for our local MBE system, showing the relative positions of effusion cells as projected onto the substrate holder plane. For Ga and As, the relative in-plane angle $\phi_{\mathrm{Ga,As}} = 135°$, while for In and As it is $\phi_{\mathrm{In,As}} = 45°$. The incidence angle is uniform for all effusion cells at $\theta \approx 25°$.

envisioned here, that would limit the width of the apertures for blocking (width of blue apertures in figure 9.7) to approximately the thickness of the stencil: $w^* = \tau \tan(\theta_{\mathrm{Ga,As}})$. For a similar approach with In and As sources, the shallow incidence angle of the In source relative to the As source position $\theta_{\mathrm{In,As}} \approx 18.6°$ would limit the width of blocking apertures to a third of the stencil thickness: $\tan(\theta_{\mathrm{In,As}}) \approx 0.337$.

Note the cross-stabilizers (horizontal) in the blue pattern, added to avoid stabilizer bridges sticking together. Experimental observations revealed that these bridges have a tendency to "bunch up", especially when they are elongated and positioned in close proximity. This phenomenon is exemplified in figure 9.8. Although the underlying cause of this bunching is hypothesized to be Van der Waals forces, a thorough investigation into this has not been conducted. To mitigate this effect, various strategies can be implemented, one of which is the use of cross-stabilizers as illustrated in figure 9.7. It is important to note that for depositions deviating from the normal incidence, each cross-stabilizer casts a distinct shadow, due to its perpendicular orientation relative to the stabilizer bridges, which necessitates consideration in flux simulations. Alternative methods to address this bunching issue are depicted in figure 9.9. On the left, a mechanical solution is presented, where two slightly misaligned sets of stabilizer bridges provide mutual support and fixation. The right side of the figure

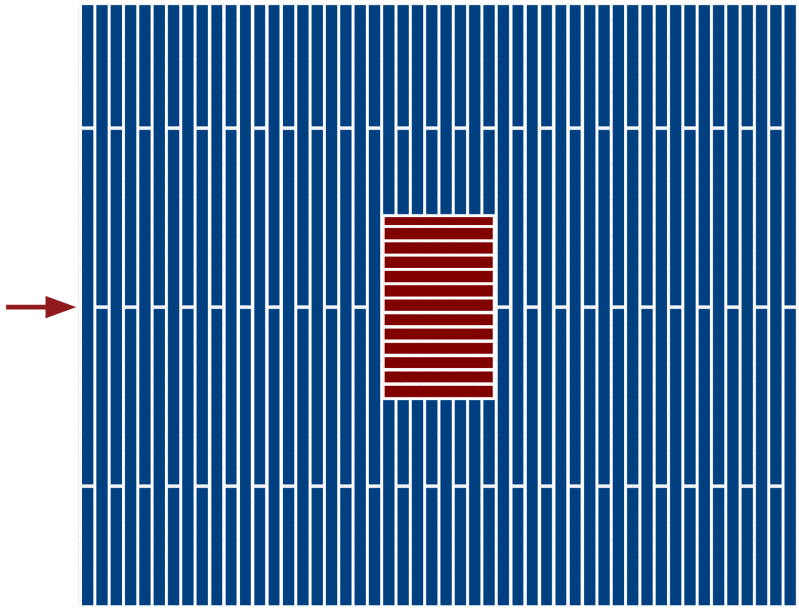

Figure 9.7: **Example of III/V stencil design:** All colored polygons are stencil apertures. Red arrow is in-plane direction for the group III beam. The entire substrate-stencil system is oriented with normal towards the group V source (out of plane). Red apertures indicate where the group III particles will be able to pass.

illustrates a physics-based solution, employing pointed spacers designed to minimize contact areas and thereby reduce the influence of Van der Waals forces. Further experimentation is required to assess the efficacy of these approaches. However, the use of cross-stabilizers with a multi-gap configuration appears to be the most versatile solution, a topic that will be elaborated upon in the upcoming chapter 10.

Figure 9.8 also demonstrates a technique for creating a ground plane, important for e.g. superconducting and optical qubit platforms. This method involves a large hash grid of stabilizers that permits flux penetration in the area surrounding the main feature (in this instance, the resonator), while maintaining a portion of the stencil suspended for design purposes. This particular technique is, however, limited to normal incidence. An alternative design, similar to the blue apertures shown in figure 9.7, could also be effective for a ground plane, with the optimal choice being contingent on the specific environmental conditions. Conclusive results, however, are pending further experimentation.

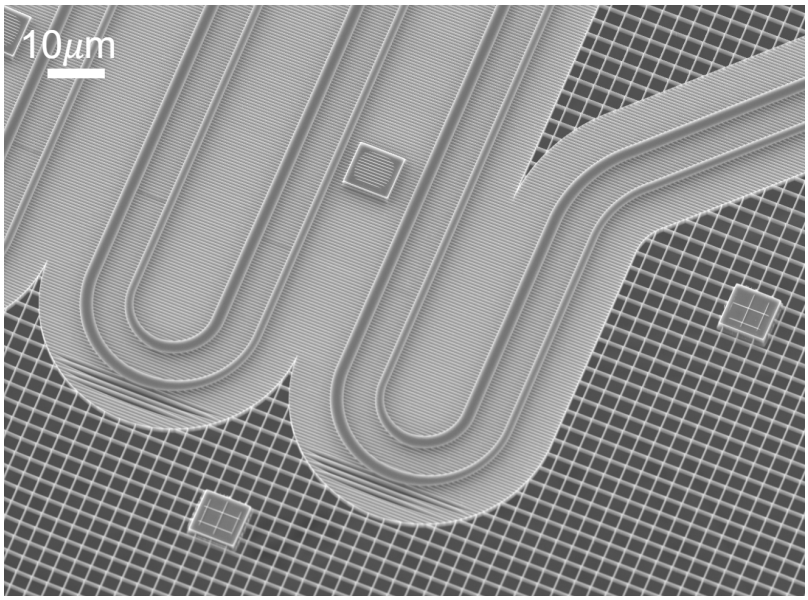

Figure 9.8: **Stabilizer "bunching" example:** SEM image of part of a stencil for an experimental resonator design. "Bunching" is clearly visible near the bottom of the rounding part for two resonator arcs where the bridges become sufficiently long without any cross-support. *Stencil fabrication and SEM image credit: Michaela Eichinger.*

9.4 Dual species atomistic simulations

In section 3.2, we introduced mean-field type simulations and noted the common simplifications employed, focusing primarily on the group III species and assuming the availability of the group V species as needed. Further, in section 9.3 above, we explored strategies to ensure ample supply of group V adatoms while modulating the selectivity via the group III flux. In simulating such a growth environment, it becomes crucial to examine the effects of the availability of both species, as well as the local lattice environment, influenced by factors like the number of bonds to neighboring lattice sites, which are affected by kinks and steps. Therefore, an atomistic approach that tracks both species is preferred for a more comprehensive understanding.

Given the involvement of two distinct species, the model necessitates separate sets of kinetic equations for each, reflecting the fact that they generally possess different energy barriers for adatom processes. Although adsorption, diffusion, and desorption rates of one species might be approximated as being largely independent of the other, processes such as nucleation, incorporation, and decomposition inherently involve both

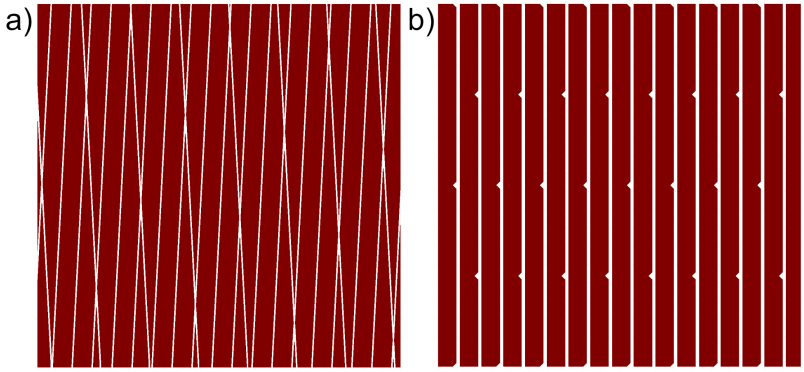

Figure 9.9: **Anti-"bunching" measures: a)** Grid of stabilizer bridges aligned by ±3°, acting as cross-stabilizers for each other. **b)** Small spacing objects (triangles in this case) placed at alternating intervals on stabilizer bridges.

species, owing to their 1:1 stoichiometry[9]. Consequently, a unified equation governs the incorporation process of both species (compare with equation 2.9):

$$\begin{aligned} \left.\frac{\partial \rho_i(x,t)}{\partial t}\right|_{\text{inc}} &= \Delta\Gamma_{sa} \\ &= \kappa_{sa} - \kappa_{as}\rho_\alpha(x,t)\rho_\beta(x,t) \end{aligned} \tag{9.13}$$

For a practical demonstration, I established a simulation for a Kossel crystal, employing transition state kinetics as described in equation 2.3. This setup included no decomposition ($\kappa_{sa} = 0$), and the process of diffusion was explicitly computed using equation 2.7 through array-wise differences to enhance computational efficiency. It is important to note that this diffusion methodology diverges from the conventional Kinetic Monte Carlo (KMC) approach, which relies on stochastic determination of random walks. Instead, this implementation utilizes an averaged diffusion of continuous variables ρ_α and ρ_β, while maintaining a discrete approach to incorporation, as indicated by the colorbars in figure 9.10. Additionally, the critical size for cluster nucleation was set to one. The binding energy at a given site was calculated linearly based on the number of bonds to nearest neighbors, including a bond to the layer beneath. The Ehrlich-Schwoebel barrier, representing the extra energy required to traverse a step edge, was established at one third of the energy of a single bond[10].

[9] Despite the distinct lattice positions occupied by the two species, the formation of a stable III/V pair depends on the concurrent presence of both. Hence, the lattice can only be completed when a full pair is incorporated. This principle applies in reverse to the process of decomposition.

[10] I received invaluable assistance from **Jonas Johansson** of Lunds Universitet in formulating the equations and providing estimations for the approximate scales of energy barriers.

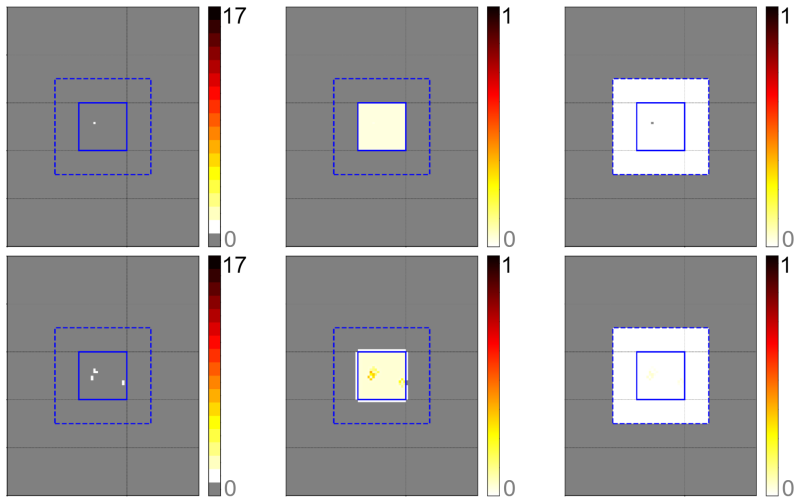

Figure 9.10: **Atomistic growth simulation 1: Top row, left to right:)** Crystal growth, Group III coverage, and Group V coverage. Solid blue lines indicates the region for direct impingement of the group III species. Dashed blue line indicates the corresponding region for the group V species. Gray background zero-level is chosen for clarity. Top row shows the distributions after the first nucleation event, bottom row shows a later stage of the same growth simulation. Later stages shown in figure 9.11 and 9.12.

An energy barrier twice as high was associated with crossing a step with a height difference exceeding unity.

Contrary to the SAG simulations discussed in section 3.2, there was no regional variation in parameter values (D, κ_{sa}, κ_{as}, and γ_{av}), reflecting the homogeneity of parameters across a substrate when a mask is not partially covering the substrate. The only variation in this case arises from the adatom density $F(x)$, regulated by the stencil apertures. While the flux input functions could be similar to those in figures 8.8 (right side), 8.10 (bottom), or 9.4d, I initially opted for a simpler approach, employing two step functions for the beam fluxes of each species, each covering a predetermined area.

Note that contrary to the SAG simulations shown back in section 3.2, no region dependence in parameter values (D, κ_{sa}, κ_{as}, and γ_{av}) was employed this time, reflecting the uniformity of parameters across a substrate in the absence of a mask. The sole difference is thus made by the adatom density $F(x)$ controlled by the stencil apertures. The flux input functions could be distributions found from flux simulations akin to that in figures 8.8 right side, 8.10 bottom, or 9.4d, but for initial simplicity, I employed two step functions for beam fluxes, one for each species covering a designated area.

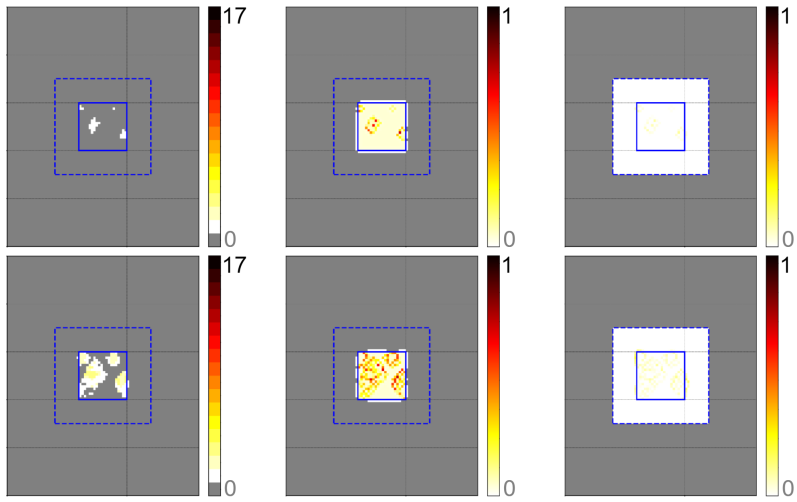

Figure 9.11: **Atomistic growth simulation 2:** Same as figure 9.10 but for later growth stages. Earlier stages shown in figure 9.10, later stages shown in figure 9.12.

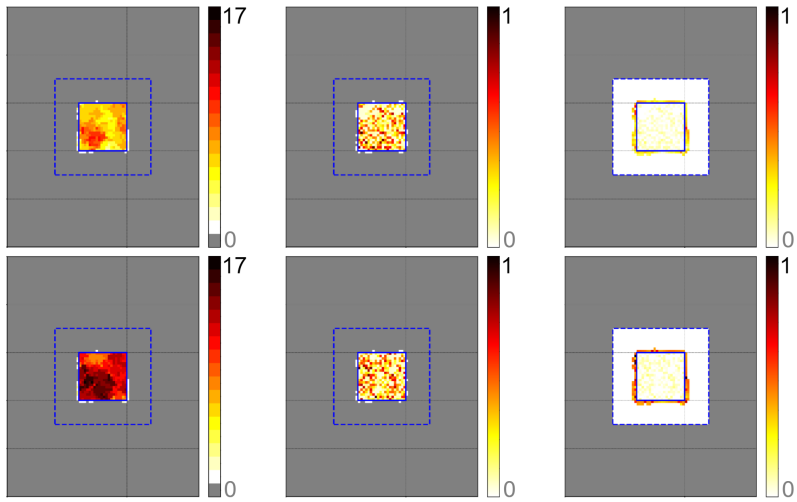

Figure 9.12: **Atomistic growth simulation 3:** Same as figure 9.10 but for later growth stages. Earlier stages shown in figures 9.10 and 9.11.

Figure 9.10 illustrates the initial phase of growth in a simulation corresponding to the methodology described above. The focus area is chosen as 80 by 100 unit cells within the Kossel crystal framework. A notable observation in the lower row is the preference for increased adatom coverage at the periphery of nucleated clusters, attributable to the enhanced bonding opportunities present at step or kink sites. In the developmental

stages captured in figure 9.11, a formation of several islands is discernible, alongside the nucleation of additional layers atop these recently formed islands. These islands expand to the boundary of the group III-impingement zone, while negligible growth is observed beyond this predefined area[11]. Subsequent stages, as depicted in figure 9.12, exhibit the development of multiple layers. A distinct accumulation of group V species is observed around the perimeter of the group III-impingement region, facilitated by the presence of a step edge. This also serves to constrain the diffusion length of the group III species through incorporation-limited diffusion. It is crucial to acknowledge that the outcomes of such a simulation are profoundly influenced by the input parameters, implying that these results do not represent an actual III/V growth system. Nevertheless, they do provide elementary insights into certain aspects of crystal growth phenomena discussed in sections 2.2 and 2.4. Furthermore, the flux distributions derived from simulation procedures outlined previously could offer valuable data for more intricate simulations of a similar nature.

Commentary on dual species adatom kinetics

While the simulations above are interesting for our initial examinations, the simplified framework warrants a few comments – details which could have been added and explored, had more time been available. A more rigorous framework would involve considerations of more detailed adatom mechanisms for the two species. We will denote the two atomic species α and β, corresponding to the group III and group V species, respectively, now with normalized densities $\rho_\alpha \in [0,1]$ and $\rho_\beta \in [0,1]$. For each of the two species, we are concerned with the same processes as before: adsorption, diffusion, decomposition, incorporation, and desorption.

The group V species is assumed to adsorb as dimers[26, 27, 149], which we can express with quadratic scaling of the vacant sites. Quadratic scaling is computationally much lighter than a more complex process of counting neighbors, weighing probabilities for dimer formation upon adsorption with each unoccupied neighboring site etc. Putting these assumptions for adsorption together in rate equations:

$$\begin{aligned} \left.\frac{\partial \rho_\alpha(x,t)}{\partial t}\right|_{\text{beam}} &= F_\alpha(x,t) \\ \left.\frac{\partial \rho_\beta(x,t)}{\partial t}\right|_{\text{beam}} &= F_\beta(x,t)\Big(1-\rho_\beta(x,t)\Big)^2 \end{aligned} \tag{9.14}$$

with $\big(1-\rho_i(x,t)\big)$ being the normalized density of unoccupied lattice sites, and $F_i(x,t)$ the adsorption independent normalized rate of atoms

[11] This specificity in growth patterns is intricately linked to the chosen energy barriers in the simulation, with particular emphasis on the Ehrlich-Schwoebel barrier and the barrier confronting an adatom in surmounting a step exceeding one unit in height.

impinging onto the substrate from each beam. Note that the second equation 9.14 goes to zero in the "usual" limit where the group V species is available everywhere[12].

Regarding incorporation and decomposition in equation 9.13 above, we note that the term κ_{sa} could have a factor of $(1-\rho_\alpha(x,t)(1-\rho_\beta(x,t)$, since decomposition would produce adatom, which need to appear in a vacancy. We omit this extra term for the same reason as the omission of $(1-\rho)$ in the adsorption rate back in chapter 2.2. We also note that equation 9.13 is consistent with equation 2.9 in the limit of high group V overpressure ($\rho_\beta = 1$).

We remark from literature[24] that group III atoms are shown to desorb as single atoms[32, 33], while the group V species desorbs primarily as dimers[26, 27, 149]. This leads to desorption rates of the two species being respectively linear and quadratic with the normalized densities of the adatoms:

$$\begin{aligned} \frac{\partial \rho_\alpha(x,t)}{\partial t}\Big|_{deso} &= -\gamma^\alpha_{av}\rho_\alpha(x,t) \\ \frac{\partial \rho_\beta(x,t)}{\partial t}\Big|_{deso} &= -\gamma^\beta_{av}\rho_\beta(x,t)^2 \end{aligned} \tag{9.15}$$

Note that the quadratic scaling makes a negligible difference in the limit of high group V overpressure ($\rho_\beta = 1$).

Based on the considerations in sections 2.3 and 9.4 here, we list the differential equation for the two species (with implicit dependence on x and t):

$$\begin{aligned} \frac{\partial \rho_\alpha}{\partial t} &= F_\alpha + D_\alpha\nabla^2\rho_\alpha + \kappa_{sa} - \kappa_{as}\rho_\alpha\rho_\beta - \gamma^\alpha_{av}\rho_\alpha \\ &= D_\alpha\nabla^2\rho_\alpha - \rho_\alpha\left(\gamma^\alpha_{av} + \kappa_{as}\rho_\beta\right) + \left(F_\alpha + \kappa_{sa}\right) \end{aligned} \tag{9.16}$$

$$\begin{aligned} \frac{\partial \rho_\beta}{\partial t} &= F_\beta\left(1-\rho_\beta\right)^2 + D_\beta\nabla^2\rho_\beta + \kappa_{sa} - \kappa_{as}\rho_\alpha\rho_\beta - \gamma^\beta_{av}\rho_\beta^2 \\ &= D_\beta\nabla^2\rho_\beta + \rho_\beta^2\left(F_\beta - \gamma^\beta_{av}\right) - \rho_\beta\left(2F_\beta + \kappa_{as}\rho_\alpha\right) + \left(F_\beta + \kappa_{sa}\right) \end{aligned} \tag{9.17}$$

where the terms in the first lines represents the contributions from adsorption, diffusion, decomposition, incorporation, and desorption, and

[12] Under the usual group V overpressure conditions, it is more likely that constant high rates of decomposition and incorporation – and especially desorption and adsorption – are what keeps the surface stable. This effectively results in a net zero rate with full occupancy.

the colors highlight the terms coupling the densities of the two species. On the second line, the terms are then gathered into a diffusion term, followed by terms in decreasing order in the dependent variable. Note that the parameters governing the different types of transitions (D_i, κ_{sa}, κ_{as}, and γ^i_{av}) in equations 9.16 and 9.17 are explicitly written as dependent on the adatom species. However, these parameters are – as before – also functions of both the adatom species and the local environment.

Finally, we note that the Kossel crystal simulation is a very rough simplification, and a more detailed simulation would incorporate the potential energy landscape, which is an expression of the surface reconstruction, which would in turn be dependent on the partial pressures incident on the substrate. This adds a further layer of complication, and is left for further simulation based studies.

9.5 Substrate transformations

In section 9.3, we introduced the idea of an alternate substrate orientation – with substrate-normal (and stencil-normal) directed towards one of the beam sources. Thus, in order to keep the equations of the previous sections 7 and 8 relevant, it would be highly useful with a way to express the other beam source positions (for sources j) relative to this new, alternate substrate orientation (z-axis substrate-normal oriented towards source i).

In the coordinate system of this new system, the unit vector towards beam source i is labeled $\boldsymbol{u_i} = (0,0,1)$. The matrix which achieves this transformation of $\boldsymbol{v_i} \rightarrow \boldsymbol{u_i}$ is conveniently the matrix which reverts the transformation we applied back in equation 9.8:

$$\begin{aligned}
\boldsymbol{M^{-1}_{\theta_i,\phi_i}} &= \boldsymbol{M_{-\phi_i,-\theta_i}} = \boldsymbol{M_{-\theta_i}} \times \boldsymbol{M_{-\phi_i}} \\
&= \begin{bmatrix} 1 & 0 & 0 \\ 0 & \cos(\theta_i) & -\sin(\theta_i) \\ 0 & \sin(\theta_i) & \cos(\theta_i) \end{bmatrix} \times \begin{bmatrix} \cos(\phi_i) & \sin(\phi_i) & 0 \\ -\sin(\phi_i) & \cos(\phi_i) & 0 \\ 0 & 0 & 1 \end{bmatrix} \\
&= \begin{bmatrix} \cos(\phi_i) & \sin(\phi_i) & 0 \\ -\cos(\theta_i)\sin(\phi_i) & \cos(\theta_i)\cos(\phi_i) & -\sin(\theta_i) \\ -\sin(\theta_i)\sin(\phi_i) & \sin(\theta_i)\cos(\phi_i) & \cos(\theta_i) \end{bmatrix}
\end{aligned} \tag{9.18}$$

A quick check using $\boldsymbol{v_i}$ from equation 9.9 confirms that indeed $\boldsymbol{M^{-1}_{\theta_i,\phi_i}}\,\boldsymbol{v_i} = (0,0,1)$. Applying the same matrix $\boldsymbol{M^{-1}_{\theta_i,\phi_i}}$ to another unit vector $\boldsymbol{v_j}$ (from equation 9.9) now yields the position of beam source j in the new system:

$$\begin{aligned}\boldsymbol{M}^{-1}_{\boldsymbol{\theta_i},\boldsymbol{\phi_i}}\boldsymbol{v_j} &= \begin{bmatrix}\cos(\phi_i) & \sin(\phi_i) & 0\\ -\cos(\theta_i)\sin(\phi_i) & \cos(\theta_i)\cos(\phi_i) & -\sin(\theta_i)\\ -\sin(\theta_i)\sin(\phi_i) & \sin(\theta_i)\cos(\phi_i) & \cos(\theta_i)\end{bmatrix}\begin{bmatrix}-\sin(\theta_j)\sin(\phi_j)\\ \sin(\theta_j)\cos(\phi_j)\\ \cos(\theta_j)\end{bmatrix}\\ &= \begin{bmatrix}-\sin(\theta_j)\sin(\phi_{j,i})\\ \cos(\theta_i)\sin(\theta_j)\cos(\phi_{j,i})-\sin(\theta_i)\cos(\theta_j)\\ \sin(\theta_i)\sin(\theta_j)\cos(\phi_{j,i})+\cos(\theta_i)\cos(\theta_j)\end{bmatrix}\\ &= \begin{bmatrix}u^x_j\\ u^y_j\\ u^z_j\end{bmatrix} \equiv \boldsymbol{u_j}\end{aligned} \tag{9.19}$$

where all quantities are expressed in the original system, and we have once again used the fact that we can choose our original coordinate system such that $\phi_i = 0$. While not very illuminating in itself, equation 9.19 does allow us to express the angle $\theta_{j,i} = \arccos\left(u^z_j\right)$, the result of which corresponds with equation 9.12 from earlier. More importantly, equation 9.19 contains the coordinates u^x_j and u^y_j, which allows calculation of the in-plane directions towards sources j and k – with in-plane referring to projection onto the new substrate direction, with the substrate-normal oriented towards beam source i. From the projections onto the new substrate orientation: $\boldsymbol{u'_j} \equiv \left(u^x_j, u^y_j\right)$ and $\boldsymbol{u'_k} \equiv \left(u^x_k, u^y_k\right)$, equation 9.10 can now be applied to $\boldsymbol{u'_j}$ and $\boldsymbol{u'_k}$ to obtain the in-plane angle directly.

$$\phi^i_{j,k} = \arccos\left(\frac{\boldsymbol{u'_j}\cdot\boldsymbol{u'_k}}{|\boldsymbol{u'_j}||\boldsymbol{u'_k}|}\right) \tag{9.20}$$

where $\phi^i_{j,k}$ is the in-plane angle between directions towards sources j and k given a substrate-orientation towards source i. Note that the denominator no longer vanishes due to the generally non-zero components u^z_j and u^z_k in equation 9.19.

To reiterate: for two sources i and j, with the substrate-normal directed towards beam source i, the in-plane direction towards source j may be chosen freely by simple rotation about the new substrate-normal. However, with the appearance of a third source k, the in-plane angles between sources j and k will matter for the flux filtering selectivity as outlined in the previous section 9.3. For the purposes of III/V semiconductors, this would be relevant for ternary growth of e.g. $In_xGa_{1-x}As$ where the substrate-normal could be oriented towards the As source i, with In and Ga playing the parts of sources j and k. In this case the angles $\theta_{i,j}$, $\theta_{i,k}$ (from equation 9.12) and $\phi^i_{j,k}$ (from equation 9.20) would determine the adaptations necessary to control the In and Ga fluxes with adaptations described in section 9.1.

10

Multi-gap flux filtering stencils

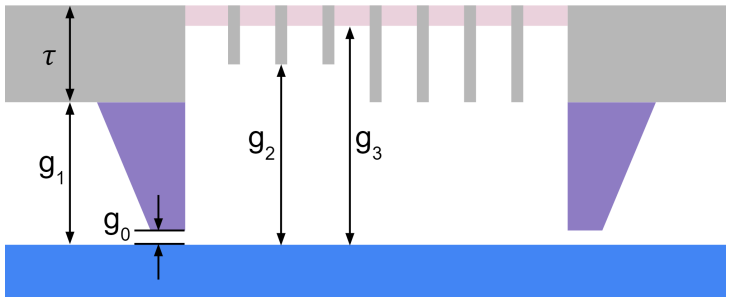

Figure 10.1: **Multi-gap stencil concept:** The basic concept for a flux filtering multi-gap stencil. Gray is "original" flux filtering stencil. Purple "frame" is added around feature outlines, either locally or in a surrounding area, defining an additional gap. Light magenta features are (alternating) cross-stabilizers akin to those in figure 9.7, which may define an additional type of gap.

Patent application number EP23219430.8 covering the techniques described in this chapter was filed on December 21st 2023.

10.1 Good gap, bad gap

Chapter 7 should have made a clear case for why higher purity and thus device fidelity is ultimately on offer with a stencil approach, compared to mask-on-substrate: the resistless fabrication means no resist or cleaning of such needs to intermix with our UHV fabrication steps. Simultaneously. In chapter 8 we went through ways of removal of some general stencil limitations, and with the flux filtering stencils we even manage to gain control features no otherwise offered by a default stencil approach, including directional selectivity for deposition of multiple materials in one in-situ step. We expanded upon this with speculations of dual species growth in chapter 9, adding the use of cross-stabilizers and hinting at multi-gap stencils.

Back in chapter 8 we concluded that flux broadening is a blessing and a curse. Broadening is the phenomenon which allows us a continuous particle flux even in the presence of stabilizer bridges, and a certain gap g is necessary for this. Meanwhile the same gap leads to feature outlines being "blurred"[139], which is detrimental to circuit quality and generally undesirable from a design perspective. Multi-gap stencils harness the broadening for flux continuity, while keeping sharp feature outlines and flux termination.

Figure 10.1 shows the basic concept in the "end view", zone axis parallel with stabilizer bridges. A purple frame is added to the bottom of the stencil, tracing the outline of features, where broadening needs to be sharp and

controlled (equation 7.3). The difference in color is for display purposes only – the frame could consist of the same material as the rest of the stencil. The distance between the substrate and this frame is g_0. Inside features the original gap g_1 controls the broadening underneath stabilizer bridges needed for continuous flux. The height of the frame additionally helps control the other gaps, as the morphology of the stencil can be engineered, characterized and optimized for the stencil before any UHV deposition (section 7.1). The stencil thickness (effectively the gap between substrate and bridges) may be varied locally, as this is one of the parameters for flux control, as we saw in chapter 8. This adds one or more additional gaps, in this case displayed as g_2. Finally, as mentioned in the previous section, cross-stabilizers can be necessary to avoid "bunching" of stabilizer bridges (section 9.3), and the shadow cast from these at angled depositions can be minimized if they span a limited height (figure 10.3), which in this case defines gap g_3.

As is evident from the conceptual drawing above, one can envision a plurality of different gaps at different aperture arrays, depending on the flux desired through these. Meanwhile the frame at gap g_0 serves an additional purpose, other than merely ensuring sharp feature outlines. The frames may serve as contact points, with smaller contact area compared to the full stencil, which carries fewer challenges when attempting to hard contact the substrate; a smaller contact area means less risk of a stray speck of dust or particle left from wafer cleaving being pinned between substrate and stencil, preventing hard contact. Figure 10.2 shows two different iterations of this frame, depending on how localized the framing structure is. More localized frames should be easier to use in the "hard contact" mode $g_0 = 0$, but the may be too susceptible to breaking or carry other issues (i.e. fabrication related). More localized frames may also be called for as they occupy less area on the stencil.

10.2 Angled apertures

One additional iteration on the multi-gap stencils is the use of angled side walls[1]. The angled walls could be for the features, stabilizer bridges and for the frames, depending on use case. If the stencil is fabricated from e.g. silicon, we note the selective tendency for wet etching towards "finding" the {111} facets, which might be exploited for fabrication of low roughness stencils with angled side walls.

Flux filtering stencils rely on angled depositions, which inherently carries "frontside" and "backside" broadenings as derived back in section 7. The discrepancy between these two broadening scales with the stencil

[1] Angled side walls could also be implemented separately from the multi-gap approach. This option was indeed included in the patent application PCT/EP2023/066474, covering the flux filtering stencils, however it gains relevance with the increased control of the broadening which comes with the multi-gap technique.

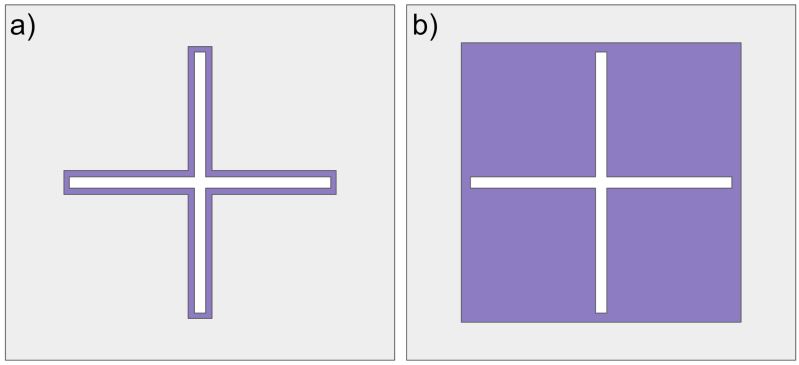

Figure 10.2: **Multi-gap frame types:** The "+" shape is the feature in question. Assume appropriate flux filtering is chosen (although not shown). **a)** A very localized frame (purple) just around the outline of the main feature. **b)** An "area" type frame, where a larger area surrounding the feature is included.

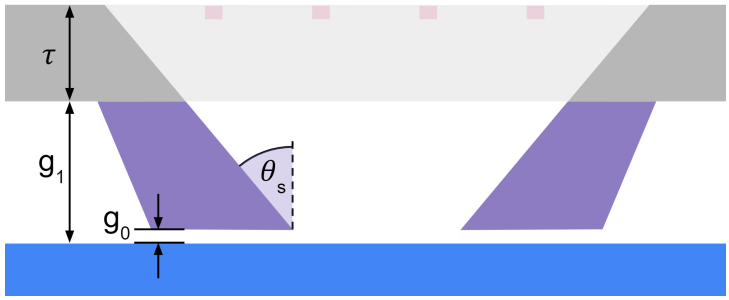

Figure 10.3: **Angled side wall stencils:** Schematic of stencil with angled side walls. Actual implementation could be combined with any number of flux filtering stabilizer bridges (light gray) and cross-stabilizers (light magenta). The angled walls counteract the discrepancy in "frontside" and "backside" broadening.

thickness, as the frontside part of the pattern is caused by the stencil top partially obstructing flux. This would no longer be the case if the incidence angle was chosen such that $\theta < \theta_s$[2] with θ_s being the angle of the side walls as displayed in figure 10.3. This leaves us with effectively a single broadening set by the gap g_0. Since we are envisioning this multi-gap stencil used in the hard contact mode $g_0 \to 0$, each single-species deposition could be carried out in the parallel (ϕ) and anti-parallel ($-\phi$) direction to further increase uniformity. This may or may not be feasible for multi-species

[2] Due to the existence of beam angle spread, σ, from section 8.4, we would more precisely require $\theta < \theta - \sigma$ instead.

depositions, depending on the setup of the growth chamber.

10.3 Flux filtering multi-gap stencil summary

A lot of ideas were presented in the last few chapters, and a brief summary highlighting the key differences and advantages offered by these stencil based techniques is in order. The analytic framework along with flux simulations and the experimental verification of blocking by in-plane misalignment proves that flux filtering by series of aperture arrays works as intended, and this new technique comes with several notable advantages. Some of these advantages address concerns relevant to stencils in general (see section 7), while other alleviate broadening issues related to the novel flux filtering stencils. Summarizing the key points in no particular order:

- Resistless, as opposed to mask-on-substrate based techniques
- No intermixing of resist/lithography and UHV fab steps
- Unlocking design possibilities, e.g. "closed loop"
- Increased mechanical stability for e.g. "cantilever" type designs
- Reusable stencils increasing fabrication reproducibility
- Separate stencil characterization and optimization
- Multiple depositions possible in one in-situ step
- Additional tuning parameters for flux distributions

Part IV

Conclusion and outlook

11

Conclusion

11.1 Summary

This thesis has covered a lot of topics, all related to bottom-up synthesis of quantum circuits in one way or another.

The initial chapters 1 and 2 provided a foundational overview of circuit fabrication processes, specifically tailored to quantum device applications. This included an examination of the kinetics and thermodynamics of crystal growth, underlining the importance of controlled crystal growth as a key element in bottom-up synthesis methodologies. Such understanding is imperative for integrating crystal growth phenomena into the synthesis strategies for quantum devices.

Subsequently, in chapters 3, 4, 5, and 6, the focus shifted to an exploration of the mask-on-substrate based patterning techniques, summarizing key findings from various studies in these domains. This section delved into the intricacies of patterning via Selective Area Growth (SAG), highlighting how the modulation of design parameters can influence adatom kinetics and, consequently, growth rates. Additionally, this part explored the formation of misfit dislocations within heterostructures, revealing collective nucleation at critical thickness thresholds.

The third part of this thesis, spanning chapters 7, 8, 9, and 10, introduced the fundamental stencil methodology, subsequently augmenting it with innovations such as flux filtering through stencil apertures. This advancement enabled selectivity based on deposition direction and mitigated some limitations inherent in the conventional stencil approach. The multi-gap stencil, a novel addition, effectively balanced the advantages and drawbacks of broadening phenomena, ultimately offering an integrated solution for the simultaneous deposition of multiple materials in a single in-situ process with sharp feature outline control. While challenges in engineering persist, this method has the potential to achieve higher levels of cleanliness compared to traditional techniques.

It is crucial to acknowledge that the foundational principles discussed in the earlier chapters remain applicable to stencil based methodologies. The synthesis of circuits still involves crystal growth processes, with both kinetic and thermodynamic factors playing significant roles. This was briefly addressed in section 9.2, focusing on broadening and contact angle effects, and further illustrated through basic simulations in section 9.4. However, a more comprehensive framework for stencil methods should incorporate all relevant morphological and thermodynamic driving forces. Currently, our emphasis has been on flux distribution, which represents the preliminary step in controlling inputs and predicting outputs.

Our analysis of growth rates revealed that the key to selectivity in SAG lies in managing differing kinetic barriers across adjacent regions, linking growth rates directly with design parameters. While stencil techniques employ a distinct control mechanism, primarily through flux distribution, the lateral movement of adatoms on the substrate is expected to similarly

affect growth rates in complex ways. Additionally, our investigations into misfit dislocations for SAG-related morphologies also hold relevance for structures created via stencil deposition, particularly in the context of controlling misfit-induced defects.

In summary, transitioning to techniques based on multi-gap flux filtering stencils necessitates substantial advancements in theoretical frameworks, simulations, engineering practices, and fabrication processes. However, the successful adaptation of these methods could be a pivotal catalyst in advancing qubit coherence and fidelity, potentially enabling a significant leap forward in the field of quantum computing.

Bibliography

[P1] M. E. Cachaza, A. W. Christensen, D. Beznasyuk, T. Særkjær, M. H. Madsen, R. Tanta, G. Nagda, S. Schuwalow, and P. Krogstrup. "Selective area growth rates of III-V nanowires". In: *Phys. Rev. Mater.* 5 (9 2021), p. 094601. DOI: 10.1103/PhysRevMaterials.5.094601. URL: https://link.aps.org/doi/10.1103/PhysRevMaterials.5.094601.

[P2] T. Særkjær, T. Christian Thann, S. Schuwalow, and P. Krogstrup. "Collective formation of misfit dislocations at the critical thickness for equilibrium nanowire heterostructures". In: *Journal of Crystal Growth* 622 (2023), p. 127400. ISSN: 0022-0248. DOI: https://doi.org/10.1016/j.jcrysgro.2023.127400. URL: https://www.sciencedirect.com/science/article/pii/S0022024823003263.

[P3] T. Særkjær, M. Eichinger, T. K. Nordqvist, M. Kjaergaard, and P. Krogstrup. "Geometrical approach to finite source shadow selectivity". In: *TBD [in preparation]* (2023).

[P4] M. Eichinger, T. Særkjær, T. K. Nordqvist, M. Kjaergaard, and P. Krogstrup. "The Shadow Mask Polarizer - A stencil lithography technique for the in-situ fabrication of quantum devices". In: *TBD [in preparation]* (2023).

[5] T. R. S. A. of Sciences. *The Nobel Prize in Physics 2000*. Feb. 2023. URL: https://www.nobelprize.org/prizes/physics/2000/press-release/.

[6] S. Chowdhury. *Design for Six Sigma: The Revolutionary Process for Achieving Extraordinary Profits*. Dearborn Trade Pub., 2002. ISBN: 9780793152247. URL: https://books.google.dk/books?id=bdl7GdpLjj0C.

[7] T. Hasenkamp and A. Olme. "Introducing Design for Six Sigma at SKF". In: *International Journal of Six Sigma and Competitive Advantage* 4.2 (2008), pp. 172–189. DOI: 10.1504/IJSSCA.2008.020281. eprint: https://www.inderscienceonline.com/doi/pdf/10.1504/IJSSCA.2008.020281. URL: https://www.

inderscienceonline.com/doi/abs/10.1504/IJSSCA.2008.020281.

[8] A. Premkumar, C. Weiland, S. Hwang, B. Jäck, A. P. M. Place, I. Waluyo, A. Hunt, V. Bisogni, J. Pelliciari, A. Barbour, M. S. Miller, P. Russo, F. Camino, K. Kisslinger, X. Tong, M. S. Hybertsen, A. A. Houck, and I. Jarrige. "Microscopic relaxation channels in materials for superconducting qubits". In: *Communications Materials* 2.1 (2021), p. 72. ISSN: 2662-4443. DOI: 10.1038/s43246-021-00174-7. URL: https://doi.org/10.1038/s43246-021-00174-7.

[9] I. Siddiqi. "Engineering high-coherence superconducting qubits". In: *Nature Reviews Materials* 6.10 (2021), pp. 875–891. ISSN: 2058-8437. DOI: 10.1038/s41578-021-00370-4. URL: https://doi.org/10.1038/s41578-021-00370-4.

[10] P. Krantz, M. Kjaergaard, F. Yan, T. P. Orlando, S. Gustavsson, and W. D. Oliver. "A quantum engineer's guide to superconducting qubits". In: *Applied Physics Reviews* 6.2 (2019), p. 021318. ISSN: 1931-9401. DOI: 10.1063/1.5089550. eprint: https://pubs.aip.org/aip/apr/article-pdf/doi/10.1063/1.5089550/16667201/021318_1_online.pdf. URL: https://doi.org/10.1063/1.5089550.

[11] M. Kjaergaard, M. E. Schwartz, J. Braumüller, P. Krantz, J. I.-J. Wang, S. Gustavsson, and W. D. Oliver. "Superconducting Qubits: Current State of Play". In: *Annual Review of Condensed Matter Physics* 11.1 (2020), pp. 369–395. DOI: 10.1146/annurev-conmatphys-031119-050605. eprint: https://doi.org/10.1146/annurev-conmatphys-031119-050605. URL: https://doi.org/10.1146/annurev-conmatphys-031119-050605.

[12] P. Schüffelgen, D. Rosenbach, C. Li, T. W. Schmitt, M. Schleenvoigt, A. R. Jalil, S. Schmitt, J. Kölzer, M. Wang, B. Bennemann, U. Parlak, L. Kibkalo, S. Trellenkamp, T. Grap, D. Meertens, M. Luysberg, G. Mussler, E. Berenschot, N. Tas, A. A. Golubov, A. Brinkman, T. Schäpers, and D. Grützmacher. "Selective area growth and stencil lithography for in situ fabricated quantum devices". In: *Nature Nanotechnology* 14.9 (2019), pp. 825–831. ISSN: 1748-3395. DOI: 10.1038/s41565-019-0506-y. URL: https://doi.org/10.1038/s41565-019-0506-y.

[13] T. Særkjær. *Morphologies of Selective Area Grown Nanowires*. eng. 2020.

[14] P. Krogstrup, H. I. Jørgensen, E. Johnson, M. H. Madsen, C. B. Sørensen, A. F. i Morral, M. Aagesen, J. Nygård, and F. Glas. "Advances in the theory of III–V nanowire growth dynamics". In: *Journal of Physics D: Applied Physics* 46.31 (2013), p. 313001. DOI: 10.1088/0022-3727/46/31/313001. URL: https://dx.doi.org/10.1088/0022-3727/46/31/313001.

[15] M. Henini. “Molecular beam epitaxy from research to mass-production — Part 1”. In: *III-Vs Review* 9.3 (1996), pp. 32–34. ISSN: 0961-1290. DOI: https://doi.org/10.1016/S0961-1290(96)80125-6. URL: https://www.sciencedirect.com/science/article/pii/S0961129096801256.

[16] A. C. Levi and M. Kotrla. “Theory and simulation of crystal growth”. In: *Journal of Physics: Condensed Matter* 9.2 (1997), p. 299. DOI: 10.1088/0953-8984/9/2/001. URL: https://dx.doi.org/10.1088/0953-8984/9/2/001.

[17] H. M. Cuppen. “Theory and simulations of crystal growth. Fundamental steps in morphology prediction”. In: 2005.

[18] E. Mårtensson. “Kinetic and Thermodynamic Modeling of Nanowire Growth”. English. Defence details Date: 2021-10-26 Time: 13:15 Place: Lecture hall Rydbergsalen, Department of Physics, Sölvegatan 14, Faculty of Engineering LTH, Lund University, Lund. Zoom: : https://lu-se.zoom.us/j/67026065957?pwd=YTZ6RGVuaXFtRVFqZ1JydGh6NGI5dz09 Passcode: 416469 External reviewer(s) Name: Voorhees, Peter W. Title: Prof. Affiliation: Northwestern University, USA. —. Doctoral Thesis (compilation). 2021. ISBN: 978-91-8039-008-8.

[19] E. Leshchenko. “Kinetic and thermodynamic modelling of ternary nanowire growth”. English. Defence details Date: 2021-10-29 Time: 09:15 Place: Lecture hall Rydbergsalen, Department of Physics, Sölvegatan 14, Faculty of Engineering LTH, Lund University, Lund. Zoom: https://lu-se.zoom.us/j/65213868705?pwd=eG54ditNelREdVFEei80ZXM3Z01jQT09 Passcode: 272441 External reviewer(s) Name: Martelli, Faustino Title: Prof. Affiliation: IMM-CNR, Italy. —. Doctoral Thesis (compilation). Lund University, 2021. ISBN: 978-91-8039-006-4.

[20] M. Borgström, K. Deppert, L. Samuelson, and W. Seifert. “Size- and shape-controlled GaAs nano-whiskers grown by MOVPE: a growth study”. In: *Journal of Crystal Growth* 260.1 (2004), pp. 18–22. ISSN: 0022-0248. DOI: https://doi.org/10.1016/j.jcrysgro.2003.08.009. URL: https://www.sciencedirect.com/science/article/pii/S0022024803016609.

[21] J. Johansson, C. Svensson, T. Mårtensson, L. Samuelson, and W. Seifert. “A mass-transport model for semiconductor nanowire growth”. English. In: *Book of extended abstracts: 11th European Workshop on MOVPE, Lausanne, Switzerland (2005)*. 11th European Workshop on MOVPE, Lausanne, Switzerland (2005) ; Conference date: 02-01-0001. 2005.

[22] T. Kanne. “Growth and Characterization of Semiconductor-Superconductor Nanowire Hybrids”. English. PhD thesis. 2021. URL: https://nbi.ku.dk/english/theses/phd-theses/nordqvist/.

[23] I. Langmuir. “THE ADSORPTION OF GASES ON PLANE SURFACES OF GLASS, MICA AND PLATINUM.” In: *Journal of the American Chemical Society* 40.9 (1918), pp. 1361–1403. DOI: 10.1021/ja02242a004. eprint: https://doi.org/10.1021/ja02242a004. URL: https://doi.org/10.1021/ja02242a004.

[24] S. Karpov and M. Maiorov. “Model of the adsorption/desorption kinetics on a growing III–V compound surface”. In: *Surface Science* 393.1 (1997), pp. 108–125. ISSN: 0039-6028. DOI: https://doi.org/10.1016/S0039-6028(97)00563-3. URL: https://www.sciencedirect.com/science/article/pii/S0039602897005633.

[25] H. Eyring. “The Activated Complex in Chemical Reactions”. In: *The Journal of Chemical Physics* 3.2 (2004), pp. 107–115. ISSN: 0021-9606. DOI: 10.1063/1.1749604. eprint: https://pubs.aip.org/aip/jcp/article-pdf/3/2/107/11062599/107_1_online.pdf. URL: https://doi.org/10.1063/1.1749604.

[26] C. Foxon and B. Joyce. “Interaction kinetics of As4 and Ga on 100 GaAs surfaces using a modulated molecular beam technique”. In: *Surface Science* 50.2 (1975), pp. 434–450. ISSN: 0039-6028. DOI: https://doi.org/10.1016/0039-6028(75)90035-7. URL: https://www.sciencedirect.com/science/article/pii/0039602875900357.

[27] C. Foxon and B. Joyce. “Interaction kinetics of As2 and Ga on 100 GaAs surfaces”. In: *Surface Science* 64.1 (1977), pp. 293–304. ISSN: 0039-6028. DOI: https://doi.org/10.1016/0039-6028(77)90273-4. URL: https://www.sciencedirect.com/science/article/pii/0039602877902734.

[28] A. Fick. “On liquid diffusion”. In: *Journal of Membrane Science* 100.1 (1995). The early history of membrane science selected papers celebrating vol. 100, pp. 33–38. ISSN: 0376-7388. DOI: https://doi.org/10.1016/0376-7388(94)00230-V. URL: https://www.sciencedirect.com/science/article/pii/037673889400230V.

[29] V. G. Dubrovskii. “Theory of MBE Growth of Nanowires on Adsorbing Substrates: The Role of the Shadowing Effect on the Diffusion Transport”. In: *Nanomaterials* 12.7 (2022). ISSN: 2079-4991. DOI: 10.3390/nano12071064. URL: https://www.mdpi.com/2079-4991/12/7/1064.

[30] X.-Q. Shen, D. K. D. Kishimoto, and T. N. T. Nishinaga. “Arsenic Pressure Dependence of Surface Diffusion of Ga on Nonplanar GaAs Substrates”. In: *Japanese Journal of Applied Physics* 33.1R (1994), p. 11. DOI: 10.1143/JJAP.33.11. URL: https://dx.doi.org/10.1143/JJAP.33.11.

[31] O. Medvedev. “Diffusion Coefficients in Multicomponent Mixtures”. English. PhD thesis. 2005. ISBN: 87-90142-94-2.

[32] K. R. Evans, C. Stutz, D. Lorance, and R. Jones. “Effects of strain and surface reconstruction on the kinetics of indium incorporation in MBE growth of InAs”. In: *Journal of Crystal Growth* 95.1 (1989), pp. 197–200. ISSN: 0022-0248. DOI: https://doi.org/10.1016/0022-0248(89)90381-3. URL: https://www.sciencedirect.com/science/article/pii/0022024889903813.

[33] E. M. Gibson, C. T. Foxon, J. Zhang, and B. A. Joyce. “Gallium desorption from GaAs and (Al,Ga)As during molecular beam epitaxy growth at high temperatures”. In: *Applied Physics Letters* 57.12 (1990), pp. 1203–1205. ISSN: 0003-6951. DOI: 10.1063/1.103485. eprint: https://pubs.aip.org/aip/apl/article-pdf/57/12/1203/7776901/1203_1_online.pdf. URL: https://doi.org/10.1063/1.103485.

[34] G. Wulff. In: *Zeitschrift für Kristallographie - Crystalline Materials* 34.1-6 (1901), pp. 449–530. DOI: doi:10.1524/zkri.1901.34.1.449. URL: https://doi.org/10.1524/zkri.1901.34.1.449.

[35] M. v. Laue. In: 105.1-6 (1943), pp. 124–133. DOI: doi:10.1524/zkri.1943.105.1.124. URL: https://doi.org/10.1524/zkri.1943.105.1.124.

[36] R. F. Sekerka. “Equilibrium and growth shapes of crystals: how do they differ and why should we care?” In: *Crystal Research and Technology* 40.4-5 (2005), pp. 291–306. DOI: https://doi.org/10.1002/crat.200410342. eprint: https://onlinelibrary.wiley.com/doi/pdf/10.1002/crat.200410342. URL: https://onlinelibrary.wiley.com/doi/abs/10.1002/crat.200410342.

[37] I. W. Yeu, G. Han, J. Park, C. S. Hwang, and J.-H. Choi. “Equilibrium crystal shape of GaAs and InAs considering surface vibration and new (111)B reconstruction: ab-initio thermodynamics”. In: *Scientific Reports* 9.1 (2019), p. 1127. ISSN: 2045-2322. DOI: 10.1038/s41598-018-37910-y. URL: https://doi.org/10.1038/s41598-018-37910-y.

[38] N. Moll, A. Kley, E. Pehlke, and M. Scheffler. “GaAs equilibrium crystal shape from first principles”. In: *Phys. Rev. B* 54 (12 1996), pp. 8844–8855. DOI: 10.1103/PhysRevB.54.8844. URL: https://link.aps.org/doi/10.1103/PhysRevB.54.8844.

[39] S. B. Zhang and S.-H. Wei. “Surface Energy and the Common Dangling Bond Rule for Semiconductors”. In: *Phys. Rev. Lett.* 92 (8 2004), p. 086102. DOI: 10.1103/PhysRevLett.92.086102. URL: https://link.aps.org/doi/10.1103/PhysRevLett.92.086102.

[40] V. Pankoke, P. Kratzer, and S. Sakong. "Calculation of the diameter-dependent polytypism in GaAs nanowires from an atomic motif expansion of the formation energy". In: *Phys. Rev. B* 84 (7 2011), p. 075455. DOI: 10.1103/PhysRevB.84.075455. URL: https://link.aps.org/doi/10.1103/PhysRevB.84.075455.

[41] T. Einstein. "5 - Equilibrium Shape of Crystals". In: *Handbook of Crystal Growth (Second Edition)*. Ed. by T. Nishinaga. Second Edition. Boston: Elsevier, 2015, pp. 215–264. ISBN: 978-0-444-56369-9. DOI: https://doi.org/10.1016/B978-0-444-56369-9.00005-8. URL: https://www.sciencedirect.com/science/article/pii/B9780444563699000058.

[42] W. Winterbottom. "Equilibrium shape of a small particle in contact with a foreign substrate". In: *Acta Metallurgica* 15.2 (1967), pp. 303–310. ISSN: 0001-6160. DOI: https://doi.org/10.1016/0001-6160(67)90206-4. URL: https://www.sciencedirect.com/science/article/pii/0001616067902064.

[43] C. Boukouvala, J. Daniel, and E. Ringe. "Approaches to modelling the shape of nanocrystals". In: *Nano Convergence* 8.1 (2021). DOI: 10.1186/s40580-021-00275-6. URL: https://doi.org/10.1186/s40580-021-00275-6.

[44] T. Nishinaga. "23 - Nucleation and Surface Diffusion in Molecular Beam Epitaxy". In: *Handbook of Crystal Growth (Second Edition)*. Ed. by T. F. Kuech. Second Edition. Handbook of Crystal Growth. Boston: North-Holland, 2015, pp. 943–982. ISBN: 978-0-444-63304-0. DOI: https://doi.org/10.1016/B978-0-444-63304-0.00023-8. URL: https://www.sciencedirect.com/science/article/pii/B9780444633040000238.

[45] G. Ehrlich and F. G. Hudda. "Atomic View of Surface Self-Diffusion: Tungsten on Tungsten". In: *The Journal of Chemical Physics* 44.3 (2004), pp. 1039–1049. ISSN: 0021-9606. DOI: 10.1063/1.1726787. eprint: https://pubs.aip.org/aip/jcp/article-pdf/44/3/1039/11259582/1039_1_online.pdf. URL: https://doi.org/10.1063/1.1726787.

[46] R. L. Schwoebel. "Step Motion on Crystal Surfaces. II". In: *Journal of Applied Physics* 40.2 (1969), pp. 614–618. DOI: 10.1063/1.1657442.

[47] T. Ihn. *Semiconductor Nanostructures: Quantum States and Electronic Transport*. OUP Oxford, 2010. ISBN: 9780199534425. URL: https://books.google.dk/books?id=PAtqPgAACAAJ.

[48] Y. Horikosh. "Chapter 2 - Migration-enhanced Epitaxy for Low-dimensional Structures". In: *Molecular Beam Epitaxy (Second Edition)*. Ed. by M. Henini. Second Edition. Elsevier, 2018, pp. 27–36. ISBN: 978-0-12-812136-8. DOI: https://doi.org/10.1016/

B978-0-12-812136-8.00002-5. URL: https://www.sciencedirect.com/science/article/pii/B9780128121368000025.

[49] P. Aseev, A. Fursina, F. Boekhout, F. Krizek, J. E. Sestoft, F. Borsoi, S. Heedt, G. Wang, L. Binci, S. Martí-Sánchez, T. Swoboda, R. Koops, E. Uccelli, J. Arbiol, P. Krogstrup, L. P. Kouwenhoven, and P. Caroff. "Selectivity Map for Molecular Beam Epitaxy of Advanced III–V Quantum Nanowire Networks". In: *Nano Letters* 19.1 (2019). PMID: 30521341, pp. 218–227. DOI: 10.1021/acs.nanolett.8b03733. eprint: https://doi.org/10.1021/acs.nanolett.8b03733. URL: https://doi.org/10.1021/acs.nanolett.8b03733.

[50] M. Hata, A. Watanabe, and T. Isu. "Surface diffusion length observed by in situ scanning microprobe reflection high-energy electron diffraction". In: *Journal of Crystal Growth* 111.1 (1991), pp. 83–87. ISSN: 0022-0248. DOI: https://doi.org/10.1016/0022-0248(91)90951-Z. URL: https://www.sciencedirect.com/science/article/pii/002202489190951Z.

[51] T. Yamamura, T. Matsushita, T. Koitabashi, and T. Kondo. "Influence of Anisotropic Diffusion of Ga Atoms on GaAs Growth on Alternately Inverted (100) Substrates". In: *Japanese Journal of Applied Physics* 44.11L (2005), p. L1397. DOI: 10.1143/JJAP.44.L1397. URL: https://dx.doi.org/10.1143/JJAP.44.L1397.

[52] J. L. Roehl, A. Kolagatla, V. K. K. Ganguri, S. V. Khare, and R. J. Phaneuf. "Binding sites and diffusion barriers of a Ga adatom on the GaAs(001)$-c(4\times4)$ surface from first-principles computations". In: *Phys. Rev. B* 82 (16 2010), p. 165335. DOI: 10.1103/PhysRevB.82.165335. URL: https://link.aps.org/doi/10.1103/PhysRevB.82.165335.

[53] M. Mińkowski and M. A. Załuska–Kotur. "Diffusion of Ga adatoms at the surface of GaAs(001) $c(4\times4)\alpha$ and β reconstructions". In: *Phys. Rev. B* 91 (7 2015), p. 075411. DOI: 10.1103/PhysRevB.91.075411. URL: https://link.aps.org/doi/10.1103/PhysRevB.91.075411.

[54] F. Fathi Aghdam, H. Liao, and Q. Huang. "Modeling Interaction in Nanowire Growth Process Toward Improved Yield". In: *IEEE Transactions on Automation Science and Engineering* 14.2 (2017), pp. 1139–1149. DOI: 10.1109/TASE.2015.2499210.

[55] Y. Y. Hervieu. "Effective diffusion length and elementary surface processes in the concurrent growth of nanowires and 2D layers". In: *Journal of Crystal Growth* 493 (2018), pp. 1–7. ISSN: 0022-0248. DOI: https://doi.org/10.1016/j.jcrysgro.2018.04.012. URL: https://www.sciencedirect.com/science/article/pii/S0022024818301787.

[56] V. G. Dubrovskii, W. Kim, V. Piazza, L. Güniat, and A. Fontcuberta i Morral. "Simultaneous Selective Area Growth of Wurtzite and Zincblende Self-Catalyzed GaAs Nanowires on Silicon". In: *Nano Letters* 21.7 (2021). PMID: 33818097, pp. 3139–3145. DOI: 10.1021/acs.nanolett.1c00349. eprint: https://doi.org/10.1021/acs.nanolett.1c00349. URL: https://doi.org/10.1021/acs.nanolett.1c00349.

[57] V. Dubrovskii. "Vapor–Liquid–Solid Growth of Nanowires". In: 2014, pp. 275–395. ISBN: 978-3-642-39659-5. DOI: 10.1007/978-3-642-39660-1_4.

[58] A. Rothman, J. Maniš, V. G. Dubrovskii, T. Šikola, J. Mach, and E. Joselevich. "Kinetics of Guided Growth of Horizontal GaN Nanowires on Flat and Faceted Sapphire Surfaces". In: *Nanomaterials* 11.3 (2021). ISSN: 2079-4991. DOI: 10.3390/nano11030624. URL: https://www.mdpi.com/2079-4991/11/3/624.

[59] T. M. Inc. *MATLAB version: 9.13.0 (R2022b)*. Natick, Massachusetts, United States, 2022. URL: https://www.mathworks.com.

[60] T. C. T. Nikolajsen. *Critical Heights and Phenomenology of Dislocations in Selective Area Growth: Investigating Nanowires with FEM*. eng. 2022.

[61] H. Wang, S. Feng, H. Zhu, D. Ning, F. Chen, and X. Wang. "Electronic characteristics of InAs self-assembled quantum dots". In: *Physica E: Low-dimensional Systems and Nanostructures* 7.3 (2000), pp. 383–387. ISSN: 1386-9477. DOI: https://doi.org/10.1016/S1386-9477(99)00346-X. URL: https://www.sciencedirect.com/science/article/pii/S138694779900346X.

[62] M. Jung, K. Hirakawa, Y. Kawaguchi, S. Komiyama, S. Ishida, and Y. Arakawa. "Lateral electron transport through single self-assembled InAs quantum dots". In: *Applied Physics Letters* 86.3 (2005), p. 033106. ISSN: 0003-6951. DOI: 10.1063/1.1853516. eprint: https://pubs.aip.org/aip/apl/article-pdf/doi/10.1063/1.1853516/14322686/033106_1_online.pdf. URL: https://doi.org/10.1063/1.1853516.

[63] Y. Kanai, R. S. Deacon, S. Takahashi, A. Oiwa, K. Yoshida, K. Shibata, K. Hirakawa, Y. Tokura, and S. Tarucha. "Electrically tuned spin–orbit interaction in an InAs self-assembled quantum dot". In: *Nature Nanotechnology* 6.8 (2011), pp. 511–516. ISSN: 1748-3395. DOI: 10.1038/nnano.2011.103. URL: https://doi.org/10.1038/nnano.2011.103.

[64] M. Al Huwayz, H. Galeti, O. Lemine, K. Ibnaouf, A. Alkaoud, Y. Alaskar, A. Salhi, S. Alhassan, S. Alotaibi, A. Almalki, A. Almunyif, A. Alhassni, D. Jameel, Y. G. Gobato, and M. Henini. "Optical properties of self-assembled InAs quantum dots based P–I–N structures

grown on GaAs and Si substrates by Molecular Beam Epitaxy". In: *Journal of Luminescence* 251 (2022), p. 119155. ISSN: 0022-2313. DOI: https://doi.org/10.1016/j.jlumin.2022.119155. URL: https://www.sciencedirect.com/science/article/pii/S0022231322004306.

[65] K. O. K. Okajima, K. T. K. Takeda, N. O. N. Oyama, E. O. E. Ohta, K. S. K. Shiraishi, and T. O. T. Ohno. "Phenomenological Theory of Semiconductor Epitaxial Growth with Misfit-Dislocations". In: *Japanese Journal of Applied Physics* 39.9A (2000), p. L917. DOI: 10.1143/JJAP.39.L917. URL: https://dx.doi.org/10.1143/JJAP.39.L917.

[66] K. Shiraishi, N. Oyama, K. Okajima, N. Miyagishima, K. Takeda, H. Yamaguchi, T. Ito, and T. Ohno. "First principles and macroscopic theories of semiconductor epitaxial growth". English. In: *Journal of Crystal Growth* 237-239.1 4 I (2002). Funding Information: We would like to thank Professor K. Nakajima and Professor H. Nakayama for their stimulating discussions. We also thank Dr. K. Murase and Dr. Y. Takahashi for their useful advice. This work was partly supported by JSPS under Contract No. RFT96P00203 and the Grant-in-Aid for Scientific Research by the Ministry of Education, Science and Culture of Japan and the NEDO International Joint Research Grant., pp. 206–211. ISSN: 0022-0248. DOI: 10.1016/S0022-0248(01)01903-0.

[67] F. Tinjod and H. Mariette. "Self-assembled quantum dot formation induced by surface energy change of a strained two-dimensional layer". In: *physica status solidi (b)* 241.3 (2004), pp. 550–557. DOI: https://doi.org/10.1002/pssb.200304300. eprint: https://onlinelibrary.wiley.com/doi/pdf/10.1002/pssb.200304300. URL: https://onlinelibrary.wiley.com/doi/abs/10.1002/pssb.200304300.

[68] T. Young. "III. An essay on the cohesion of fluids". In: *Philosophical Transactions of the Royal Society of London* 95 (1805), pp. 65–87. DOI: 10.1098/rstl.1805.0005. eprint: https://royalsocietypublishing.org/doi/pdf/10.1098/rstl.1805.0005. URL: https://royalsocietypublishing.org/doi/abs/10.1098/rstl.1805.0005.

[69] P. Müller and R. Kern. "Equilibrium nano-shape changes induced by epitaxial stress (generalised Wulf–Kaishew theorem)". In: *Surface Science* 457.1 (2000), pp. 229–253. ISSN: 0039-6028. DOI: https://doi.org/10.1016/S0039-6028(00)00371-X. URL: https://www.sciencedirect.com/science/article/pii/S003960280000371X.

[70] J. Wu and P. Jin. "Self-assembly of InAs quantum dots on GaAs(001) by molecular beam epitaxy". In: *Frontiers of Physics* 10.1 (2015),

pp. 7–58. ISSN: 2095-0470. DOI: 10.1007/s11467-014-0422-4. URL: https://doi.org/10.1007/s11467-014-0422-4.

[71] D. J. DUNSTAN. "Strain and strain relaxation in semiconductors". In: *Journal of Materials Science: Materials in Electronics* 8.6 (1997), pp. 337–375. ISSN: 1573-482X. DOI: 10.1023/A:1018547625106. URL: https://doi.org/10.1023/A:1018547625106.

[72] F. C. Frank, J. H. van der Merwe, and N. F. Mott. "One-dimensional dislocations. I. Static theory". In: *Proceedings of the Royal Society of London. Series A. Mathematical and Physical Sciences* 198.1053 (1949), pp. 205–216. DOI: 10.1098/rspa.1949.0095. eprint: https://royalsocietypublishing.org/doi/pdf/10.1098/rspa.1949.0095. URL: https://royalsocietypublishing.org/doi/abs/10.1098/rspa.1949.0095.

[73] J. H. Van Der Merwe. "Crystal Interfaces. Part I. Semi-Infinite Crystals". In: *Journal of Applied Physics* 34.1 (2004), pp. 117–122. ISSN: 0021-8979. DOI: 10.1063/1.1729050. eprint: https://pubs.aip.org/aip/jap/article-pdf/34/1/117/7931618/117_1_online.pdf. URL: https://doi.org/10.1063/1.1729050.

[74] J. H. Van Der Merwe. "Crystal Interfaces. Part II. Finite Overgrowths". In: *Journal of Applied Physics* 34.1 (2004), pp. 123–127. ISSN: 0021-8979. DOI: 10.1063/1.1729050. eprint: https://pubs.aip.org/aip/jap/article-pdf/34/1/123/7931634/123_1_online.pdf. URL: https://doi.org/10.1063/1.1729051.

[75] J. W. Matthews, S. Mader, and T. B. Light. "Accommodation of Misfit Across the Interface Between Crystals of Semiconducting Elements or Compounds". In: *Journal of Applied Physics* 41.9 (2003), pp. 3800–3804. ISSN: 0021-8979. DOI: 10.1063/1.1659510. eprint: https://pubs.aip.org/aip/jap/article-pdf/41/9/3800/7946151/3800_1_online.pdf. URL: https://doi.org/10.1063/1.1659510.

[76] J. Matthews and A. Blakeslee. "Defects in epitaxial multilayers: I. Misfit dislocations". In: *Journal of Crystal Growth* 27 (1974), pp. 118–125. ISSN: 0022-0248. DOI: https://doi.org/10.1016/S0022-0248(74)80055-2. URL: https://www.sciencedirect.com/science/article/pii/S0022024874800552.

[77] N. Grandjean, J. Massies, and V. H. Etgens. "Delayed relaxation by surfactant action in highly strained III-V semiconductor epitaxial layers". In: *Phys. Rev. Lett.* 69 (5 1992), pp. 796–799. DOI: 10.1103/PhysRevLett.69.796. URL: https://link.aps.org/doi/10.1103/PhysRevLett.69.796.

[78] A. Sasaki. “Initial growth layers and critical thickness of InAs heteroepitaxy on GaAs substrates”. In: *Journal of Crystal Growth* 160.1 (1996), pp. 27–35. ISSN: 0022-0248. DOI: https://doi.org/10.1016/0022-0248(95)00472-6. URL: https://www.sciencedirect.com/science/article/pii/0022024895004726.

[79] E. Fitzgerald. “Dislocations in strained-layer epitaxy: theory, experiment, and applications”. In: *Materials Science Reports* 7.3 (1991), pp. 87–142. ISSN: 0920-2307. DOI: https://doi.org/10.1016/0920-2307(91)90006-9. URL: https://www.sciencedirect.com/science/article/pii/0920230791900069.

[80] R. People and J. C. Bean. “Calculation of critical layer thickness versus lattice mismatch for GexSi1-x/Si strained-layer heterostructures”. In: *Applied Physics Letters* 47.3 (1985), pp. 322–324. ISSN: 0003-6951. DOI: 10.1063/1.96206. eprint: https://pubs.aip.org/aip/apl/article-pdf/47/3/322/7756891/322_1_online.pdf. URL: https://doi.org/10.1063/1.96206.

[81] B. W. Dodson and J. Y. Tsao. “Relaxation of strained-layer semiconductor structures via plastic flow”. In: *Applied Physics Letters* 51.17 (1987), pp. 1325–1327. ISSN: 0003-6951. DOI: 10.1063/1.98667. eprint: https://pubs.aip.org/aip/apl/article-pdf/51/17/1325/7763218/1325_1_online.pdf. URL: https://doi.org/10.1063/1.98667.

[82] G. J. Whaley and P. I. Cohen. “Summary Abstract: The growth of strained InGaAs on GaAs: Kinetics versus energetics”. In: *Journal of Vacuum Science & Technology B: Microelectronics Processing and Phenomena* 6.2 (1988), pp. 625–626. ISSN: 0734-211X. DOI: 10.1116/1.584416. eprint: https://pubs.aip.org/avs/jvb/article-pdf/6/2/625/11981324/625_1_online.pdf. URL: https://doi.org/10.1116/1.584416.

[83] G. J. Whaley and P. I. Cohen. “Relaxation of strained InGaAs during molecular beam epitaxy”. In: *Applied Physics Letters* 57.2 (1990), pp. 144–146. ISSN: 0003-6951. DOI: 10.1063/1.103966. eprint: https://pubs.aip.org/aip/apl/article-pdf/57/2/144/7777528/144_1_online.pdf. URL: https://doi.org/10.1063/1.103966.

[84] P. M. J. Marée, J. C. Barbour, J. F. van der Veen, K. L. Kavanagh, C. W. T. Bulle-Lieuwma, and M. P. A. Viegers. “Generation of misfit dislocations in semiconductors”. In: *Journal of Applied Physics* 62.11 (1987), pp. 4413–4420. ISSN: 0021-8979. DOI: 10.1063/1.339078. eprint: https://pubs.aip.org/aip/jap/article-pdf/62/11/4413/7996841/4413_1_online.pdf. URL: https://doi.org/10.1063/1.339078.

[85] E. Placidi, F. Arciprete, R. Magri, M. Rosini, A. Vinattieri, L. Cavigli, M. Gurioli, E. Giovine, L. Persichetti, M. Fanfoni, F. Patella, and A. Balzarotti. "InAs Epitaxy on GaAs(001): A Model Case of Strain-Driven Self-assembling of Quantum Dots". In: *Self-Assembly of Nanostructures: The INFN Lectures, Vol. III*. Ed. by S. Bellucci. New York, NY: Springer New York, 2012, pp. 73–125. ISBN: 978-1-4614-0742-3. DOI: 10.1007/978-1-4614-0742-3_2. URL: https://doi.org/10.1007/978-1-4614-0742-3_2.

[86] P. B. Joyce, T. J. Krzyzewski, G. R. Bell, B. A. Joyce, and T. S. Jones. "Composition of InAs quantum dots on GaAs(001): Direct evidence for (In,Ga)As alloying". In: *Phys. Rev. B* 58 (24 1998), R15981–R15984. DOI: 10.1103/PhysRevB.58.R15981. URL: https://link.aps.org/doi/10.1103/PhysRevB.58.R15981.

[87] M. Friedl, K. Cerveny, P. Weigele, G. Tütüncüoglu, S. Martí-Sánchez, C. Huang, T. Patlatiuk, H. Potts, Z. Sun, M. O. Hill, L. Güniat, W. Kim, M. Zamani, V. G. Dubrovskii, J. Arbiol, L. J. Lauhon, D. M. Zumbühl, and A. Fontcuberta i Morral. "Template-Assisted Scalable Nanowire Networks". In: *Nano Letters* 18.4 (2018). PMID: 29579392, pp. 2666–2671. DOI: 10.1021/acs.nanolett.8b00554. eprint: https://doi.org/10.1021/acs.nanolett.8b00554. URL: https://doi.org/10.1021/acs.nanolett.8b00554.

[88] M. Friedl, K. Cerveny, C. Huang, D. Dede, M. Samani, M. O. Hill, N. Morgan, W. Kim, L. Güniat, J. Segura-Ruiz, L. J. Lauhon, D. M. Zumbühl, and A. Fontcuberta i Morral. "Remote Doping of Scalable Nanowire Branches". In: *Nano Letters* 20.5 (2020). PMID: 32315191, pp. 3577–3584. DOI: 10.1021/acs.nanolett.0c00517. eprint: https://doi.org/10.1021/acs.nanolett.0c00517. URL: https://doi.org/10.1021/acs.nanolett.0c00517.

[89] D. V. Beznasyuk, S. Martí-Sánchez, J.-H. Kang, R. Tanta, M. Rajpalke, T. š. Stankevi č, A. W. Christensen, M. C. Spadaro, R. Bergamaschini, N. N. Maka, C. E. N. Petersen, D. J. Carrad, T. S. Jespersen, J. Arbiol, and P. Krogstrup. "Doubling the mobility of InAs/InGaAs selective area grown nanowires". In: *Phys. Rev. Mater.* 6 (3 2022), p. 034602. DOI: 10.1103/PhysRevMaterials.6.034602. URL: https://link.aps.org/doi/10.1103/PhysRevMaterials.6.034602.

[90] W. J. Schaffer, M. D. Lind, S. P. Kowalczyk, and R. W. Grant. "Nucleation and strain relaxation at the InAs/GaAs(100) heterojunction". In: *Journal of Vacuum Science & Technology B: Microelectronics Processing and Phenomena* 1.3 (1983), pp. 688–695. ISSN: 0734-211X. DOI: 10.1116/1.582579. eprint: https://pubs.aip.org/avs/jvb/article-pdf/1/3/688/11783308/688_1_online.pdf. URL: https://doi.org/10.1116/1.582579.

[91] E. Tournié, A. Trampert, and K. H. Ploog. “Interplay between Surface Stabilization, Growth Mode and Strain Relaxation during Molecular-Beam Epitaxy of Highly Mismatched III-V Semiconductor Layers”. In: *Europhysics Letters* 25.9 (1994), p. 663. DOI: 10.1209/0295-5075/25/9/005. URL: https://dx.doi.org/10.1209/0295-5075/25/9/005.

[92] A. Trampert, E. Tournié, and K. Ploog. “Defect control during growth of highly mismatched (100) InAsGaAs-heterostructures”. In: *Journal of Crystal Growth* 146.1 (1995). Vapour Growth and Epitaxy 1994, pp. 368–373. ISSN: 0022-0248. DOI: https://doi.org/10.1016/0022-0248(94)00535-4. URL: https://www.sciencedirect.com/science/article/pii/0022024894005354.

[93] C. W. Snyder and B. G. Orr. “Comment on “Delayed relaxation by surfactant action in highly strained III-V semiconductor epitaxial layers””. In: *Phys. Rev. Lett.* 70 (7 1993), pp. 1030–1030. DOI: 10.1103/PhysRevLett.70.1030. URL: https://link.aps.org/doi/10.1103/PhysRevLett.70.1030.

[94] E. Placidi, F. Arciprete, V. Sessi, M. Fanfoni, F. Patella, and A. Balzarotti. “Step erosion during nucleation of InAs/GaAs(001) quantum dots”. In: *Applied Physics Letters* 86.24 (2005), p. 241913. ISSN: 0003-6951. DOI: 10.1063/1.1946181. eprint: https://pubs.aip.org/aip/apl/article-pdf/doi/10.1063/1.1946181/13932039/241913_1_online.pdf. URL: https://doi.org/10.1063/1.1946181.

[95] F. Patella, F. Arciprete, M. Fanfoni, V. Sessi, A. Balzarotti, and E. Placidi. “Reflection high energy electron diffraction observation of surface mass transport at the two- to three-dimensional growth transition of InAs on GaAs(001)”. In: *Applied Physics Letters* 87.25 (2005), p. 252101. ISSN: 0003-6951. DOI: 10.1063/1.2147731. eprint: https://pubs.aip.org/aip/apl/article-pdf/doi/10.1063/1.2147731/14651776/252101_1_online.pdf. URL: https://doi.org/10.1063/1.2147731.

[96] F. Arciprete, E. Placidi, V. Sessi, M. Fanfoni, F. Patella, and A. Balzarotti. “How kinetics drives the two- to three-dimensional transition in semiconductor strained heterostructures: The case of InAs/GaAs(001)”. In: *Applied Physics Letters* 89.4 (2006), p. 041904. ISSN: 0003-6951. DOI: 10.1063/1.2234845. eprint: https://pubs.aip.org/aip/apl/article-pdf/doi/10.1063/1.2234845/13160168/041904_1_online.pdf. URL: https://doi.org/10.1063/1.2234845.

[97] F. Houzay, C. Guille, J. Moison, P. Henoc, and F. Barthe. “First stages of the MBE growth of InAs on (001)GaAs”. In: *Journal of Crystal Growth* 81.1 (1987), pp. 67–72. ISSN: 0022-0248. DOI: https://doi.

org/10.1016/0022-0248(87)90367-8. URL: https://www.sciencedirect.com/science/article/pii/0022024887903678.

[98] F. Glas, C. Guille, P. Hénoc, and F. Houzay. "TEM study of the molecular beam epitaxy island growth of InAs on GaAs". In: 2020, pp. 71–76. ISBN: 9781003069621. DOI: 10.1201/9781003069621-11.

[99] A. Mazuelas, L. González, F. Ponce, L. Tapfer, and F. Briones. "Critical thickness determination of InAs, InP and GaP on GaAs by X-ray interference effect and transmission electron microscopy". In: *Journal of Crystal Growth* 131.3 (1993), pp. 465–469. ISSN: 0022-0248. DOI: https://doi.org/10.1016/0022-0248(93)90197-5. URL: https://www.sciencedirect.com/science/article/pii/0022024893901975.

[100] D. Leonard, K. Pond, and P. M. Petroff. "Critical layer thickness for self-assembled InAs islands on GaAs". In: *Phys. Rev. B* 50 (16 1994), pp. 11687–11692. DOI: 10.1103/PhysRevB.50.11687. URL: https://link.aps.org/doi/10.1103/PhysRevB.50.11687.

[101] S. Guha, A. Madhukar, and K. C. Rajkumar. "Onset of incoherency and defect introduction in the initial stages of molecular beam epitaxical growth of highly strained InxGa1-xAs on GaAs(100)". In: *Applied Physics Letters* 57.20 (1990), pp. 2110–2112. ISSN: 0003-6951. DOI: 10.1063/1.103914. eprint: https://pubs.aip.org/aip/apl/article-pdf/57/20/2110/8996114/2110_1_online.pdf. URL: https://doi.org/10.1063/1.103914.

[102] S. Guha, A. Madhukar, R. Kapre, and K. C. Rajkumar. "Initial Stages of Molecular Beam Epitaxical Growth of Highly Strained InxGa1-XAs on GaAs (100)". In: *MRS Online Proceedings Library* 202.1 (1990), pp. 519–524. ISSN: 1946-4274. DOI: 10.1557/PROC-202-519. URL: https://doi.org/10.1557/PROC-202-519.

[103] S. Guha, A. Madhukar, L.-p. Chen, K. C. Rajkumar, and R. M. Kapre. "Interfacet migration and defect formation in heteroepitaxy on patterned substrates: AlGaAs and InGaAs on GaAs (100) in MBE". In: *Growth of Semiconductor Structures and High-Tc Thin Films on Semiconductors*. Ed. by A. Madhukar. Vol. 1285. International Society for Optics and Photonics. SPIE, 1990, pp. 160–169. DOI: 10.1117/12.20817. URL: https://doi.org/10.1117/12.20817.

[104] C. W. Snyder, B. G. Orr, D. Kessler, and L. M. Sander. "Effect of strain on surface morphology in highly strained InGaAs films". In: *Phys. Rev. Lett.* 66 (23 1991), pp. 3032–3035. DOI: 10.1103/PhysRevLett.66.3032. URL: https://link.aps.org/doi/10.1103/PhysRevLett.66.3032.

[105] B. F. Lewis, T. C. Lee, F. J. Grunthaner, A. Madhukar, R. Fernandez, and J. Maserjian. "RHEED oscillation studies of MBE growth kinetics and lattice mismatch strain-induced effects during InGaAs growth on GaAs(100)". In: *Journal of Vacuum Science & Technology B: Microelectronics Processing and Phenomena* 2.3 (1984), pp. 419–424. ISSN: 0734-211X. DOI: 10.1116/1.582887. eprint: https://pubs.aip.org/avs/jvb/article-pdf/2/3/419/11613858/419_1_online.pdf. URL: https://doi.org/10.1116/1.582887.

[106] H. Nakao and T. Yao. "Surface Lattice Strain Relaxation at the Initial Stage of Heteroepitaxial Growth of InxGa1-xAs on GaAs by Molecular Beam Epitaxy". In: *Japanese Journal of Applied Physics* 28.3A (1989), p. L352. DOI: 10.1143/JJAP.28.L352. URL: https://dx.doi.org/10.1143/JJAP.28.L352.

[107] B. Elman, E. S. Koteles, P. Melman, C. Jagannath, J. Lee, and D. Dugger. "In-situ measurements of critical layer thickness and optical studies of InGaAs quantum wells grown on GaAs substrates". In: *Applied Physics Letters* 55.16 (1989), pp. 1659–1661. ISSN: 0003-6951. DOI: 10.1063/1.102279. eprint: https://pubs.aip.org/aip/apl/article-pdf/55/16/1659/7772109/1659_1_online.pdf. URL: https://doi.org/10.1063/1.102279.

[108] B. Elman, E. S. Koteles, P. Melman, K. Ostreicher, and C. Sung. "Low substrate temperature molecular beam epitaxial growth and the critical layer thickness of InGaAs grown on GaAs". In: *Journal of Applied Physics* 70.5 (1991), pp. 2634–2640. ISSN: 0021-8979. DOI: 10.1063/1.349376. eprint: https://pubs.aip.org/aip/jap/article-pdf/70/5/2634/7509392/2634_1_online.pdf. URL: https://doi.org/10.1063/1.349376.

[109] J. Y. Yao, T. G. Andersson, and G. L. Dunlop. "The interfacial morphology of strained epitaxial InxGa1-xAs/GaAs". In: *Journal of Applied Physics* 69.4 (1991), pp. 2224–2230. ISSN: 0021-8979. DOI: 10.1063/1.348700. eprint: https://pubs.aip.org/aip/jap/article-pdf/69/4/2224/9047590/2224_1_online.pdf. URL: https://doi.org/10.1063/1.348700.

[110] J. Zou, D. J. H. Cockayne, and B. F. Usher. "Misfit dislocations and critical thickness in InGaAs/GaAs heterostructure systems". In: *Journal of Applied Physics* 73.2 (1993), pp. 619–626. ISSN: 0021-8979. DOI: 10.1063/1.353372. eprint: https://pubs.aip.org/aip/jap/article-pdf/73/2/619/8030737/619_1_online.pdf. URL: https://doi.org/10.1063/1.353372.

[111] D. I. Westwood, D. A. Woolf, A. Vilà, A. Cornet, and J. R. Morante. "Influence of mismatch on the defects in relaxed epitaxial InGaAs/GaAs(100) films grown by molecular beam epitaxy". In: *Journal of Applied Physics* 74.3 (1993), pp. 1731–1735. ISSN: 0021-8979. DOI: 10.1063/

1.354827. eprint: https://pubs.aip.org/aip/jap/article-pdf/74/3/1731/8032358/1731_1_online.pdf. URL: https://doi.org/10.1063/1.354827.

[112] J. W. Matthews. "Defects associated with the accommodation of misfit between crystals". In: *Journal of Vacuum Science and Technology* 12.1 (1975), pp. 126–133. ISSN: 0022-5355. DOI: 10.1116/1.568741. eprint: https://pubs.aip.org/avs/jvst/article-pdf/12/1/126/12208636/126_1_online.pdf. URL: https://doi.org/10.1116/1.568741.

[113] J. H. van der Merwe. "Misfit dislocation generation in epitaxial layers". In: *Critical Reviews in Solid State and Materials Sciences* 17.3 (1991), pp. 187–209. DOI: 10.1080/10408439108243751. eprint: https://doi.org/10.1080/10408439108243751. URL: https://doi.org/10.1080/10408439108243751.

[114] J. Y. Tsao, B. W. Dodson, S. T. Picraux, and D. M. Cornelison. "Critical Stresses for Si_xGe_{1-x} Strained-Layer Plasticity". In: *Phys. Rev. Lett.* 59 (21 1987), pp. 2455–2458. DOI: 10.1103/PhysRevLett.59.2455. URL: https://link.aps.org/doi/10.1103/PhysRevLett.59.2455.

[115] F. Krizek, J. E. Sestoft, P. Aseev, S. Marti-Sanchez, S. Vaitiek ėnas, L. Casparis, S. A. Khan, Y. Liu, T. š. Stankevi č, A. M. Whiticar, A. Fursina, F. Boekhout, R. Koops, E. Uccelli, L. P. Kouwenhoven, C. M. Marcus, J. Arbiol, and P. Krogstrup. "Field effect enhancement in buffered quantum nanowire networks". In: *Phys. Rev. Mater.* 2 (9 2018), p. 093401. DOI: 10.1103/PhysRevMaterials.2.093401. URL: https://link.aps.org/doi/10.1103/PhysRevMaterials.2.093401.

[116] S. Vaitiek ėnas, A. M. Whiticar, M.-T. Deng, F. Krizek, J. E. Sestoft, C. J. Palmstrøm, S. Marti-Sanchez, J. Arbiol, P. Krogstrup, L. Casparis, and C. M. Marcus. "Selective-Area-Grown Semiconductor-Superconductor Hybrids: A Basis for Topological Networks". In: *Phys. Rev. Lett.* 121 (14 2018), p. 147701. DOI: 10.1103/PhysRevLett.121.147701. URL: https://link.aps.org/doi/10.1103/PhysRevLett.121.147701.

[117] J. S. Lee, S. Choi, M. Pendharkar, D. J. Pennachio, B. Markman, M. Seas, S. Koelling, M. A. Verheijen, L. Casparis, K. D. Petersson, I. Petkovic, V. Schaller, M. J. W. Rodwell, C. M. Marcus, P. Krogstrup, L. P. Kouwenhoven, E. P. A. M. Bakkers, and C. J. Palmstrøm. "Selective-area chemical beam epitaxy of in-plane InAs one-dimensional channels grown on InP(001), InP(111)B, and InP(011) surfaces". In: *Phys. Rev. Mater.* 3 (8 2019), p. 084606. DOI: 10.1103/PhysRevMaterials.3.084606. URL: https://link.aps.org/doi/10.1103/PhysRevMaterials.3.084606.

[118] M. Friedl, K. Cerveny, P. Weigele, G. Tütüncüoglu, S. Martí-Sánchez, C. Huang, T. Patlatiuk, H. Potts, Z. Sun, M. O. Hill, L. Güniat, W. Kim, M. Zamani, V. G. Dubrovskii, J. Arbiol, L. J. Lauhon, D. M. Zumbühl, and A. Fontcuberta i Morral. "Template-Assisted Scalable Nanowire Networks". In: *Nano Letters* 18.4 (2018). PMID: 29579392, pp. 2666–2671. DOI: 10.1021/acs.nanolett.8b00554. eprint: https://doi.org/10.1021/acs.nanolett.8b00554. URL: https://doi.org/10.1021/acs.nanolett.8b00554.

[119] M. Fahed, L. Desplanque, D. Troadec, G. Patriarche, and X. Wallart. "Selective area heteroepitaxy of GaSb on GaAs (001) for in-plane InAs nanowire achievement". In: *Nanotechnology* 27.50 (2016), p. 505301. DOI: 10.1088/0957-4484/27/50/505301. URL: https://dx.doi.org/10.1088/0957-4484/27/50/505301.

[120] L. Desplanque, M. Fahed, X. Han, V. K. Chinni, D. Troadec, M.-P. Chauvat, P. Ruterana, and X. Wallart. "Influence of nanoscale faceting on the tunneling properties of near broken gap InAs/AlGaSb heterojunctions grown by selective area epitaxy". In: *Nanotechnology* 25.46 (2014), p. 465302. DOI: 10.1088/0957-4484/25/46/465302. URL: https://dx.doi.org/10.1088/0957-4484/25/46/465302.

[121] R. L. M. Op het Veld, D. Xu, V. Schaller, M. A. Verheijen, S. M. E. Peters, J. Jung, C. Tong, Q. Wang, M. W. A. de Moor, B. Hesselmann, K. Vermeulen, J. D. S. Bommer, J. Sue Lee, A. Sarikov, M. Pendharkar, A. Marzegalli, S. Koelling, L. P. Kouwenhoven, L. Miglio, C. J. Palmstrøm, H. Zhang, and E. P. A. M. Bakkers. "In-plane selective area InSb–Al nanowire quantum networks". In: *Communications Physics* 3.1 (2020), p. 59. ISSN: 2399-3650. DOI: 10.1038/s42005-020-0324-4. URL: https://doi.org/10.1038/s42005-020-0324-4.

[122] B. Ohlsson, M. Björk, A. Persson, C. Thelander, L. Wallenberg, M. Magnusson, K. Deppert, and L. Samuelson. "Growth and characterization of GaAs and InAs nano-whiskers and InAs/GaAs heterostructures". In: *Physica E: Low-dimensional Systems and Nanostructures* 13.2 (2002), pp. 1126–1130. ISSN: 1386-9477. DOI: https://doi.org/10.1016/S1386-9477(02)00318-1. URL: https://www.sciencedirect.com/science/article/pii/S1386947702003181.

[123] K. L. Kavanagh, I. Saveliev, M. Blumin, G. Swadener, and H. E. Ruda. "Faster radial strain relaxation in InAs–GaAs core–shell heterowires". In: *Journal of Applied Physics* 111.4 (2012), p. 044301. ISSN: 0021-8979. DOI: 10.1063/1.3684964. eprint: https://pubs.aip.org/aip/jap/article-pdf/doi/10.1063/1.3684964/15084681/044301_1_online.pdf. URL: https://doi.org/10.1063/1.3684964.

[124] A. Biermanns, T. Rieger, G. Bussone, U. Pietsch, D. Grützmacher, and M. Ion Lepsa. "Axial strain in GaAs/InAs core-shell nanowires". In: *Applied Physics Letters* 102.4 (2013), p. 043109. ISSN: 0003-6951. DOI: 10.1063/1.4790185. eprint: https://pubs.aip.org/aip/apl/article-pdf/doi/10.1063/1.4790185/13565604/043109_1_online.pdf. URL: https://doi.org/10.1063/1.4790185.

[125] E. Ertekin, P. A. Greaney, D. C. Chrzan, and T. D. Sands. "Equilibrium limits of coherency in strained nanowire heterostructures". In: *Journal of Applied Physics* 97.11 (2005), p. 114325. ISSN: 0021-8979. DOI: 10.1063/1.1903106. eprint: https://pubs.aip.org/aip/jap/article-pdf/doi/10.1063/1.1903106/14935918/114325_1_online.pdf. URL: https://doi.org/10.1063/1.1903106.

[126] F. Glas. "Critical dimensions for the plastic relaxation of strained axial heterostructures in free-standing nanowires". In: *Phys. Rev. B* 74 (12 2006), p. 121302. DOI: 10.1103/PhysRevB.74.121302. URL: https://link.aps.org/doi/10.1103/PhysRevB.74.121302.

[127] K. L. Kavanagh. "Misfit dislocations in nanowire heterostructures". In: *Semiconductor Science and Technology* 25.2 (2010), p. 024006. DOI: 10.1088/0268-1242/25/2/024006. URL: https://dx.doi.org/10.1088/0268-1242/25/2/024006.

[128] C. Multiphysics. "Introduction to COMSOL multiphysics®". In: *COMSOL Multiphysics, Burlington, MA, accessed Feb* 9 (1998), p. 2018.

[129] A. K. Head. "Edge Dislocations in Inhomogeneous Media". In: *Proceedings of the Physical Society. Section B* 66.9 (1953), p. 793. DOI: 10.1088/0370-1301/66/9/309. URL: https://dx.doi.org/10.1088/0370-1301/66/9/309.

[130] P. Anderson, J. Hirth, and J. Lothe. *Theory of Dislocations*. Cambridge University Press, 2017. ISBN: 9780521864367. URL: https://books.google.dk/books?id=LK7DDQAAQBAJ.

[131] A. Mazuelas, L. González, F. Ponce, L. Tapfer, and F. Briones. "Critical thickness determination of InAs, InP and GaP on GaAs by X-ray interference effect and transmission electron microscopy". In: *Journal of Crystal Growth* 131.3 (1993), pp. 465–469. ISSN: 0022-0248. DOI: https://doi.org/10.1016/0022-0248(93)90197-5. URL: https://www.sciencedirect.com/science/article/pii/0022024893901975.

[132] H. Ye, P. Lu, Z. Yu, Y. Song, D. Wang, and S. Wang. "Critical Thickness and Radius for Axial Heterostructure Nanowires Using Finite-Element Method". In: *Nano Letters* 9.5 (2009), pp. 1921–1925. DOI: 10.1021/nl900055x. eprint: https://doi.org/10.1021/nl900055x. URL: https://doi.org/10.1021/nl900055x.

[133] Q. Liu, C. Zhao, S. Su, J. Li, Y. Xing, and B. Cheng. “Strain Field Mapping of Dislocations in a Ge/Si Heterostructure”. In: *PLOS ONE* 8.4 (2013), pp. 1–6. DOI: 10.1371/journal.pone.0062672. URL: https://doi.org/10.1371/journal.pone.0062672.

[134] J. J. Peters, R. Beanland, M. Alexe, J. W. Cockburn, D. G. Revin, S. Y. Zhang, and A. M. Sanchez. “Artefacts in geometric phase analysis of compound materials”. In: *Ultramicroscopy* 157 (2015), pp. 91–97. ISSN: 0304-3991. DOI: https://doi.org/10.1016/j.ultramic.2015.05.020. URL: https://www.sciencedirect.com/science/article/pii/S030439911500131X.

[135] F. K. LeGoues, M. C. Reuter, J. Tersoff, M. Hammar, and R. M. Tromp. “Cyclic Growth of Strain-Relaxed Islands”. In: *Phys. Rev. Lett.* 73 (2 1994), pp. 300–303. DOI: 10.1103/PhysRevLett.73.300. URL: https://link.aps.org/doi/10.1103/PhysRevLett.73.300.

[136] T. Merdzhanova, S. Kiravittaya, A. Rastelli, M. Stoffel, U. Denker, and O. G. Schmidt. “Dendrochronology of Strain-Relaxed Islands”. In: *Phys. Rev. Lett.* 96 (22 2006), p. 226103. DOI: 10.1103/PhysRevLett.96.226103. URL: https://link.aps.org/doi/10.1103/PhysRevLett.96.226103.

[137] E. Gilardi, A. Fluri, T. Lippert, and D. Pergolesi. “Real-time monitoring of stress evolution during thin film growth by in situ substrate curvature measurement”. In: *Journal of Applied Physics* 125.8 (2018), p. 082513. ISSN: 0021-8979. DOI: 10.1063/1.5054092. eprint: https://pubs.aip.org/aip/jap/article-pdf/doi/10.1063/1.5054092/15221850/082513_1_online.pdf. URL: https://doi.org/10.1063/1.5054092.

[138] O. Vazquez-Mena, L. Gross, S. Xie, L. Villanueva, and J. Brugger. “Resistless nanofabrication by stencil lithography: A review”. In: *Microelectronic Engineering* 132 (2015). Micro and Nanofabrication Breakthroughs for Electronics, MEMS and Life Sciences, pp. 236–254. ISSN: 0167-9317. DOI: https://doi.org/10.1016/j.mee.2014.08.003. URL: https://www.sciencedirect.com/science/article/pii/S0167931714003359.

[139] Y.-C. Sun, G. Boero, and J. Brugger. “Nanobridge Stencil Enabling High Resolution Arbitrarily Shaped Metallic Thin Films on Various Substrates”. In: *Advanced Materials Technologies* 8.2 (2023), p. 2201119. DOI: https://doi.org/10.1002/admt.202201119. eprint: https://onlinelibrary.wiley.com/doi/pdf/10.1002/admt.202201119. URL: https://onlinelibrary.wiley.com/doi/abs/10.1002/admt.202201119.

[140] N. Muthusubramanian, P. Duivestein, C. Zachariadis, M. Finkel, S. L. M. van der Meer, H. M. Veen, M. W. Beekman, T. Stavenga, A. Bruno, and L. DiCarlo. *Wafer-scale uniformity of Dolan-bridge and*

bridgeless Manhattan-style Josephson junctions for superconducting quantum processors. 2023. arXiv: 2304.09111 [quant-ph].

[141] O. Vazquez-Mena, L. G. Villanueva, V. Savu, K. Sidler, P. Langlet, and J. Brugger. "Analysis of the blurring in stencil lithography". In: *Nanotechnology* 20.41 (2009), p. 415303. DOI: 10.1088/0957-4484/20/41/415303. URL: https://dx.doi.org/10.1088/0957-4484/20/41/415303.

[142] S. Fritz, L. Radtke, R. Schneider, M. Weides, and D. Gerthsen. "Optimization of Al/AlOx/Al-layer systems for Josephson junctions from a microstructure point of view". In: *Journal of Applied Physics* 125.16 (2019), p. 165301. ISSN: 0021-8979. DOI: 10.1063/1.5089871. eprint: https://pubs.aip.org/aip/jap/article-pdf/doi/10.1063/1.5089871/15227875/165301_1_online.pdf. URL: https://doi.org/10.1063/1.5089871.

[143] A. Bilmes, A. Megrant, P. Klimov, G. Weiss, J. M. Martinis, A. V. Ustinov, and J. Lisenfeld. "Resolving the positions of defects in superconducting quantum bits". In: *Scientific Reports* 10.1 (2020). DOI: 10.1038/s41598-020-59749-y. URL: https://doi.org/10.1038/s41598-020-59749-y.

[144] M. Eichinger. "Novel methods and materials for superconducting qubits and circuits". English. PhD thesis. 2023. URL: https://nbi.ku.dk/english/theses/phd-theses/michaela-eichinger/.

[145] V. Nguyen, E. Shkondin, F. Jensen, J. Hübner, P. Leussink, and H. Jansen. "Ultrahigh aspect ratio etching of silicon in SF6-O2 plasma: The clear-oxidize-remove-etch (CORE) sequence and chromium mask". English. In: *Journal of Vacuum Science & Technology. A. Vacuum, Surfaces, and Films* 38.5 (2020). ISSN: 0734-2101. DOI: 10.1116/6.0000357.

[146] V. Nguyen, C. Silvestre, P. Shi, R. Cork, F. Jensen, J. Hubner, K. Ma, P. Leussink, M. de Boer, and H. Jansen. "The CORE Sequence: A Nanoscale Fluorocarbon-Free Silicon Plasma Etch Process Based on SF6/O2 Cycles with Excellent 3D Profile Control at Room Temperature". English. In: *ECS Journal of Solid State Science and Technology* 9.2 (2020). ISSN: 2162-8769. DOI: 10.1149/2162-8777/ab61ed.

[147] S. Gillies et al. *Shapely: manipulation and analysis of geometric objects*. toblerity.org, 2007. URL: https://github.com/Toblerity/Shapely.

[148] J. Biznarova, A. Osman, E. Rehnman, L. Chayanun, C. Krizan, P. Malmberg, M. Rommel, C. Warren, P. Delsing, A. Yurgens, J. Bylander, and A. F. Roudsari. *Mitigation of interfacial dielectric loss in aluminum-on-silicon superconducting qubits*. 2023. arXiv: 2310.06797 [quant-ph].

[149] T. M. Brennan, J. Y. Tsao, and B. E. Hammons. “Reactive sticking of As4 during molecular beam homoepitaxy of GaAs, AlAs, and InAs”. In: *Journal of Vacuum Science & Technology A* 10.1 (1992), pp. 33–45. ISSN: 0734-2101. DOI: 10.1116/1.578147. eprint: https://pubs.aip.org/avs/jva/article-pdf/10/1/33/11513689/33_1_online.pdf. URL: https://doi.org/10.1116/1.578147.

Colophon

This document was typeset using LaTeX, a high-quality typesetting system. The template uses various packages to enhance the typographic quality and ease of use, providing a consistent and visually appealing result.

This thesis was typeset using an altered version of the *Fantastic PhD Thesis Template*. It is licensed under the Creative Commons Attribution-Non Commercial 4.0 International License (CC-BY-NC 4.0). The source code for this template, along with the full documentation, can be found on GitHub at https://github.com/maiani/fantastic_template.